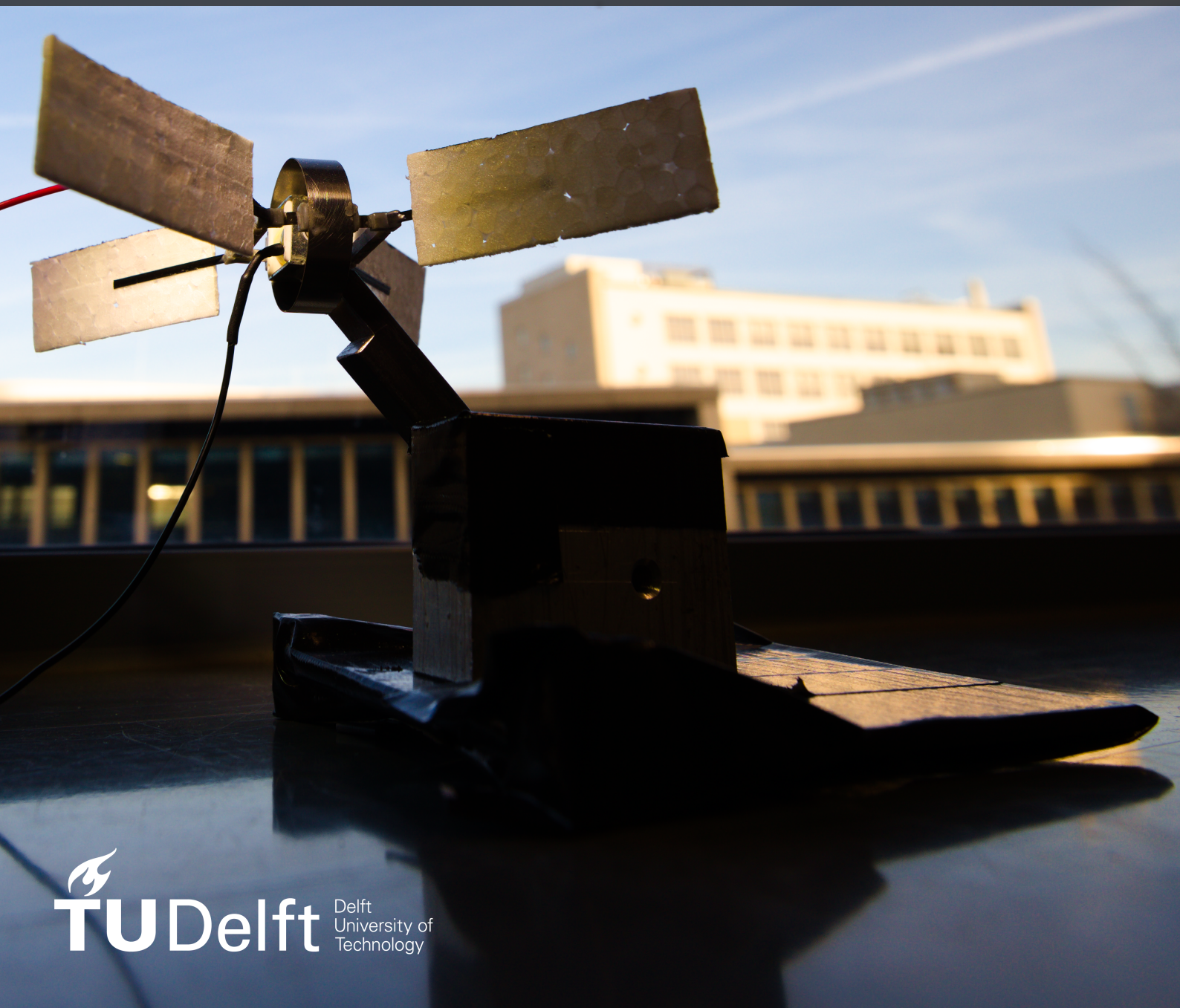
Experimental Investigation of Resonant Dynamics in the Atalanta

Response Modification through Local Stiffness Variations in a Compliant Flapping-Wing Micro Air Vehicle Prototype

M. H. A. Doornink



TU Delft Delft University of Technology

Experimental Investigation of Resonant Dynamics in the Atalanta

Response Modification through Local Stiffness Variations in a Compliant Flapping-Wing Micro Air Vehicle Prototype

by

Mynne Henke Arie Doornink

to obtain the degree of

Master of Science
in Mechanical Engineering

at Delft University of Technology,
Faculty of Mechanical Engineering,
Departments of Precision and Microsystems Engineering,
& BioMechanical Engineering

To be defended publicly on Friday March 6, 2026 at 10:30 CET.

Student number:	4678494		
Supervisors:	S. Basile, MSc.	Daily Supervisor	
	Dr. *ir.* J. F. L. Goosen	Responsible Supervisor	
Thesis committee:	Dr. *ir.* J. F. L. Goosen	Committee Chair	TU Delft ME-PME
	S. Basile, MSc.	Committee Member	TU Delft ME-PME
	Dr. J. K. Moore	External Committee Member	TU Delft ME-BMD
	Dr. R. H. Guis	External Committee Member	TU Delft ME-PME

An electronic version of this thesis is available at `http://repository.tudelft.nl/`.

TU Delft

Preface

When viewing the world using the curiosity my parents taught me as a child, I can still see how the world around me is marvellously interesting, even when it seems mundane. My studies thought me to take this curiosity and explore the intricacies of anything that sparks my interest. It also gave me the skills to try and use my curiosity for good and to help others when doing so.

This research was driven by such an exploration. I tried to dive deeper into my lifelong interest of insects. The first presentation I did in elementary school was on beetles. Their shields, colours and jaws fascinated me as a child, and they still do. My high school senior project was on the use of bugs as livestock, as a more ethical approach to feed the world with complex proteins. At university, I learned to explore through physically building machines, and now, this thesis is focused on replicating the amazing flight mechanics of insects. I strive to never lose my curiosity, and I hope this thesis inspires others to stay curious as well.

M. H. A. Doornink
Rotterdam, February 2026

Abstract

This thesis explores the dynamic behaviour of a flapping-wing micro air vehicle (FWMAV) prototype, when actuated at resonance to increase flight efficiency. The prototype is based on a four wing vehicle design called the Atalanta FWMAV. The current research adopted a Straight Linkage Concept, which was hypothesized to be more sensitive to control inputs used for steering. The used control inputs are local structural property modifications, which alter the dynamic response of the prototype when operating at resonance. The Straight Linkage Concept entails a two degree of freedom compliant mechanism capable of transferring linear actuator motion into rotational wing flapping motion. The prototype was designed and physically realized to be a representation of the fully integrated Atalanta, without lift-off capable wings. In the prototype, stiffness was passively varied to induce response modifications, giving an indication on the performance of the Straight Linkage Concept.

Three experimental methods were developed to investigate the functioning of the FWMAV prototype. The first method was used to measure the individual stiffness of specific flexures in the compliant mechanism. The second method measured the amplitude response as a function of frequency in two distinct stiffness configurations. By taking photographs of the wings at different frequencies, the influence of the variations in stiffness on the amplitudes of the wings are characterized. The third method measured the phase relation between the wings in two distinct stiffness configurations. By taking stroboscopic videos of the wings at different frequencies, the influence of variations in stiffness on the phase delay of each wing were characterized.

Together, the methods provided insights into the dynamic behaviour of the prototype. It was found that locally changing the sweeping hinge stiffness affected the resonant dynamics of the four wing drone as a whole, as well as the response of individual wings. In fact, the frequency response functions indicated that the applied stiffness modification increased the amplitude of one wing, while it decreased the amplitude of the other wings. The dynamic response of both amplitude and phase were modified due to the local stiffness variations, indicating an asymmetric lift distribution can be realized over the four wings, which is necessary for steering. Furthermore, it was found two eigenmodes dominate the dynamics of the physical prototype. Under a symmetric stiffness distribution, an out-of-phase mode shape was observed, wherein two wings in the Straight Linkage Concept move in opposite directions. The applied stiffness increase caused the oscillations to include an in-phase mode shape, wherein two wings move in equal directions. The in-phase mode shape is thought to have less equivalent stiffness, which allows for increased flapping amplitudes in a stiffer configuration. The capability of the Straight Linkage Concept to shift from one mode to the other is thought to allow for more elaborate and highly sensitive dynamic response modifications under limited local stiffness increase, allowing for high controllability with low control effort.

Acknowledgements

This thesis was written with the help of many others. These people helped me tremendously by giving me their time and attention, or they allowed me to use their work. I want to express my gratitude towards the amazing support network I got to be a part of at TU Delft, and in my personal life.

First and foremost, I want to thank my supervisors, Serena Basile and Hans Goosen. For more than a year, Serena and Hans spent their time by helping me structure my thoughts, focus my work and to show me how to be a researcher. When I was stuck in my research direction or the matter was seemingly too complex, both Hans and Serena always had their door open to help me get back on track. Thank you Serena, for the interesting weekly meetings, the thorough feedback, and the insights on a wide array of topics such as physics, design, writing and teaching. Thank you Hans, for providing the necessary changes in research focus, for allowing me to graduate at PME on this interesting topic, recommending me to the CERN staff, and for showing me how this thesis taught me to be an engineer.

I also want to thank my friends and family. My parents, Willemijn en Ger, who taught me to be curious and supported me throughout my studies. My bothers and sisters, Jula, Rense, Celine and Daniël, who showed me to pursue my own interest. My friends and roommates, Gillis and Sam, who where so kind to help me by brainstorming, practising presentations and cooking for me. My friends, Bastian, Dido, Isa, Jakob, Jelle, Jip, Noortje, Vita, Zola and Zora, who kept me going in the past year. I feel grateful to have so many friends so close around me. Finally, I want to thank Jip, who was always there for me, even when she was more fed up with this thesis then I was. Thank you so much Jip.

I want to thank the people that provided hardware, software, information or support throughout my thesis. First of all, the employees and colleagues at the Faculty Workshop of the Mechanical Engineering Faculty at TU Delft contributed to this thesis by engaging with me, suggesting ideas, helping with manufacturing or using specialized equipment. Especially Jacques Brenkman from the Measurement Shop helped me with understanding measurement equipment, sourcing sensors and actuators, and understanding measurement limitations. Thank you guys. Secondly, hardware setups and electronics designed and built by others were used to measure the prototype developed in this thesis. The transistor circuit was designed and soldered by Bradley But from the Precision and Microsystems Engineering (PME) department. The force-displacement sensor stage was also built by the staff of the PME department. Furthermore, the PME staff were always available for questions and help, which greatly contributed to this thesis. Thanks for that. Finally, the developers of open source software contributed by building the apps that I needed to write this thesis and create code and diagrams. The open source programs I used are draw.io, RawTherapee, Python 3, digiCamControl and Overleaf, and are greatly recommended. Furthermore, a special contribution was made by open source developer Daan Zwaneveld by distributing the LaTeX thesis template used to write this thesis.

Thank you all. I could not have done it alone.

Statement on the use of Artificial Intelligence

This statement declares that this thesis is the authors own work, and that all sources of information have been properly cited. The author acknowledges the use of artificial intelligence (AI) as a research tool. The AI, in the form of a large language model (LLM) created by OpenAI, was used in several ways. The LLM was used to explain concepts and guide initial literature research directions, to test hypotheses or chains of thought, to refine focus in writing, or to transform methods into functional MATLAB, Python or LaTeX code. The LLM was not used write any part of this thesis. Any output of the LLM, in the form of code or information, was critically evaluated on functioning and truth. The author has full intellectual responsibility over the used methods and the written work. When the LLM was used to generate a method, it was in the form of a computer program implementation, later refined by the author. These use cases are stated in the methods section of this thesis.

Nomenclature

Glossary

Term	Definition
Linkage	A mechanism that translates linear motion of the central actuator to rotational motion of the wings. Each linkage has two wings attached. There are two linkages in the prototype.
Original	Stiffness distribution wherein all flexures in the prototype are designed to have the same flexural rigidity.
Stiff V1	Stiffness distribution wherein one flexure is designed to have a higher flexural rigidity.
Stiff V2	Stiffness distribution wherein two flexures are designed to have a higher flexural rigidity. The flexural rigidity of these two flexures is equal. One of these two flexures is the altered flexure of the Stiff V1 configuration. The second flexure is not in the same linkage as the first flexure. The location is defined in figure 1.4.

Abbreviations

Abbreviation	Definition
CAD	Computer Aided Design
CFRP	Carbon-Fibre Reinforced Polymer
(M)DOF	(Multi) Degree of Freedom
DSLR	Digital Single-Lens Reflex
EOM	Equation of Motion
FEM	Finite Element Method
FRF	Frequency Response Function
FWMAV	Flapping-Wing Micro Air Vehicle
LLM	Large Language Model
PCHIP	Piecewise Cubic Hermite Interpolating Polynomial
PRBM	Psuedo Rigid Body Method
PWM	Pulse Width Modulation
(M)SLA	(Masked) Stereo-Lithography Apparatus

Symbols

Symbol	Definition	Unit
A	Theoretical sweeping angle amplitude assuming harmonic oscillation	*rad*
$\hat{A}$	Measured sweeping angle amplitude using shutter speed T_w	*rad*
EI	Flexural rigidity	Nmm^2
F_{act}	Actuator force	*N*
f_{act}, f	Actuator frequency	*Hz*

Symbol	Definition	Unit
k_1–k_8	Stiffness values of the flexures in the Straight Linkage Concept	*Nmm/rad*
k_r	Central ring stiffness	*N/mm*
L_1–L_8	Lengths of the respective flexures (global context)	*mm*
L_1, L_2	Characteristic hinge distances used in transmission ratio analysis	*mm*
R	Wing span (wing design context)	*mm*
R	Central ring diameter (flexure mechanism context)	*mm*
R^2	Coefficient of determination	–
T	Oscillation period ($T = 1/f_{act}$)	*s*
T_w	Camera shutter speed	*s*
t	Thickness of a flexure or glue layer (subscript denotes type)	*mm*
u	Central actuator displacement	*mm*
w_1–w_4	Wing numbering index (with respect to lead wire orientation in figure 1.4)	–
ϕ	Peak-to-peak sweeping angle amplitude	$^\circ$
ω_{act}	Actuator angular rate	*rad/s*

Contents

Preface i

Summary ii

Acknowledgements iii

Statement on the use of Artificial Intelligence iv

Nomenclature v

1 Introduction 1
- 1.1 Flapping Wing Micro Air Vehicles . . . 1
  - 1.1.1 Resonance Mechanics & Biological Inspiration . . . 1
  - 1.1.2 TU Delft Atalanta . . . 3
- 1.2 Research Objective . . . 3
  - 1.2.1 Challenges in Utilizing Resonance for Flight Efficiency . . . 3
  - 1.2.2 Tuning the Structural Properties for Steering . . . 3
- 1.3 Research Questions . . . 6
- 1.4 Thesis Structure . . . 7

2 Theoretical Framework 8
- 2.1 Linkage Mechanism & Kinematics . . . 8
- 2.2 Dynamics . . . 10
  - 2.2.1 Aerodynamics & Manoeuvre Forces . . . 10
  - 2.2.2 Resonance of Damped Linear Systems . . . 12
- 2.3 Experimental Framework and Requirements . . . 14
  - 2.3.1 Experiment . . . 14
  - 2.3.2 Requirements . . . 14

3 Experimental Methodology 16
- 3.1 Prototype Design & Manufacture . . . 16
  - 3.1.1 Research Prototype Design . . . 16
  - 3.1.2 Design Choices . . . 19
  - 3.1.3 Manufacturing Procedures & Inducing Stiffness Variations . . . 22
- 3.2 Measuring Stiffness . . . 24
  - 3.2.1 Estimating Flexural Rigidity . . . 24
  - 3.2.2 Measuring Stiffness Variations . . . 26
- 3.3 Measuring Dynamic Responses . . . 27
  - 3.3.1 Modal Analysis . . . 27
  - 3.3.2 Measuring Sweeping Amplitude . . . 28
  - 3.3.3 Measuring Phase . . . 30

4 Results & Interpretations 32
- 4.1 Manufactured Prototype . . . 32
  - 4.1.1 Dimensional Measurements . . . 33
- 4.2 Modal Analysis . . . 33
  - 4.2.1 Interpretation and Validity of the Numerical Modal Analysis . . . 35
- 4.3 Stiffness Measurements . . . 36
  - 4.3.1 Evaluating Flexural Rigidity . . . 37
  - 4.3.2 Interpretation and Validity of Stiffness Measurements . . . 38
- 4.4 Photography Measurements . . . 41
  - 4.4.1 Sweeping Angle Frequency Response Functions . . . 41
  - 4.4.2 Interpretation and Validity of Sweeping Angle FRF . . . 43
- 4.5 Video Measurements . . . 47
  - 4.5.1 Interpretation and Validity Phase FRF . . . 49

5 Implications for the Atalanta FWMAV **53**
5.1 Sensitivity Estimation 53
5.2 Recommendations on Physical Modelling 54
5.3 Recommendations on Measuring the Dynamics of the Atalanta 56

6 Conclusions **57**
6.1 The Behaviour of the Straight Linkage Concept 57
6.2 Final thoughts on Controlling the Atalanta FWMAV 59

Bibliography **60**

A Stiffness Measurements **63**

1 Introduction

1.1. Flapping Wing Micro Air Vehicles

The centuries-old desire of mankind to mimic the flight of birds and insects has resulted in the creation of the machines seen taking to the skies today. Yet, only recently, autonomous drones, or unmanned aerial vehicles (UAVs), allow engineers and scientists to think new machines and systems that utilize the sky in different ways. Applications range from autonomous surveillance, assisted agriculture and art, to military, emergency response, or medical logistics [1]–[6].

The common functions in these examples are the unobstructed movements and agile flight envelopes. Most of the drones currently used for this purpose are fixed or rotary wing vehicles [7], [8]. For certain applications these drones do not suffice. Especially in tightly spaced or indoor applications, the fixed and rotary wing designs fail due to a lack of manoeuvrability or loss of lift at lower Reynolds number flight conditions [9].

In order to mitigate these apparent problems, researchers drew inspiration from animal flight, by creating *flapping-wing micro air vehicles* (FWMAVs). Flapping wings utilize different aerodynamics than fixed or rotary wings. For example, their efficiency is influenced positively by the aerodynamic effects near solid structures [10]. The research interest into FWMAVs is well established, with research at not only Harvard, TU Delft and MIT [11]–[13]. A 2022 literature survey on actuation mechanisms used in FWMAVs, shows an upward trend in research on these devices between 2001 and 2021 [14].

The basis of the inspiration from animal flight is wide. For example, insects are capable of broad flight envelopes including hovering, backward flight or landing upside down on a ceiling [15]. Furthermore, when measuring insect flight, the energy demand per gram of bodyweight is found to be proportional to the mass and the wing length of the animal. Lighter insects require less power per gram of bodyweight, given that they increase their wing length [16]. Following these biological scaling laws gives a basis for miniature FWMAV designs. On top of that, flapping flight produces less noise and does not have fast moving rotors, positively influencing human robot interactions.

However, when hovering, the absence of a forward flight induced fluid flow over the wings, demands extra energy for a FWMAV to stay aloft. Mitigating and overcoming this high energy demand is crucial for the creation of fully autonomous and untethered FWMAV.

1.1.1. Resonance Mechanics & Biological Inspiration

Because of the above mentioned extra energy demand for hovering, it is necessary to minimize non-conservative processes in the FWMAVs. Amongst these, multiple processes are inherent to the functions of the system, such as aerodynamic drag acting on the wing or actuator and electronic losses. One particular non-conservative process found in FWMAVs is the energy wasted on the oscillations in the wing motion. Each flapping stroke, the wings are accelerated and decelerated twice. Rotary wing aircraft do not suffer from this particular energy loss, because the angular momentum in the rotor blades is only damped by friction and drag [17]. To aid in the understanding of this problem, one might imagine the practical limitations of a helicopter which oscillates its rotors, instead of spinning them.

However, exciting an oscillating mechanism with an elastic element at resonance would, theoretically, mitigate the inertial energy losses [18]. Similar to pushing a swing, maintaining the motion by exciting a resonant frequency requires less energy. It requires a force to overcome non-conservative losses such as friction and drag, but energy is stored in the system through potential gravitational energy at the highest points in the swing's oscillations. In the drone, the wings would move using a similar mechanism. Instead of gravity, the system relies on potential elastic energy of springs. When the wings have to accelerate and decelerate during an oscillation, a stiff structure can convert potential elastic energy to kinetic energy and aid the flapping motion.

Researchers from multiple fields have shown interest in the excitation of structures at their resonant frequencies. The energy efficiency of resonance could be used by other vibrating systems, such as energy harvesters or accelerometers [19]–[23]. The common theme in these fields is the use of elastically deforming, oscillating members capable of storing and releasing energy in a compliant or spring-like fashion. The eigenfrequency and resonant behaviour is influenced by the mass, stiffness and damping in the system and the distribution thereof.

Not coincidentally, a similar mechanism is found in animals. The present day biological consensus on the functioning of insect flight motors in some insect species, such as butterflies, wasps and flies, is to use the flight muscles to elastically deform the exoskeletal thorax structure, instead of directly pulling on the wings [24], [25]. This mechanism is called an *indirect flight motor*. Additionally, rubber like protein structures called 'resilin' are found to be attached to wing hinges. Both these structures are coupled to the wings and excited in resonance to create an efficient flapping motion [26]. However, the biomechanics governing control and efficiency of animal flight is still an open research topic [27], [28]. A 2022 paper on resonance mechanics in indirect insect flight motors, suggest insects are capable of finding near-resonance, energetically optimal flight motor conditions for multiple frequencies, dependant on flight conditions [25].

Therefore, one of the mayor driving factors for the current research is the fact that small, 1 mm sized insects exist, such as fairyflies in the family of *Mymaridae*. The intricacy of flying creatures has not yet been reproduced by humans, despite the research effort pointed out before.

This raises many biomechanically related questions. For example, what makes it possible for these animals to fly, let alone perform animal behaviours such as eating, finding mates or generating offspring? What can be learned from the insect biology and biomechanics, in order to further develop the capabilities of small scale manufacturing? What is so efficient about the biomechanical lift generation of flapping, causing animals of many different shapes and sizes to evolve?

Evidently, the research and development of FWMAVs not only applies to the use case of the drones themselves. Broader fields of research, such as miniaturization, control theory, aerodynamics, structural mechanics, energy efficient design or biology can benefit and interact with research into FWMAVs. The research interest leading to this thesis originated in a project at Delft University of Technology [29]–[31]. The device resulting from this research is called the *Atalanta FWMAV*.

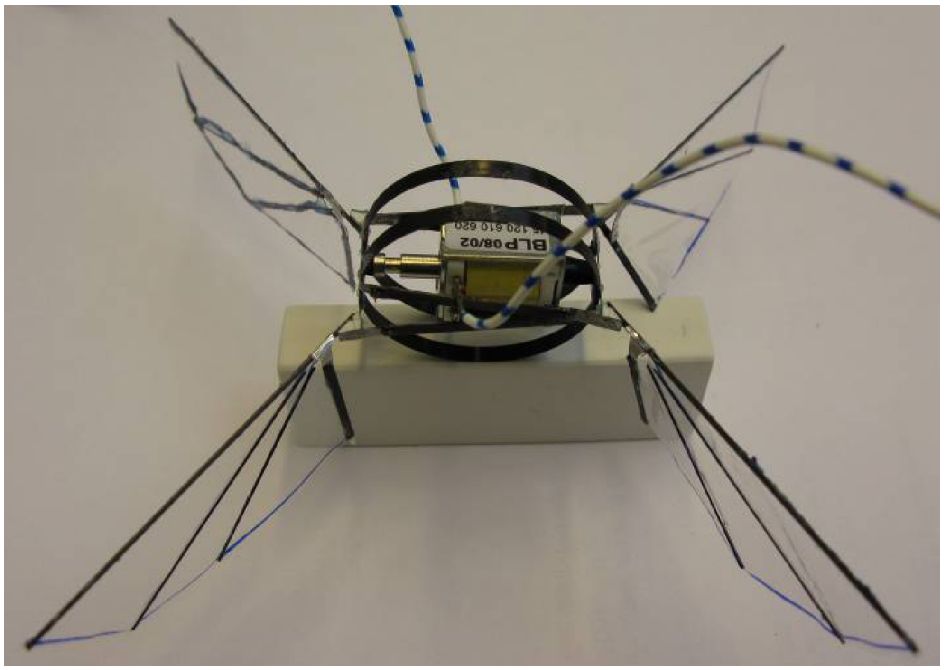


Figure 1.1: Picture of a prototype Atalanta FWMAV manufactured and studied by Bolsman [29].

1.1.2. TU Delft Atalanta

The Atalanta is a prototype FWMAV capable of generating lift by using a resonating compliant mechanism actuated by a chemical bellows actuator. The drone serves as a research framework to develop and experiment on the mechanics and fabrication of lightweight resonating devices, the development of aerodynamic models for flapping flight, and the development of efficient micro actuation systems.

The current version of the Atalanta is a four wing drone with an elastic ring element at its center, surrounding a main actuator, as shown in figure 1.1. As stated, the drone is designed to operate at resonance. This resonant state is maintained through the compliance of the central ring, which acts on a linkage mechanism attached to the wings. The linkage mechanism allows all four wings to move in a synchronous matter, excited only by the central actuator. Each wing has its own passive pitching hinge, connecting the wing to the linkage system. As the requirements for miniaturizing flapping flight are stringent, research is unfinished. The Atalanta is not yet capable of actively stabilized autonomous flight, let alone carrying payloads or performing advanced flight manoeuvres. The assembled drone was measured to produce lift, but no stable lift off has been achieved [29].

1.2. Research Objective

1.2.1. Challenges in Utilizing Resonance for Flight Efficiency

When critically exploring the concept of resonating mechanisms in FWMAVs, multiple challenges arise. First of all, the efficiency of the mechanism is highly sensitive to the excitation frequency. Exciting the system at frequencies higher or lower than the natural frequency of the structure might prevent lift-off in FWMAV designs which are dependant on the amplifications in the resonant state [32].

Secondly, the resonant state of the system is dependant not only on the structural mechanics, but also on geometric non-linearities and aerodynamic damping in the system [29]. For example, non-linearities in the flapping motion using passive pitching wings can cause the resonant frequency of the system to be dependant on the amplitude of system itself [32]. Furthermore, increased aerodynamic damping due to varying wind loads might change the resonance state of the system, although it is found in literature on insects this effect is small [29]. Here, Q-factors in insects are reported to be up to 19, showing the inertial effects should dominate over the aerodynamic damping [16].

Thirdly, in order to control a mechanism, it is necessary to change the state of its degrees of freedom (DOFs). This can be achieved by actuating a system externally, similar to pushing the swing, or internally, like changing the orientation of the sails and rudder on a sailboat. In FWMAVs, the control effort is internal and entails changing the geometry, attitude or velocity of the wings during oscillations. These changes influence the aerodynamic lift production of individual wings, thus applying control forces to orient and accelerate the drone as a whole [9]. As the actuation is applied to the structure, the structure changes, and thus its response to vibrations changes accordingly [18].

Finally, the geometrical accuracy and material qualities acquired during the manufacturing of a structure govern the shape, stiffness and damping and thus its resonance behaviour. For example, a deviation from an intended cross-section or Young's modulus might change the resonant state of the fabricated mechanism. Even during operation, the resonance of a perfectly manufactured structure might change due to the dependence of stiffness governing material properties on temperature or fatigue [33].

The common element in the above mentioned problems is an unwanted change in the resonance. A solution would be to actively modify the resonance to a desired state. If the structure could monitor and modify the mass, stiffness, damping or distribution thereof, it would be able to control the oscillation and benefit from the efficient resonant state in different conditions. Additionally, the control of the resonance behaviour might be sufficient to control the whole mechanism. This would eliminate the need for additional control actuators and aid integration of parts. Finally, an active structure could reverse any structural property deviations generated by fabrication errors.

1.2.2. Tuning the Structural Properties for Steering

This thesis aims to shed light on the use of resonating mechanism and the functioning of those mechanisms when subjected to local structural modifications, in physical prototypes. The focus of the thesis lies on using structural modifications for steering. The main idea is adopted from the PhD theses by Bolsman, Peters and Wang under guidance of Goosen [29], [31], [34], [35]. An outline of the idea is shown in figure 1.2. The compliant mechanism inside the drone is actuated using a single actuator. When hovering, this actuator drives the wings of the drone simultaneously, generating a sweeping angle ϕ, equal for all four wings. A larger sweeping angle at a certain frequency requires a higher wing speed and creates more lift [34]. If lift

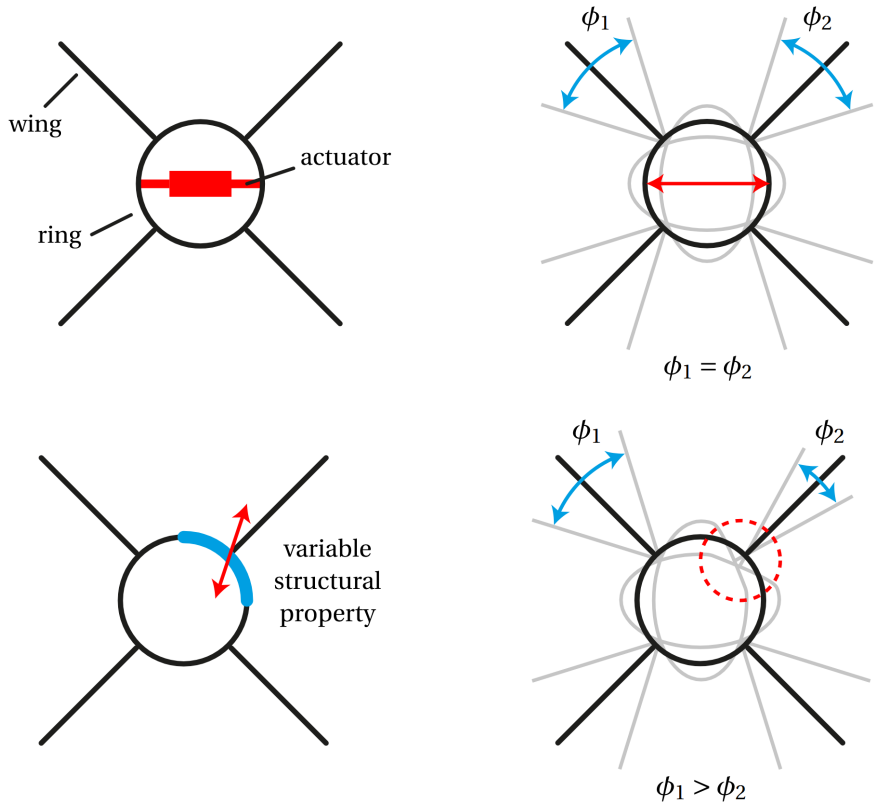


Figure 1.2: Schematic representation of control, using a resonance response alteration induced by a variable structural property. The top right figure shows, for example, a hovering response, where the bottom right response would be for steering [31].

production is equal over all wings, the system will lift straight up and hover. However, this is an unstable system, and active control of the attitude of the drone is required.

The amount of sweeping displacement at each of the wings is governed by the compliant linkage mechanism that connects the wings to the actuator. This linkage is made up of flexures and rigid bodies. When driving the system at a resonant frequency, the amplitude of the wings increase without having to supply more power to the main actuator, increasing its efficiency. This resonance response is governed by the structural properties of stiffness, mass and damping within mechanism and the distribution thereof [18].

Now, one might apply specific changes to these structural properties to influence the response of the wings. For example, stiffness might be increased. In this new stiffness configuration, a new response might have a lower sweeping amplitude in one wing than for the other wings. As the generated lift scales with amplitude, this would cause an asymmetric lift around the center of the drone, creating a torque and tipping the system. This tipping can now be used for steering purposes. If each of the three rotational degrees of freedom could be controlled by modulating the structural properties in specific configurations, then the structural property modifications can act as a control input. With enough bandwidth and lift modification, the structural changes might be able stabilize and control the flight of the Atalanta.

If this process were able to control the Atalanta, the control actuators could be integrated within the passive elements that make up the compliant structure, reducing the weight of the drone. However, this requires the compliant mechanism to be manufactured from materials capable of changing their structural properties as a response to control signals. Furthermore, it is necessary to understand the effect of the structural modifications on the resonant dynamics of the drone. Research on this has been conducted, but is not finished.

The subjects in this thesis aim to shed light on designing resonating structures for efficient flight, within the context of the Atalanta. This thesis focuses on the changes in oscillating behaviour due to changes in stiffness. Specifically, this thesis aims to identify the dynamic response of a design referred to as the *Straight Linkage Concept*. By experimentally analysing the dynamic effects of changes in local sweeping hinge stiffness, the implications for steering capabilities are researched.

The Straight Linkage Concept is one of two prominent linkage mechanism concepts in the research of Bolsman [29]. The second concept is referred to as the *Cross Linkage Concept*. Both concepts transfer linear actuator motion into rotational wing sweeping motion. However, the Cross Linkage Concept can do this more efficiently, given the links in the mechanism are the same length. The functioning of the two concepts is elaborated in chapter 2.

The most important difference between the two concepts are the DOFs between the wing sweeping angle and the actuator. The Cross Linkage Concept has a single DOF, while the Straight Linkage Concept has two. This implies that the sweeping motion of the Cross Linkage Concept is governed directly by the force of the actuator and the stiffness in the system. At resonance, the Cross Linkage Concept can oscillate at higher amplitudes. However, because of the single degree of freedom, a local structural property modification, as described in figure 1.2, is hypothesized not to influence the dynamics of specific wings. There is a different structural configuration, but the displacement will adjust equally for all wings.

For the Cross Linkage Concept, steering through structural property modifications are proposed to modulate a different mechanism. Namely, the passive pitching of the wing, influencing the angle of attack [31]. Changing the structural properties of the wing affects the amount of pitching, modifying the amount of lift generated. At rest, the pitching angle is 0° and the normal vector of the frontal wing area is pointed parallel to a tangential velocity due to sweeping. The angle of attack is maximum here. When oscillating, drag forces tilt the wing up, decreasing the angle of attack and allowing for lift generation [34]. Modulation of the amount of pitching can independently be implemented for each wing, allowing for steering. For example, stiffening the pitching hinge would cause less deflection under the same drag force, influencing the amount of lift. Another modification example, based in biology, is the hypothesized inertia modulation that dragonflies utilize. By pumping blood in different directions through their wings it is postulated dragonflies can influence their flight dynamics [36].

For the Straight Linkage Concept, the functioning is different. The extra DOF allows for more intricate dynamic responses to actuator displacement. For each position of the actuator, this linkage is free to displace further. Therefore, changing local structural properties of the linkage is hypothesized to influence each wing differently, allowing for steering. On top of this, passive pitching hinge modifications are still applicable to this concept, allowing to infer an increased overall controllability of the system [29].

Furthermore, the dynamics of the Straight Linkage Concept have been studied using numerical simulation, which found the eigenvalues of the structure to be closely spaced [29]. This is found to increase sensitivity of the wing oscillation response to structural property modifications [31]. Further investigation of this sensitivity is in order, especially in a physical prototype. A theoretical description of the sensitivity of damped resonant responses can be found in Peters' dissertation [31].

There are several methods found in literature capable of modifying structural properties. Methods include, but are not limited to, the following sets of materials referred to as *smart materials*:

- Smart fluids or fluid induced property changes [37]–[39].
- Sliding stacked layers [31], [34].
- Electrostatic softening and zipper actuators [19], [31], [40].
- Piezoelectric polymers [31], [41].

The governing control signal for most of these methods is either a voltage or a pressure. As with all control systems, their use requires weight budgets to be spent on control elements. The amount of weight spent on control depends on the used control strategy. The strategy dictates the control signal magnitude and the sensitivity of the plant to the controller. For example, the stacked layer approach adopted in previous research within the Atalanta project showed functional lift modifications using control signals ranging between 50 and 600 V. The efforts of Peters and Wang were focused on modifying the pitching angle amplitude of a wing using stiffness modifications. A 31% lift force reduction was found at 250 V when comparing experimental with analytical results [31], [34].

This voltage range is not necessarily a problem, and dependents on the plant dynamics of the system. However, more research on intricate micro-electronics to generate these voltages using light-weight structures is needed. Lowering the voltage for structural property modifications might enable a lift-off capable system, as it will weigh less and not be limited by these electronics. The required magnitude of the control signal can be lowered in two ways, by either increasing the efficiency of the smart material or increasing the sensitivity of a mechanism to property changes of the smart material. This thesis is focused on the latter, as the Straight Linkage Concept is deemed more sensitive to structural property modifications.

Furthermore, the controllability of the Straight Linkage Concept is arguably higher due aerodynamic effects. Two recent MSc thesis within the Atalanta project focused on the aerodynamics and mechanics of an optimal wing design by Wang [34]. Here, it was found that pitching hinge stiffness modulation can generate lift regimes where stall occurs, whereas sweeping angle modulation does not indicate this shortcoming [42], [43]. Furthermore, it was found that, by combining both pitching hinge stiffness and sweeping angle amplitude modulation, lift alterations in different flight conditions can be obtained [42]. This capability is only found in the Straight Linkage Concept.

The reasons to adopt the Straight Linkage Concept seem decisive. However, the functioning of a FW-MAV prototype which employs the Straight Linkage Concept has not been researched. It is unknown what the dynamic behaviour of this physical prototype entails, how it responds to property changes, how to manufacture the concept, nor how to control the extra degree of freedom it provides. Furthermore, generating a steering motion in any physical Atalanta prototype has not yet been achieved.

1.3. Research Questions

As stated in the previous section, thesis is focused on the functioning of the Straight Linkage Concept designed by Bolsman [29]. The research concerns the functioning of this concept in terms of structural property modifications induced steering through dynamic response alterations. To guide the exploration of the research, the following research questions are asked.

The main research question is:

> *What is the effect of using the Straight Linkage Concept on the steering and control capabilities of the Atalanta, when using structural property modifications as a control input?*

The research direction is supported by the following sub-questions:

1 *How sensitive are the resonant dynamics of the Straight Linkage Concept to local structural property modifications?*

2 *How does the extra degree of freedom of the Straight Linkage Concept affect the dynamics and resonance behaviour of the system?*

3 *In what way does the Straight Linkage Concept differ in steering capabilities compared to the Cross Linkage Concept?*

1.4. Thesis Structure

The thesis is structured in six chapters, as shown in the schematic of figure 1.3. The first chapter is the current chapter. The second chapter highlights relevant theory, used to define the design space and experimental requirements. The third chapter outlines the used methods of measuring dynamic response alterations due to controlled stiffness changes. The fourth chapter combines the found results with a discussion on the implications and validity of these results. The fifth chapter discusses approaches to combine the found results and recommends future steps in the continuation of the Atalanta project. The sixth and final chapter answers the research questions.

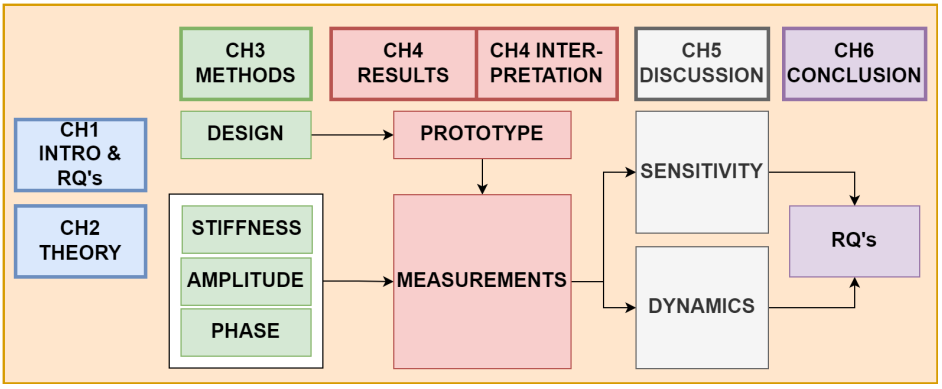


Figure 1.3: Structure of the thesis. The discussion is split in two parts. The result and interpretations are integrated in chapter 4. A discussion on the combination of all results is found in chapter 5.

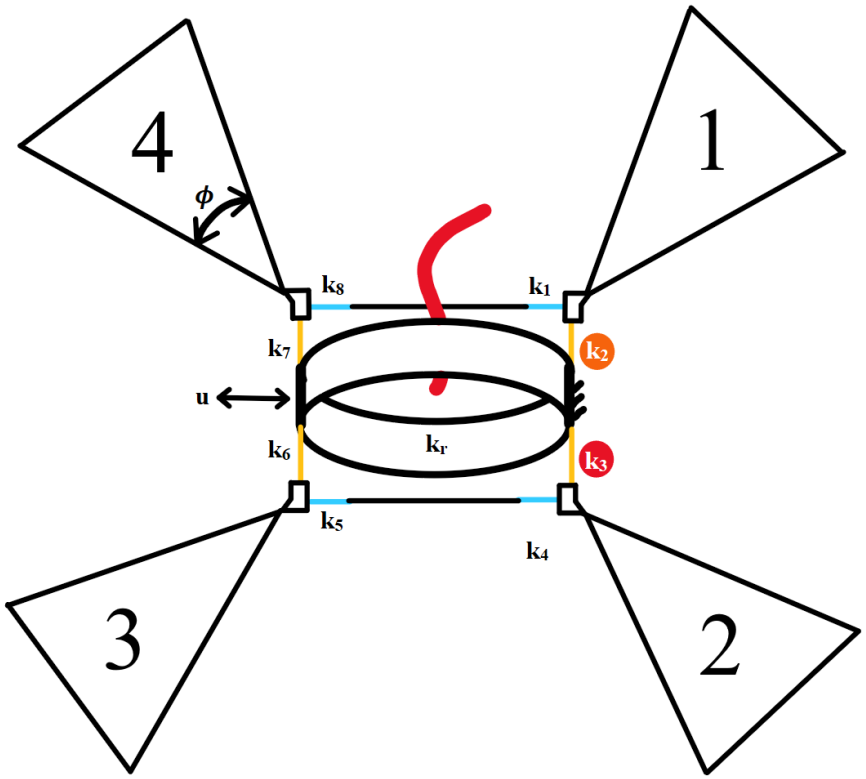


Figure 1.4: Nomenclature of wings and flexures with respect to the red actuator wire. On side of the ring is fixed, while the side indicated with the arrows oscillates due to the actuator movements. The system has two linkage systems. The linkage system connected to Wing 1 and Wing 4 is called the *Wing 1 - Wing 4* linkage. The linkage system connected to Wing 2 and Wing 3 is called the *Wing 2 - Wing 3* linkage. Flexures k_2 and k_3 have been modified in stiffness for configuration Stiff V1 and Stiff V2, respectively. The methods for changing the stiffness and their configurations are described in section 3.1.3.

2
Theoretical Framework

This chapter is aimed at defining requirements and criteria for the manufacturing and testing of a new prototype version of the Atalanta FWMAV, utilizing the Straight Linkage Concept. The chapter combines requirements and findings from literature with new findings, guiding the experimental research outlined in the methods of chapter 3. It explores relevant design variables and limits the scope of the research by determining the critical aspects of the concept.

2.1. Linkage Mechanism & Kinematics

The linkage mechanism translates linear movement from the actuator in to a rotational flapping movement of the wings. The mechanism creates a mechanical advantage through positioning of flexure hinges. Two schematics of the mechanisms preposed by Bolsman are shown in figure 2.1 [29]. Each concept has two linkages with two wings attached.

The analysis assumes the flexures in the linkages behave as pin joints, with one degree of rotational freedom. The rotation point lies at the center of each flexure length. Now, L_1 and L_2 in figure 2.1 is the distance between the idealized pin joint location of one flexure to the plane of the other flexure. Figure 2.2 shows a simplified schematic of the definition. P_1 and P_2 are the locations of the pin joints. As stated in section 1.2.2, for the same linkage lengths, the Cross Linkage Concept rotates the wings roughly twice the amount of the Straight Linkage Concept, dependant on L_1 and L_2 [29].

To be specific, when observing the Cross Linkage Concept in figure 2.1, a positive displacement u pulls P_1 down while pushing P_2 up. Where, in the Straight Linkage Concept, only P_1 is pulled down. When L_1 and L_2 are equal in both concepts, the Cross Linkage Concept creates more angular displacement in the attached wings than the Straight Linkage Concept. However, using optimal values for L_1 and L_2 can yield large flapping amplitudes for the Straight Linkage Concept as well, but is limited by manufacturability due to shorter flexures being required. The exact amount of wing sweeping displacement per unit actuator displacement input is to be determined.

Bolsman defined the relation between the actuator input and angular displacement output as equation 2.1 [29]. The relation is dependant on the chosen design variables L_1 and L_2. When thoroughly analysing this equation, it does not hold when $2u + L_2 > R$, or $u > (R - L_2)/2$. The arcsine is undefined under these conditions. Bolsman found the following values to yield sweeping amplitudes of approximately $90°$: $L_1 = 2.2\ mm$, $L_2 = 0.5\ mm$ for a stroke of $\pm 3\ mm$. These values yield $(R - L_2)/2 \approx 0.88\ mm$, which is smaller than $u = 3\ mm$.

It is hypothesized that either the $3\ mm$ input is not the value used to determine the values for the design variables and/or the factor 2 in the denominator of the first arcsine term only works for the Cross Linkage Concept. Without this factor and taking $u = \pm 1.5\ mm$, $R - L_2 \approx 1.76$, and the equation holds. Then, using equation 2.1 and taking the sum of the outputs of positive and negative $1.5\ mm$ yields a displacement of $88.7°$.

Still, the formula does not hold for displacements larger than $R - L_2$. Also, it assumes the actuator can have a neutral position as shown in figure 2.1 and displace is both directions. In this configuration, both displacement directions require elastic deformation of the flexures and the central ring, requiring force. Therefore, only a push/pull actuator with a stroke of $1.5\ mm$ is accurately described using this formulation. A consistent formulation which includes push or pull actuators is in order.

$$\phi = \arcsin\left(\frac{2 \cdot u + L_2}{L_{tot}}\right) - \arcsin\left(\frac{L_2}{L_{tot}}\right) \tag{2.1}$$

$$\text{with, } L_{tot} = \sqrt{L_1^2 + L_2^2} \tag{2.2}$$

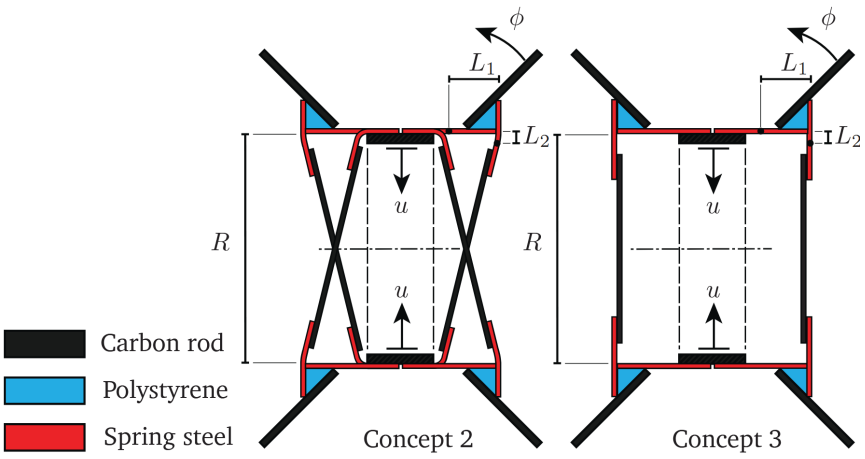


Figure 2.1: Schematics of the straight and the Cross Linkage Concept designed by Bolsman [29].

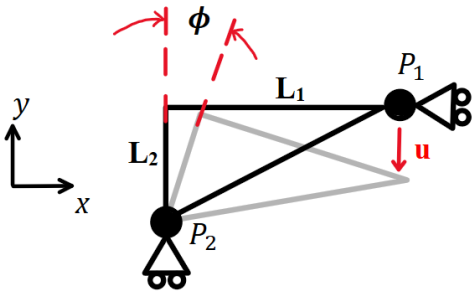


Figure 2.2: Simplified representation of a hinge corner rotation ϕ due to displacement u of the central actuator. Note the displacement u takes place on both sides of the mechanism, therefore, in this model, finding a value for u entails halving the actuator displacement. E.g. if an actuator displaces $2\ mm$, then $u = 1\ mm$

$$\text{for } u > 0 \wedge u < L_{tot}: \quad \phi(u) = \arcsin\left(\frac{u - L_2}{L_{tot}}\right) + \arccos\left(\frac{L_1}{L_{tot}}\right) \tag{2.3}$$

$$\text{for } u < 0 \wedge |u| < L_{tot}: \quad |\phi(u)| = \arcsin\left(\frac{|u| + L_2}{L_{tot}}\right) - \arcsin\left(\frac{L_2}{L_{tot}}\right) \tag{2.4}$$

$$\text{with, } L_{tot} = \sqrt{L_1^2 + L_2^2} \tag{2.5}$$

A new definition for the input/output relation of the Straigh Linkage Concept was found as described in equation 2.4 and 2.5. The formulation could be expanded to include the Cross Linkage Concept by adding the result of an additional u displacement at the bottom-left L_2 pin, but this is out of scope. The piecewise formulation depends on the direction of the displacement u. It is similar to the definition of Bolsman. For displacements in the negative u direction, where the central ring is enlarged, both descriptions are equal. For positive displacements u, but smaller than L_2, both definitions suffice as well and give similar outputs. When $u > L_2$, and the actuator position drops below the hinge center at the middle of the short flexure, the descriptions differ. This is common for pull actuators, such as many solenoids. The piecewise formulation will give a better estimation of the sweeping output at these displacements. In figure 2.3 the difference is shown when using Bolsman's Straight Linkage Concept design parameters. $L_1 = 2.2\ mm$, $L_2 = 0.5\ mm$ and $u = 1.5\ mm$. The piecewise expression for $\phi(u)$ can be used to define the effect of flexure geometries on expected outcomes.

Inversely, the expression can be used to estimate the linkage geometries based on a desired output. In literature, the required peak-to-peak sweeping amplitudes are found to be between 75 and $120°$ [29], [34]. Many different combinations of flexure lengths can be used to generate these sweeping outputs under

a $1.5\ mm$ actuator displacement. Manufacturability governs the choice of the flexure lengths. For large displacements, shorter flexures are needed.

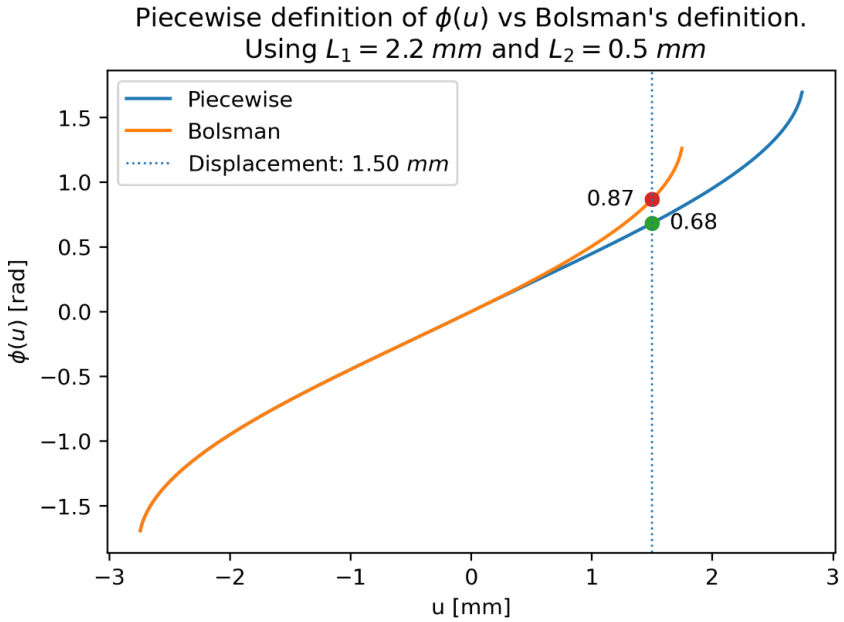


Figure 2.3: Difference in the definition of $\phi(u)$ for the Straight Linkage Concept when using Bolsman's or the Piecewise definition. At the proposed displacement of $u = 1.5\ mm$, the values differ. The discrepancy between the two models starts when $u \approx L_2$

2.2. Dynamics

2.2.1. Aerodynamics & Manoeuvre Forces

In order to control the Atalanta using stiffness modifications, steering torques have to be generated. The applied stiffness changes should tip, tilt or spin the whole drone, depending on the controlled degree of freedom. As the wings are offset from the center of mass of the drone, the distance between the center of lift and the center of mass can yield a torque. Therefore, asymmetric lift production between different wings can generate a torque directly proportional to the difference in lift between the two wings. To quantify the functioning of the Straight Linkage Concept, it is necessary to describe a performance variable indicative of the amount of steering that can be accomplished under a certain stiffness modification.

Both the linkage designs can be used to control the Atalanta when actively modifying the stiffness of specific flexures in the construction. However, the aerodynamic mechanism used for steering is different. As outlined in section 1.2.2, the Cross Linkage Concept is designed to modulate passive wing pitching through pitching hinge stiffness modification. A higher stiffness of the pitching hinge results in less passive pitching at the same sweeping amplitude. Due to its single DoF structure, the Cross Linkage Concept cannot modulate sweeping angle of individual wings with stiffness. The actuator and wing displacements are directly coupled. On the other hand, the Straight Linkage Concept is designed to modulate both the sweeping angle and the pitching angle by modulating stiffness in either of the corresponding hinges.

The effect of pitching and sweeping angles on the amount of lift generated by flapping wings is extensively researched for the Atalanta. Wang described the aerodynamics of a passively pitching wing using a quasi-steady model and found an optimal wing shape and passive pitching hinge location [34]. However, a full description of aerodynamic performance using passively pitching wings is out of scope for this thesis.

Changes in passive pitching hinge stiffness are found to modulate the angle of attack of the wing. The angle of attack defines the amount of lift. It should not be too high nor too low, as both of these states generate no lift. Changes in sweeping angle hinge stiffness alter the flapping amplitude at a given frequency. Higher speeds of the wing dictate higher lift generation, which is the sweeping amplitude divided by the period. If the sweeping amplitude is increased under the same period, the speed increases. However, if the sweeping amplitude becomes higher under the same frequency, the amount of passive pitching increases with it, which reduces drag and influences the dynamics of the system non-linearly [32].

For the Atalanta, the effect of modulations in pitching or sweeping on lift production of individual wings

has been described by Roulaux and Kottiswaran [42], [43]. It was found pure pitching hinge modulation can generate regimes where no lift is generated by the wing kinematics. On the other hand, sweeping angle modulation was found not generate such regimes.

From the outlined aerodynamics above, it is assumed the amount of lift in a system is directly proportional to the peak-to-peak sweeping amplitude at a given frequency. The exact lift generation of a specific wing remains unknown, while a peak-to-peak amplitude measurement together with a frequency will be indicative for the amount of lift generated. For simplicity sake, the lift force is averaged over a period of the flapping oscillation [29]. Other factors that generate lift, such as wing geometry, wing aerodynamic performance or external conditions are out of scope for this thesis. The pitching angle is also not included in measurements. It plays a role in aerodynamic performance, but can be modulated in both concepts to allow for optimal lift production at a specific sweeping angle.

To define necessary changes in lift for specific steering actions, a benchmark steering test was proposed by Peters [31]. Here, a two dimensional model of a drone was subjected different lift force modifications while performing a 0.5 m horizontal displacement as a flight manoeuvre. It was found a 5% change in lift would allow the modelled vehicle to perform the manoeuvre in less then 0.9 seconds.

Expanding this model to a four wing drone gives an indication on the lift force modifications required for rolling or pitching in the concept systems at hand. For the analysis, the four wings are assumed to be distributed radially symmetric. Now, the inertia for pitching and rolling is equal, and no distinction is made between these degrees of freedom. However, a yaw torque cannot be generated in this model. Figure 2.5 shows a simplified model of the four wing drone where the wing masses are modelled as points and the center of lift is assumed to be equal to the center of mass of the wings.

The inertia and torque of the two wing drone can be expressed as equations 2.6 and 2.7, respectively. For the four wing drone, inertia is the same when rotating over the x, y axes (equation 2.8), or the x', y' axes (equation 2.8). However, the amount of available lift is not the same, since two wings have no moment arm when rotating over the x', y' axes. The torque generated by rolling or pitching using two wings per side yields a factor of $\sqrt{2}$ more torque than in the two wing system. This effectively reduces the required change in lift by a factor of $1/\sqrt{2}$.

$$I_{2W} = I_r + 2m_w R^2 \tag{2.6}$$

$$T_{2W} = \Delta F_L R \tag{2.7}$$

$$I'_{4W} = I_r + 2m_w R^2 \tag{2.8}$$

$$I_{4W} = I_r + 4m_w \left(\frac{1}{2}\sqrt{2}R\right)^2 = I_r + 2m_w R^2 \tag{2.9}$$

$$T'_{4W} = \Delta F_L R \tag{2.10}$$

$$T_{4W} = 2\Delta F_L \left(\frac{1}{2}\sqrt{2}\right) R = \sqrt{2}\Delta F R \tag{2.11}$$

$$\tag{2.12}$$

No direct yaw control torque can be generated when basing the controls on cycle averaged lift forces, since the lift vector of each of the wings is pointed perpendicular to the plane spanned by the wings. However, it is possible to generate a net yaw torque when performing the following rotations in a local frame of reference: Pitch-up + Roll-left + Pitch-Down + Roll-right. This is due to the non-commutativity of 3D rotations. It is unknown if this is sufficient for yaw control of the four wing drone.

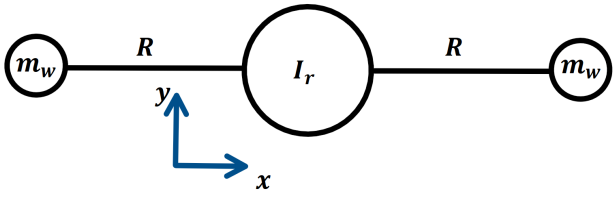


Figure 2.4: Model to study inertia effects of a two wing drone, similar to the model used by Peters [31].

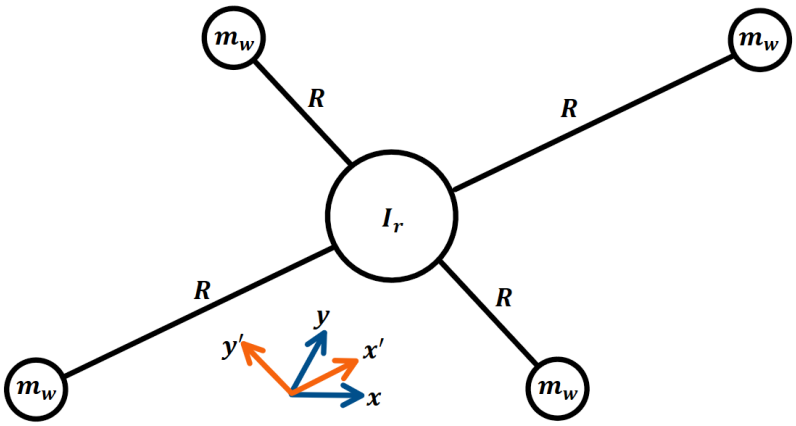


Figure 2.5: Model to study inertia effects of a four wing drone, akin to the two concepts currently under study.

2.2.2. Resonance of Damped Linear Systems

The resonance behaviour of linear mechanical systems is thoroughly described in literature on structural mechanics using modal analysis [18], [44]–[46]. Based on Newton's laws and Lagrangian energy methods, the differential equations governing the vibrations of discretized linear multiple-degree-of-freedom (MDOF) systems can be described, as shown in equation 2.13. Solving the differential equations of the MDOF system will yield a kinematic description of the motion under perturbation or excitation, which are called the equations of motions (EoM). The EoMs are governed by mass, stiffness, damping, and the distribution thereof. This is described in system matrices $\mathbf{M}$, $\mathbf{K}$ and $\mathbf{C}$, respectively. The EoMs can be found using a method called *modal decomposition*, which greatly reduces the computational effort of solving the differential equations.

In order to find the solution to the differential equations, an eigenvalue problem can be solved to rewrite a system of n-DOF into n independent differential equations. The eigenvalue problem is shown in equation 2.14, where ω_k^2 is the k^{th} eigenvalue corresponding to eigenvector $\mathbf{x}_k$, at a frequency of ω_k $[rad/s]$. This is called *modal analysis*.

$$\mathbf{M}\ddot{\mathbf{q}} + \mathbf{K}\mathbf{q} = \mathbf{0} \tag{2.13}$$

$$(\mathbf{K} - \omega_k^2\mathbf{M})\mathbf{x}_k = \mathbf{0} \tag{2.14}$$

$$\text{or with damping,} \quad \mathbf{M}\ddot{\mathbf{q}} + \mathbf{C}\dot{\mathbf{q}} + \mathbf{K}\mathbf{q} = 0 \tag{2.15}$$

In modal analysis, the equations of motion are rewritten in an orthogonal basis, wherein the degrees of freedom are decoupled. This is called modal decomposition, which is common practice in the numerical analysis of dynamic structures [18]. Using modal decomposition is computationally efficient because each DOF in a large MDOF system can be described independently of all the other DOFs. Decoupling the equations of motion yields modified mass, stiffness and damping matrices, written in an orthogonal basis of eigenvectors. These modal matrices are denoted using $\bar{\mathbf{M}}$, $\bar{\mathbf{K}}$ and $\bar{\mathbf{C}}$. Written in this orthogonal basis of eigenvectors, the $\bar{\mathbf{M}}$ and $\bar{\mathbf{K}}$ matrices are diagonal. For the damping matrix, a matrix element of $\bar{\mathbf{C}}$ for two distinct eigenmodes is described using equation 2.16, which shows the damping matrix is generally not diagonal. It defines where in the system damping occurs and couples the different degrees of freedom as $\mathbf{C}$ is not diagonal. Therefore, conservative systems are more computationally efficient to solve using modal decomposition than non-conservative or damped systems.

$$[\bar{\mathbf{C}}]_{ks} = \beta_{ks} = \mathbf{x}_s^T\mathbf{C}\mathbf{x}_k \neq 0, \text{for } s \neq k\ . \tag{2.16}$$

In conservative systems (eq. 2.13) each DOF can be analysed separately using the modal decomposition, in damped systems they generally can not. Only under the assumption a system has proportional damping and is lightly damped the coupling effects can be approximated and a modal decomposition is possible.

This approximated description of coupled damped systems in terms eigenmodes can be written, as long as the eigenfrequencies of the system are far apart, and the influence of damping on the system is low compared to mass and stiffness [18]. Now, each DOF has its own specific damping term dependant on the damping in all the other DOFs. The method entails computing the eigenfrequencies ω_k and eigenmodes $\mathbf{x}_k$

of the undamped freely vibrating system of equations 2.13. Then, each k^{th} damped eigenmode $\mathbf{z}_k$ can be described in terms of modal mass μ_k and modal damping β_{ks} in equation 2.19. This equation shows the damping influence of mode s on mode k. For each mode, the influence of all the other modes is calculated in a weighted sum. Finally the response $\mathbf{q}$ can be written in terms of $\mathbf{z}$ (eq. 2.20).

What can be seen in equation 2.19, is that closely spaced eigenvalues ω_k and ω_s result in larger coupling terms in the damped eigenmodes. Furthermore, the coupling term creates a complex eigenmode, which captures a phase relation between different modes. In the conservative system, all eigenmodes present in a response $\mathbf{q}$ move in phase. In the free vibration of damped systems, a phase shift will occur between different eigenmodes present in the response.

$$\mathbf{K}\mathbf{q} + \mathbf{C}\dot{\mathbf{q}} + \mathbf{M}\ddot{\mathbf{q}} = \mathbf{0} \tag{2.17}$$

$$\left(\mathbf{K} - \omega_k^2\mathbf{M} + i\omega_k\mathbf{C}\right)\mathbf{z}_k = \mathbf{0} \tag{2.18}$$

$$\mathbf{z}_k = \mathbf{x}_k + \sum_{\substack{s=1 \\ s\neq k}}^{n} \frac{i\omega_k\beta_{ks}}{\mu_s(\omega_k^2 - \omega_s^2)}\mathbf{x}_s \tag{2.19}$$

$$\mathbf{q} = \mathbf{z}e^{\lambda t} \tag{2.20}$$

Forced vibrations require the analysis to be expanded with a forcing term $\mathbf{p}(t) = \mathbf{f}e^{i\theta t}$, where θ is the angular frequency of the excitation. The influence of the excitations $\mathbf{f}e^{i\theta t}$ on the response $\mathbf{q}(t)$ can be computed by solving the eigenvalue problem of equation 2.23. Here, $\mathbf{z}$ are complex eigenmodes constructed through modal expansion in the form of equation 2.24. The coefficients α_s in equation 2.25, show the influence of the s^{th} undamped mode $\mathbf{x}_s$ and the forcing term $\mathbf{p}(t)$ on response amplitude $\mathbf{z}$. Because of the forcing, $\mathbf{z}$ is not an eigenmode, rather an amplitude as a sum of contributing eigenmodes, and thus on solution $\mathbf{q}$ of equation 2.22. The relative contribution of each undamped mode $\mathbf{x}_s$ is dependant on the force amplitude $\mathbf{f}$, the excitation frequency θ and the modal contributions of mass, stiffness and damping. What can be seen in this description, is that an excitation vector $\mathbf{f}$ orthogonal to eigenmode x_s will yield no contribution of this mode to the eigenvector $\mathbf{z}$.

$$\mathbf{K}\mathbf{q} + \mathbf{C}\dot{\mathbf{q}} + \mathbf{M}\ddot{\mathbf{q}} = \mathbf{p}(t) = \mathbf{f}e^{i\theta t} \tag{2.21}$$

$$\text{And,}\quad \mathbf{q} = \mathbf{z}e^{i\theta t} \tag{2.22}$$

$$\left(\mathbf{K} - \omega^2\mathbf{M} + i\omega\mathbf{C}\right)\mathbf{z} = \mathbf{f} \tag{2.23}$$

$$\mathbf{z} = \sum_{s=1}^{n} \alpha_s\mathbf{x}_s, \tag{2.24}$$

$$\text{wherein,}\quad \alpha_s(\theta) = \frac{\mathbf{x}_s^T\mathbf{f}}{\mu_s\left(\omega_s^2 - \theta^2 + 2i\varepsilon_s\theta\omega_s\right)} \tag{2.25}$$

$$\text{With,}\quad \varepsilon_s = \frac{\beta_s}{2\omega_s\mu_s} \tag{2.26}$$

$$F_d = \frac{1}{2}C_D S\rho(L\dot{\phi})^2 \tag{2.27}$$

As the amplitude $\mathbf{z}$ of response $\mathbf{q}$ is the superposition of all eigenmodes, a response at different frequencies θ can be found. If θ is close to an eigenfrequency ω_s, the contribution of an eigenmode $\mathbf{x}_s$ increases through $\omega_s^2 - \theta^2$. When damping is present in the system, the numerator of equation 2.25 is non-zero and a maximum amplitude contribution is reached. Together with the modal contribution of all the other modes, a total amplitude is obtained.

This theoretical framework gives an indication on the interplay between forced vibrations of structurally damped linear systems and the eigenmodes thereof. However, for the Atalanta, the response amplitude at resonance is likely to be non-linear and structurally damped. Most dissipation in the system is centered near the wings through aerodynamic drag. Now, for simplicity sake, $\mathbf{q}_w$ will denote the position of the DoF of a wing. This drag force is proportional to the squared rotational velocity of the wing, or $F_d \propto \dot{\mathbf{q}}_w^2$, through equation 2.27 [29]. Here, C_D is the drag coefficient of the wing, S is the surface area of the wing, L is a characteristic length to convert the rotational velocity to linear velocity, and ρ is the air density. As the wing velocity is governed by the vibration amplitude $\mathbf{q}_w$ divided by the period ω, the non-linear damping will yield a damping formulation where the modal terms are proportional to the amplitude.

On top of that, wings reliant on the passive pitching mechanism yields another non-linear effect. Through the passive pitch mechanism, higher amplitudes yields more pitching of the wing, away from a neutral

vertical position. Therefore, the drag force is reduced at higher amplitudes and an inverse relation between amplitude and damping is obtained [32].

2.3. Experimental Framework and Requirements

2.3.1. Experiment

Summarizing the findings in the previous and current chapters yields a design space for prototypes and experiments. To reiterate, the research question at hand asks to find the effect of the Straight Linkage Concept on steering capabilities, when using structural property modifications as a control input. As stated, several variables influence the amount of lift generated per wing, and thus the steering capabilities of a design. These variables are frequency, sweeping and pitching amplitude, structural and aerodynamic properties of the wings, structural properties of the linkage mechanism, and the structural properties of the drone itself. A full theoretical description of the effects of these variables on the non-linear lift and drag generation and non-proportional damping in the vibrating aerodynamic system are thought to be too computationally expensive to fully describe. Instead, the listed theoretical framework drives the research focus on experimentally observing the dynamics at resonance.

Conceptually, the easiest comparison would be to design two fully integrated lift generating devices outfitted with either the Cross or the Straight Linkage Concept together with smart materials capable of structural property modifications. Then, an equal input control signal could be directly related to different output angular accelerations for each device. However, when realizing this experiment, the influence of manufacturing error will be too high to make a fair comparison. The current research on consistent manufacturing procedures for wings and smart materials in the Atalanta is still open. Small changes in wing performance due to manufacturing error might be enough to create a steering motion, as only 1% lift changes are shown to generate control torques [31]. The manufacturing know-how is likely to exist in the general body of knowledge, but it is currently not integrated within the Atalanta project. Due to time constraints, researching accurate and repeatable manufacturing methods for wings and smart materials, together with measuring dynamic performance, is out of scope for this thesis.

Because of the manufacturing limitations, a simplified experiment is designed to resemble the fully integrated Atalanta FWMAV as closely as possible within the time constraints of the thesis. The prototype will have four wings, and a central actuator and a central ring flexure. Two linkages with each two wings will translate linear motion of the central actuator to reciprocating rotational sweeping motion of the wings. The experiment is focused around observations of the resonant dynamics of the Straight Linkage Concept. Its response modifications due to passive variations in stiffness are to be investigated. By measuring changes in wing sweeping amplitude, and using the fact that lift is directly proportional to amplitude at a given frequency, steering capabilities will be inferred.

Variations in stiffness are chosen to be passive in order to prevent the research to be limited by smart material manufacturing. Furthermore, variations in stiffness are chosen over other structural property modifications, as this was found to be easiest to realize in smart materials [47].

Furthermore, in order to limit the influence of non-linear damping and individual wing performance due to manufacturing, the passive pitching hinge will be omitted from the wing design. Wings will be idealized as rectangular slabs and will not generate lift, but are required to generate sufficient drag. Therefore, the wings should have same frontal surface area as the optimal wings found by Wang [34].

2.3.2. Requirements

A list of requirements is outlined below:

- It is unknown what an optimal sweeping hinge stiffnesses is. Stiffness values mentioned in literature by Diekerhof and Bolsman indicate 98 Nmm/rad and 11 Nm/rad, respectively [29], [48]. The sweeping hinge stiffness is required to be in the same order of magnitude or lower, as lower stiffness are thought to yield higher amplitudes at the same force input.
- It is unknown what an optimal central ring stiffness is. Stiffness values mentioned in literature by Bolsman indicate 0.2 to 0.4 N/mm for linear displacements [29]. The central ring stiffness is required to be in the same order of magnitude or lower, as lower stiffness are thought to yield higher amplitudes at the same force input.
- It is unknown what the stiffness accuracy needs to be in order to have equal sweeping amplitude over all wings, as the sensitivity of the structure to changes in stiffness is unknown. The criteria is to be as accurate as possible given the time constraints within the thesis. Furthermore, it is required that

the hinge sweeping hinge stiffness of each wing is as equal as possible, before applying stiffness variations.

- Wing damping and mass requirements are in the order of magnitude of the optimal wing by Wang, which is governed geometrically by wingspan $R = 50\ mm$ and surface area of the wing which is approximately $1000\ mm^2$. Wing mass is $50\ mg$ [34].
- Overall scaling is 1:1 because the flapping dynamics are non-linear in speed due to damping. Making the prototype bigger will require extra computational steps to infer performance based on measured sweeping displacements.
- Buying new material and equipment is limited to cost € 150 at most, as this is made available through the institution.
- Due to time constraints, the design and manufacturing approaches are constraint to the methods known by, and availability to the author.

3
Experimental Methodology

In this chapter, the methodology of this research is outlined. It aimed to provide insight in the effect of structural stiffness variations on the resonant response of vibrating compliant mechanisms. Specifically, as outlined in chapter 2, the device at hand was a multi degree of freedom flapping-wing micro air vehicle (FWMAV) with compliant hinges, called Atalanta. The device contained two linkage systems which transfer the driving force of a central actuator to four reciprocating wings.

This chapter is organized as follows. First, the design and manufacturing of the research prototype is elaborated upon, together with the methods of stiffness variation. Secondly, the design and realization of a stiffness measuring protocol is explained, which was based on the comparison between a numerical model and physical measurements. Thirdly, the design and implementation of two experiments setups are shown, which measure amplitude and phase of the wings under variable stiffness and frequency. The measurements are combined with a numerical modal analysis. Their respective data processing procedures are described. The amplitude experiment sheds light on the steering capabilities of the Straight Linkage Concept. The phase experiment takes stroboscopic slow motion videos in order to analyse the dynamic response of the Concept.

3.1. Prototype Design & Manufacture

3.1.1. Research Prototype Design

The prototype was designed to be a representation of the Atalanta, incorporating a central actuator, a central ring flexure, two linkage systems and four wings. The practical constraints and requirements outlined in section 2.3 governed the manufacturability and functioning of the mechanism while not overcomplicating the prototype by being directly implementable in a lift-off capable version of the Atalanta. Design decisions were prioritized on displaying the effects of local increased stiffness on the relevant resonant dynamics.
The designed and manufactured prototype is shown in figures 3.1 and 3.2. Autodesk Fusion 360 was used to for Computer Aided Design (CAD) modelling and to generate `.stl` and `.dxf` files. The `.stl` files were used in a masked stereolithography apparatus (mSLA) 3D printer called the Formlabs Form 4 to create plastic parts out of polymer resin. The `.dxf` files were used in a fiber laser cutting machine called the Lion Alpha Metal XL to create flexures out of steel sheet.

The prototype consisted of flexures and rigid bodies. In the middle of the prototype, a compliant sheet steel ring with a thickness of $0.15\ mm$ was placed, housing a central solenoid actuator. On either side of the central ring, a connector body coupled a linkage mechanism to the ring and the central actuator. These bodies are called *central ring connectors*. The compliant linkage mechanism connected two wings on either side of the central actuator. To dampen the resonant state, a wing-like rectangular sheet was attached to each corner of the linkage, at a *wing connector*. The two wing connectors are in turn coupled by *side connectors*. Each of the bodies in the linkage system is connected by a flexure in a chain, combining to three bodies and four flexures per linkage. This design is the Straight Linkage Concept designed by Bolsman, as described in section 1.2.2 [29].

The research prototype was not designed to be capable of lift-off. In fact, the stator of the actuator is rigidly attached to a baseplate through the *connector rod*, as shown in figures 3.3c to 3.3e. Another, free floating configuration was designed by Bolsman [29]. Here, the prototype was suspended from two electrical wires attached to the central solenoid. The rigid attachment configuration was chosen to get a more accurate reading of the wing displacements without having to take rigid body motions into account. If, during measuring, the vibrations cause a suspended prototype to drift in global position, an extra computational step would be required to track the orientation of the drone to a global reference frame. A downside to this configuration was the effect on the dynamics of the mechanism. In the free floating Atalanta, the stator and plunger would both vibrate. Now, only the plunger oscillated. The implication of this configuration was studied in the numerical modal analysis of section 3.2.

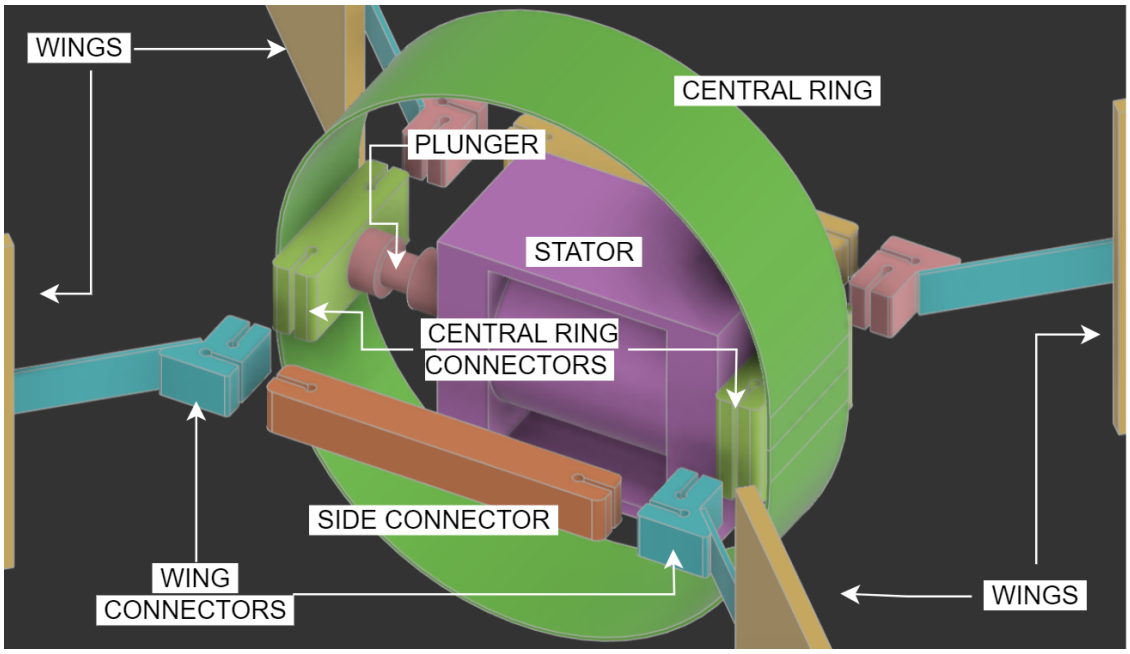


Figure 3.1: View of the research prototype mechanism in CAD. The flexures are not modelled and are designed to fit in the slots of the connector bodies.

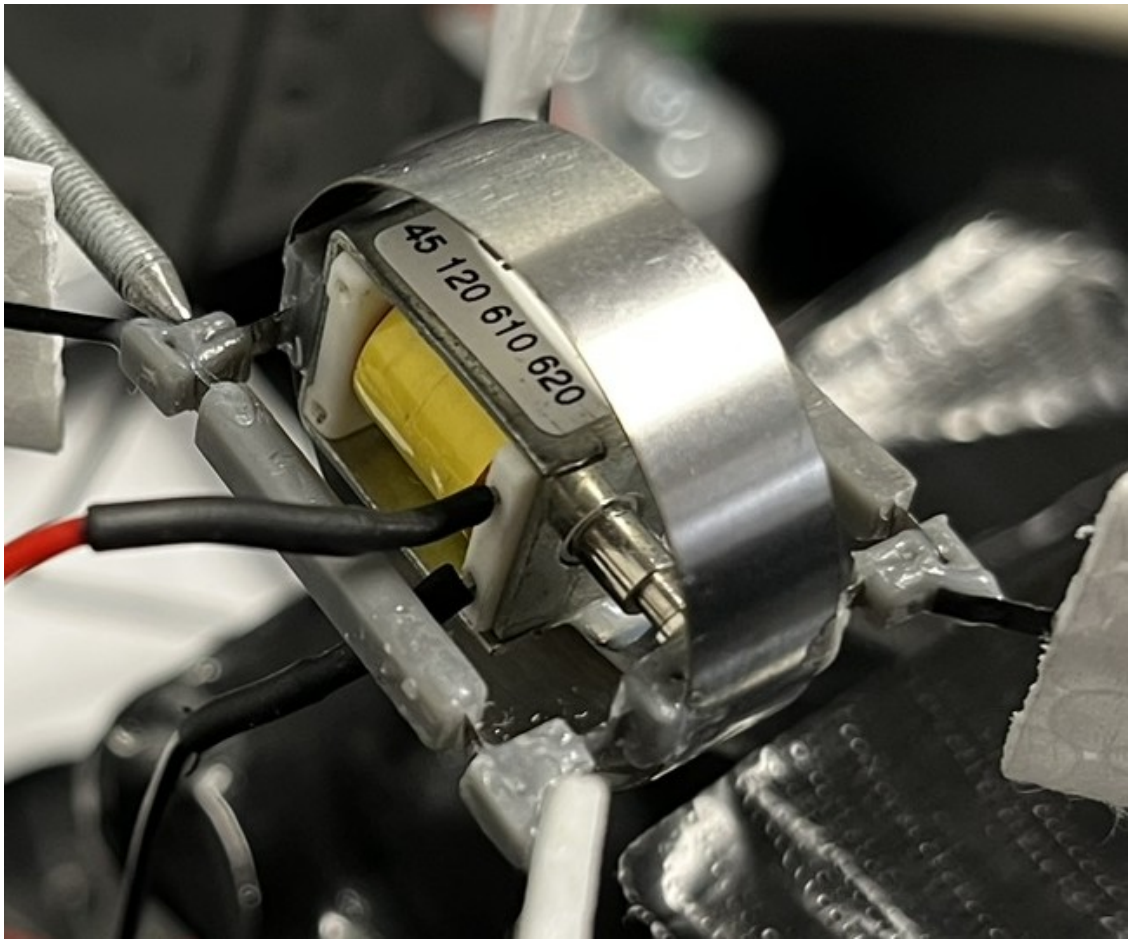
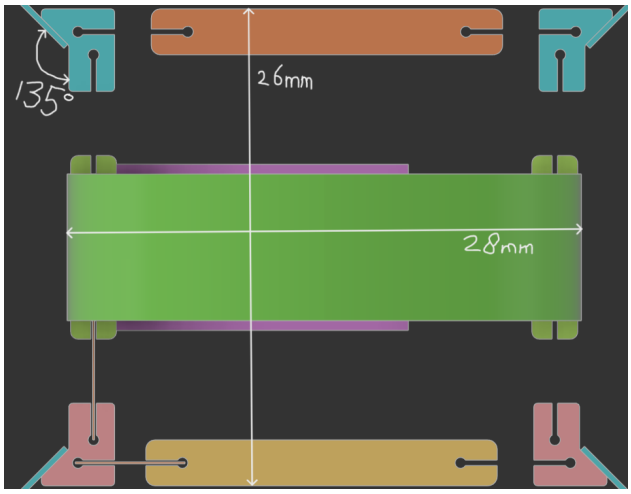
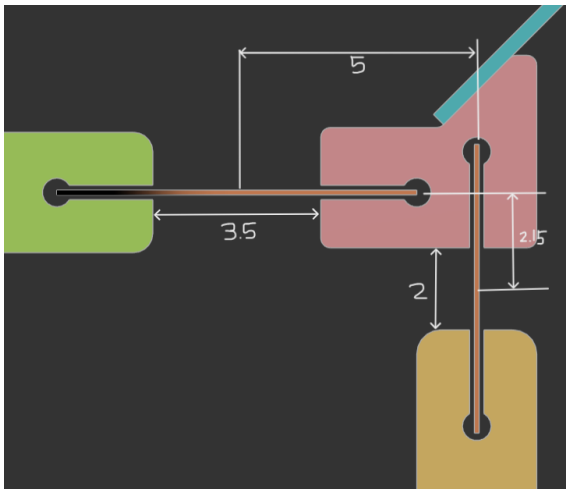


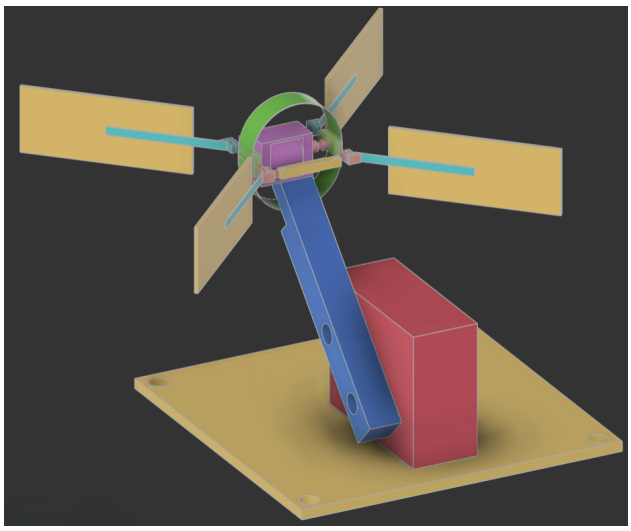
Figure 3.2: View of the physical research prototype. The red and black wires are the leads of the solenoid. The screw in the top left corner is a measurement pin used in stiffness measurements, as outlined in section 4.3.2. Information on the functioning of the realized device are found in section 4.1.



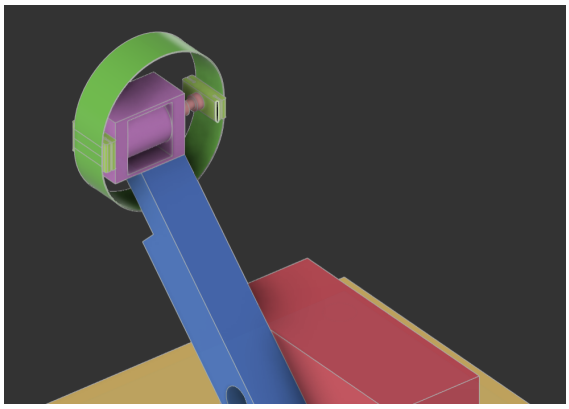
(a) Top view of the linkage mechanism, without flexures drawn.



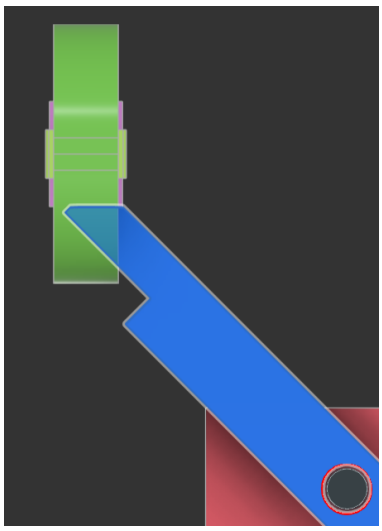
(b) Dimensions of a linkage corner where the wing connectors are attached to the central ring connectors and the side connectors. A wing is attached to each wing connector.



(c) Assembly of the prototype connected to the baseplate.



(d) Attachment of central actuator to the baseplate. Wings and linkages are not modelled to show how the connector rod is inserted into the mechanism.



(e) Side view of a the connection between the rod and the stator in the central ring. For the ring functioning it is required that the rod does not interfere with ring deformations.

Figure 3.3: Design of the prototype modelled in CAD.

3.1.2. Design Choices

This section outlines relevant design choices and prototype parameters. The design choices are primarily governed by manufacturability and rapid prototyping. Several manufacturing processes were considered before the prototype was designed. The precision of the manufacturing method governs the spread in the sweeping hinge stiffness between wings.

Manufacturing Method

For precision and versatility, the most appropriate manufacturing choice was found to be stacked sheet manufacturing. This method involved laser cutting sheets of different materials and glueing them together. Sheets of compliant and rigid materials could be specifically alternated in order to create a compliant mechanism [49]. This method would be favourable because of its precision, but requires specialized materials or laser cutters. Often, laser cutting machines are able to cut either plastics or metals. Laser ablating machines capable of cutting both materials simultaneously were available to the author, but only on a scheduled and supervised basis. On the other hand, 3D printers and metal laser cutters were generally available for unsupervised use, allowing faster prototyping and iteration.

To avoid the use of laser ablation machines, tests were done on cutting stacked layer materials with a fiber laser. The tests were performed on a sandwich structure of three layers. A layer of 0.05 mm thick 1.4310 stainless steel was sandwiched between two layers of 0.45 mm thick 3D printed polylactic acid (PLA) plastic and, bonded using a thin (not measured) layer of cyanoacrylate glue. When cutting, the steel sheets were not fully cut through, the PLA melted and delaminated from the steel. It was not possible to t

Furthermore, designing for stacked sheet manufacturing requires monolithic designs which are folded into shape. The time to design and model the necessary folding patterns was out of scope for this thesis. Also, the materials used in stacked sheet manufacturing are not trivial. Especially the glue layer in between the rigid or compliant layers had to be able to withstand the peel forces under large deflections, and be available for very low quantity purchasing under the budget constraints of € 150. Spring steel flexures and 3D printing materials were provided by the faculty, and did not require to be included in the budget. This kept the budget open for other prototyping materials or measurement setup equipment.

Flexure Design

The flexure lengths are chosen to be manufacturable, while still displaying measurable amplitudes. From figure 3.3b it can be seen that the thickness of the rigid pieces had to be balanced with the length of the flexures to prevent collision during sweeping, as it was not known beforehand how much amplitude increase will be generated by driving the system at resonance. Therefore, flexure lengths were not governed by optimal linkage efficiency, but by manufacturability and collision avoidance.

The flexures of the sweeping hinges were designed to be made from 0.05 mm thick 1.4310 stainless steel, as this was the thinnest steel sheet material available in stock in the Faculty Workshop. Steel was used for its fatigue strength limit to prevent the possibility of failure under oscillations.

The geometry of the flexures governs the expected stiffness of the hinges. The stiffness values of the designed flexures were lower than the values stated in section 2.3. Each corner hinge has a long and a short flexure, as shown in figure 3.3b. The stiffness of the corner hinge was estimated by looking at the stiffness of the two flexures, when modelling them as pin joints with purely rotational stiffness [50]. Using $k_i = EI/L$, then the long 3.5 mm flexure will have a stiffness of $k_{long} = 1.3\ Nmm/rad$. The shorter 2 mm flexure will have a stiffness of $k_{short} = 2.2\ Nmm/rad$.

From the derived Piecewise formulation for sweeping angle (eq. 2.5), the used flexure lengths for the top flexure and the side flexure of 3.5 and 2 mm respectively, are not able to generate sweeping angles that could generate lift. This was assumed to be reasonable as the prototype was not required to generate lift. The discussions in section 5 shed light on the limitations of this choice. The designed dimensions and actuator displacement yield an L_1 and L_2 of 5 and 2.15 mm, respectively. As $u = Stroke/2$ =3.15/2 mm, this would generate a theoretical sweeping amplitude of approximately $17°$.

Inverting the piecewise function to calculate L_1 and L_2 lengths based on actuator input $u = 3.15/2\ mm$ and a desired peak-to-peak sweeping amplitude of $75°$ [29], yielded multiple length combinations. An optimal design is governed by manufacturable flexure. Now, a combination of $L_1 = 0.98\ mm$ and $L_2 = 0.90\ mm$ was found to be most manufacturable, as other combinations lowered one dimension to increase the length of the other dimension.

Designing a hinge with these dimensions requires the centers of the flexures to be close to the plane of the other flexure, per the definition of L_1 and L_2 in figure 2.1. This would require the design to withstand high peeling forces, similar to how the spring steel flexures are glued to the polystyrene in the aforementioned

figure. Without support material on both sides of the flexure, peeling loads start to limit the allowed flexure deformation. Therefore, it was chosen not to follow the design rules outlined in section 2.1.

The central ring was designed to be manufacturable. The ring was formed into a ring shape, before it was placed into the prototype. This prevented a preload in the material. This bending procedure is outlined in section 3.1.3. The central ring was made from 0.15 mm thick 1.4310 stainless steel sheet, using a radius of 28 mm. This material thickness was used because it was less prone to bending in faulty directions when manufacturing the ring, compared to using the 0.05 mm material thickness. The stiffness of the central ring was estimated using a strain formula, outlined by Young [51], as shown in equation 3.14. The found stiffness is higher than the required 0.2-0.4 N/mm order of magnitude.

$$\frac{1}{k_r} = \frac{R^3}{EI}\left(\frac{g_1}{2} - g_2 + 2g_2^2\right) \tag{3.1}$$

$$EI = \frac{Ew_r t_r^3}{12} \tag{3.2}$$

$$g_1 = 1 - \alpha + \beta \tag{3.3}$$

$$g_2 = 1 - \alpha \tag{3.4}$$

$$\alpha = \frac{I}{AR^2} \tag{3.5}$$

$$A = 2\pi R t_r \tag{3.6}$$

$$\beta = \frac{4EI_r}{\pi GAR^2} \tag{3.7}$$

$$G = \frac{E}{2(1+v)} \tag{3.8}$$

$$v = 0.3 \tag{3.9}$$

$$R = 14\ mm \tag{3.10}$$

$$w_r = 8\ mm \tag{3.11}$$

$$t_r = 0.15\ mm \tag{3.12}$$

$$E = 200 \times 10^3\ N/mm^2 \tag{3.13}$$

$$k_r \approx 1.2\ N/mm \tag{3.14}$$

Rigid Part Design

Rigid and flexure parts were designed to be manufacturable using 3D printing and laser cutting. The size of the 3D prints was based on the slit size for mounting the flexures connector pieces. A minimal dimension of 1 mm was used, which was based on experience with resin 3D printing in Formlabs machines, and generated consistent results. The strength and stiffness of the rigid pieces was assumed to be sufficient under the loads of the prototype.

Two glueing methods were used to join parts together. All connections were glued, except for the attachment of the connector rod to the baseplate, shown in figure 3.3c. Both methods consisted of glueing parts together. The first method consisted of directly glueing two surfaces together. This was considered sufficient for attachments with low peeling load. For high peeling load attachments, slits were used to insert a flexure into a rigid body.

The slits in the rigid parts were designed to be 0.3 mm to allow 0.05 mm flexures to be fully surrounded by glue. This would yield an approximate glue layer of 0.125 mm on each side. Shear strength of glue layers was not taken into account for the design of the joints, but the ISO 4587 shear strength test requires $0.2\ mm$ adhesive layer thickness. The placement of the flexure in the glue slit was performed by hand, so the $\pm$0.125 mm play between the flexure and the sides of the slit allowed for a proper adhesive layer thickness no matter the position. Together with the 1 mm minimal dimension, a minimal thickness of the rigid pieces of 1+1+0.3 = 2.3 mm was required. The height and width of the rigid elements were chosen to be minimally 2.5 mm for design convenience.

Actuator Choice

The used actuator is the *Series 45D Miniature printed circuit mount solenoid*, `S/N:45D120610620`, manufactured by BLP Components Ltd. For the Atalanta research project, many earlier contributors bought useable actuators. The actuator choice was based on availability within the project. This exact actuator was used to drive a similar prototype based on the Cross Linkage Concept, as shown in figure 1.1 [29], and therefore deemed adequate.

The actuator is capable of applying a force at 12 V under continuous current, measured to draw approximately 0.12 A. The actuator can output approximately 0.3 to 0.9 N at a 50% duty cycle, according to the data sheet. No higher voltages were used to continuously drive the system, as this would heat up the solenoid. As the actuator was glued to the connecting rod and the central ring connectors, the possibility of overheating and weakening the glue had to be limited.

The actuator was designed to displace 3.15 mm, which was governed by the ring size used by Bolsman, the actuator dimensions and the central ring connector thickness. Per the data sheet of the actuator, the maximum stroke is 3 mm. The amount of force the actuator can provide is non-linearly dependant on the stroke amplitude.

The expected effect of constraining one side of the mechanism is that the constraint wings have slightly less displacement due to the kinematics. It is deemed insignificant at resonance as now stiffness governs the amplitude not kinematic efficiency.

Wing Design

The wings were designed as flat $1 \times 50 \times 20\ mm$ expanded polystyrene (EPS) foam rectangles, supported by carbon-fibre reinforced polymer (CFRP) bars glued to the EPS. The rectangle size was based on an estimation of the surface area of a wing designed by Wang [34]. The wing surface area is approximated by tracing the contour of the wing and extruding the surface in CAD. The surface area was found to be approximately 1004 mm^2.

The CFRP cross section was $0.3 \times 3\ mm$, which was based on material availability within the project. The position of the wing is placed $5\ mm$ away from the hinge. EPS was used to limit the wing mass while remaining rigid, weighing approximately $25\ mg$ per rectangle. The CFRP support lengths were $35\ mm$ and did not stretch to full wing length to limit wing mass. The supports were placed in the middle of the wing to limit wing twist under oscillations. Based on a CFRP density of 1.5 mg/mm^3, the support weighted approximately 50 mg. The total wing masses were measured to be in the same order of magnitude of the required wing mass by Wang of $50\ mg$, at $78.5 \pm 0.5\ mg$. Thirteen different materials were gathered and weighted, as shown in figure 3.4. The lightest material was chosen and no lighter materials were available to the author.

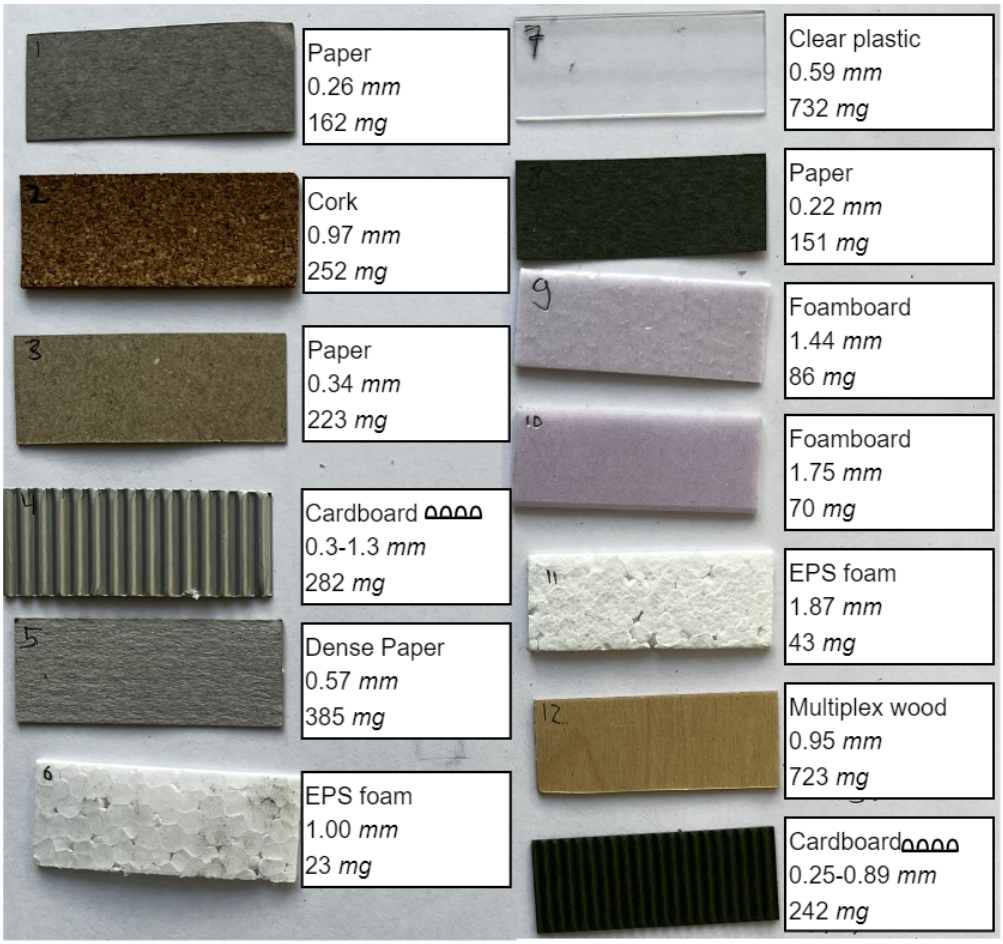


Figure 3.4: Sourced materials and their specifications. All materials were cut into 20 $\times$50 mm rectangles before weighing. The values for thickness and weight are reported in the figure. The cardboard materials list backing and rib dimensions. All other dimensions are sheet thickness.

3.1.3. Manufacturing Procedures & Inducing Stiffness Variations

This section outlines manufacturing steps and procedures. As stated, the manufacturing methods consist of glueing together 3D printed rigid parts and laser cut flexures. The precision of the manufacturing method governs the spread in the sweeping hinge stiffness between wings.

Flexure Manufacturing

The flexures were cut from stainless steel 1.4310 sheet using the Lion Alpha Metal XL fiber laser cutter. The laser cutting process created burrs on the sides of the flexure, increasing their stiffness. These burrs were removed using 400 grit sandpaper. The central ring flexure was formed into shape by rolling the flexure over a 5 mm diameter steel round stock bar. Using trial and error, it was found this diameter worked best. The process is shown in figure 3.5.

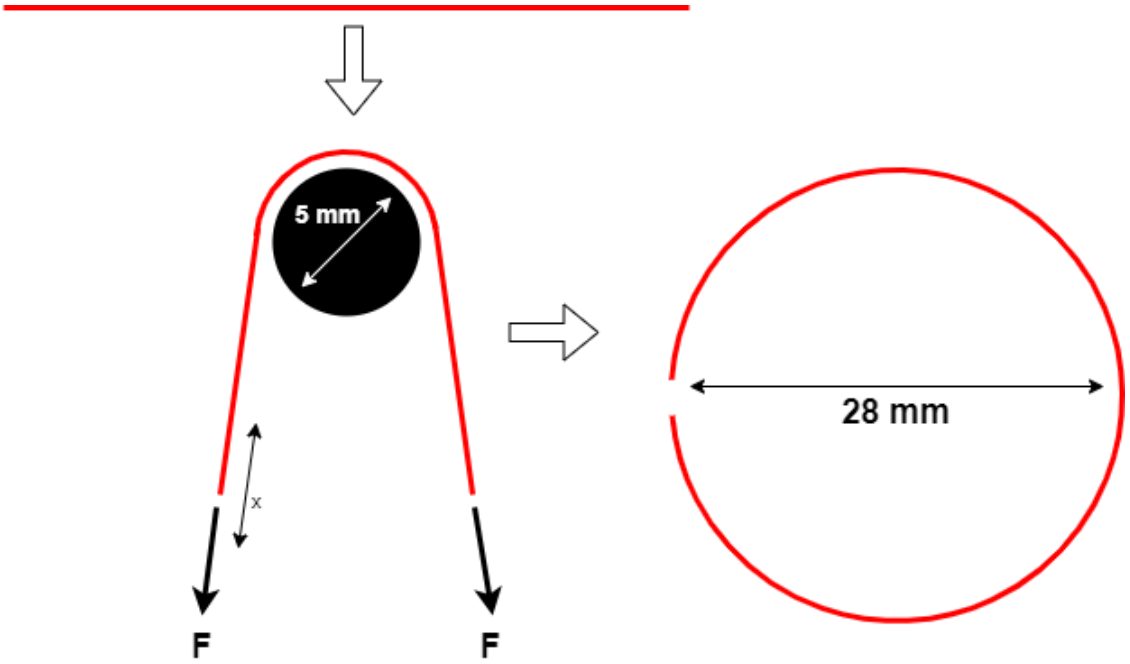
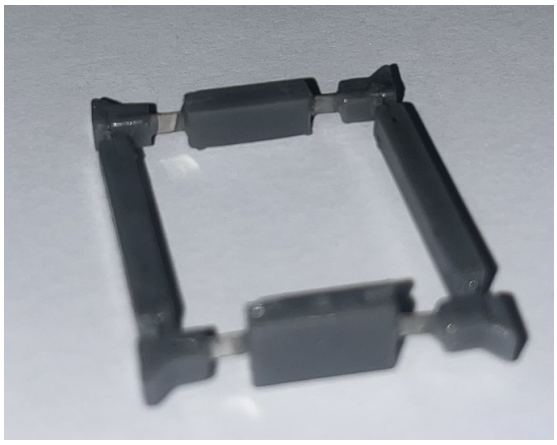


Figure 3.5: Schematic depiction of forming a ring flexure from a flat sheet. When applying a tangential force F on both ends of the flexure using pliers, and moving the material back and forth along x over the 5 mm round stock, a radius of approximately 28 mm was achieved.

Glueing

The sub-assemblies of the prototype were primarily made out of spring steel flexures and resin epoxy. The flexures were glued into place using 2-component epoxy glue, Henkel Loctite EA 9466 [52]. This glue was chosen because of a long, room temperature induced curing time of 180 minutes. This aids in the assembly of the mechanism, because alignment issues can be restored. Furthermore, it is listed to have a large 180° peel strength, which is necessary when the flexures bend outward due to loading.

Because of the curing time, the prototype assembly was longer than expected. Because of manufacturing tolerance, preloads existed in the material, and sub-assemblies had to be held in place for a prolonged time, before a new part could be attached. First, each flexure was combined with a rigid piece. Then, after drying, two flexure-rigid assemblies could be combined to form a chain of two flexures and two rigid parts. This process was continued until a ring of flexures and rigid parts was created, shown in figure 3.6a. Thereafter, the actuator was placed inside the linkages. Finally, the formed ring was glued onto the flexure. When the ring was glued, some extra pressure was used to keep the system in place, as shown in figure 3.6b. Then, the wings were glued on the wing connector pieces. Finally, the actuator was glued to the base connector rod (see figure 3.3d).



(a) Chain of flexures and rigid parts, making up two linkages. The actuator and ring were glued around this part.



(b) Flexures, actuator and ring flexure being held in place when curing the epoxy.

Figure 3.6: Intermediate gluing steps showing the compliant linkage chain (a), and the actuator being glued in place using a vice (b).

Realizing Stiffness Modifications

In order to create a variable stiffness in the structure, an extra piece of sheet steel was glued on top of the existing structure, using the same epoxy glue. This created a thicker cross-section. Because the sensitivity of the structure was unknown beforehand, it was also not known what the required stiffness changes were. Glueing this extra sheet provided a reasonable, low complexity method to increase stiffness. The placement is shown in figure 3.7.

Three stiffness configurations were realized using this method. The first is called the *Original* configuration, wherein all flexures are unmodified. The second is called the *Stiff V1* configuration, where flexure k_2 is modified. The third is called the *Stiff V2* configuration, where flexure k_3 is modified. Both stiffness increase locations are shown in figure 1.4.

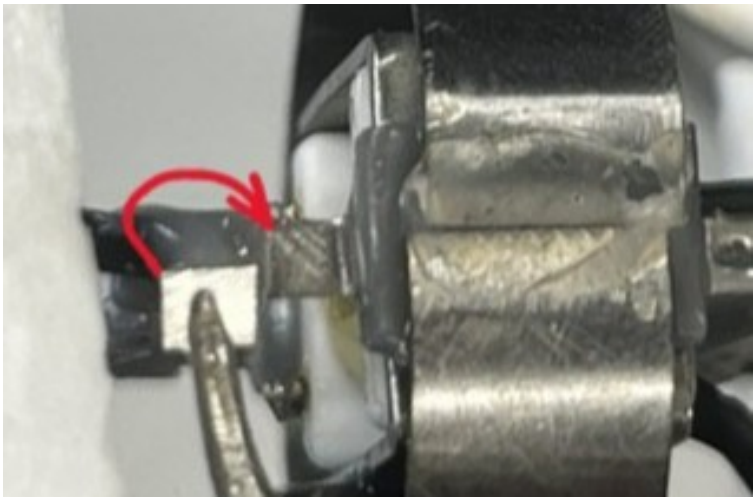


Figure 3.7: A stiffness increase was realized by gluing an extra sheet of metal over an existing flexure. The red arrow indicates the placement of this sheet, which is held with needle pincers.

Rigid Part Manufacturing

As stated, the rigid parts were printed on a Formlabs Form 4 mSLA 3D printer. The used material was Formlabs grey resin. Due to the small feature size of the slots that accept the flexures and glue some extra printing steps were found to increase print reliability. First of all, the prints were oriented in the direction of the slots. This was done to prevent support structures to be automatically generated within the 0.3 mm wide slots, which would be impossible to remove. Furthermore, before curing the resin prints, the slots were thoroughly cleaned to remove any excess resin. A regular ultrasonic cleaning procedure did not suffice, and the slots had to be cleared by using a thin and strong material, such as the metal sheets used for flexure laser

cutting. The slots were outfitted with a bigger cutout at the deepest part of the slot (see figure 3.3b). These cutouts were designed to aid in assembly by increasing play. This was thought to minimize the preload on the linkage chain when misalignments occurred.

3.2. Measuring Stiffness

3.2.1. Estimating Flexural Rigidity

The stiffness measurements are based on an estimation of the flexural rigidity of the flexures. As it is unknown what the influence of glued endpoint connections is on the flexural rigidity of the flexures, the physical prototype is compared to a numerical model. The found flexural rigidity was then used to calculate the stiffness of the flexures by modelling them as torsion springs using the psuedo-rigid body method (PRBM) [50]. Using the PRBM, flexures which function as torsion can be assumed to have the stiffness expression of equation 3.15.

$$k_i = \frac{EI_{real}}{L_i} \tag{3.15}$$

$$E_{steel} = 200 \times 10^3 \ N/mm^2 \tag{3.16}$$

$$t = 0.05 \ mm \tag{3.17}$$

$$w = 2 \ mm \tag{3.18}$$

$$I = \frac{wt^3}{12} \ mm^4 \tag{3.19}$$

$$EI_{FEM} = 4.167 \ Nmm^2 \tag{3.20}$$

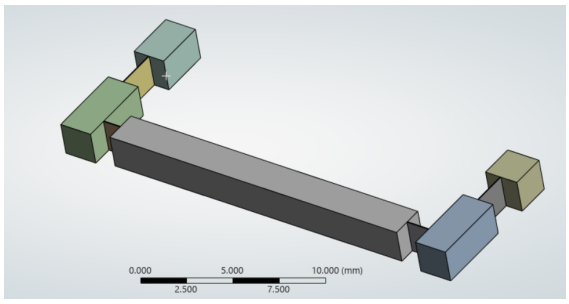
Prototype Static Analysis
The procedure for estimating flexural rigidity and the stiffness of the unmodified flexures is outlined below.

1. The lengths of the flexures in the manufactured prototype were measured using a static top-down picture of the assembly. One physical dimension was measured using screw gauge micrometers. The flexures were measured by comparing the lengths of the flexures in the image with the known physical dimension.
2. Two numerical finite element method (FEM) models were designed, using the same dimensions as the physical prototype. One numerical model is used per side of the prototype, as the two sides do not have exactly equal dimensions, due to manufacturing errors.
3. Both the numerical model and the physical prototype were displaced 1 mm at different locations and reaction forces were obtained.
4. Physical measurements were done using a $2 \ N$ load cell on a linear stage, as shown in figure 3.10. The central actuator was continuously pulling on the plunger during the measurements to have no unwanted compliance in the direction of the actuator displacements. This was achieved by applying a continuous voltage of $12 \ V$.
5. The used measurement setup is shown in figure 3.10. This setup was provided to the author by the PME staff.
6. Comparing the difference in reaction forces found in a numerical model with physical measurements yields a scaling factor for flexural rigidity, as all other parameters were equal. The flexural rigidity of the rigid parts is considered to be significantly higher than that of the flexures. Therefore, the deformation of these parts is considered negligible to the stiffness estimation.
7. The physical stiffness is calculated by averaging two stiffness values. This was done to average out any stiffness non-linearities. The first value is the slope coefficient of a linear line traced through the found data points. The second value is the secant stiffness, calculated by dividing the maximum measured force by the maximum deflection.
8. The fem result has a flexural rigidity of $E \cdot I = E_{steel} \cdot \frac{wt^3}{12}$, or EI_{FEM}. The used value for the estimation is outlined in equation 3.20.
9. The physical prototype had an unknown flexural rigidity, which resulted in a different reaction force, mainly due to the epoxy glue.

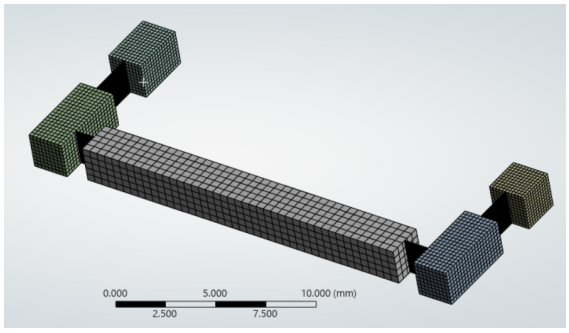
10. Now, $k_{FEM}/k_{real} = EI_{FEM}/EI_{real}$, as L is equal between the FEM and the prototype. Now, EI_{real} can be calculated. This value is then used to calculate the stiffness of each flexure based on the measured flexure lengths in step 1.

Numerical Static Analysis
A screenshot of one of the numerical models is shown in figure 3.8. The numerical models were constructed in Ansys 2024 R2 using, SpaceClaim, Workbench and Mechanical. The used FEM parameters are found below.

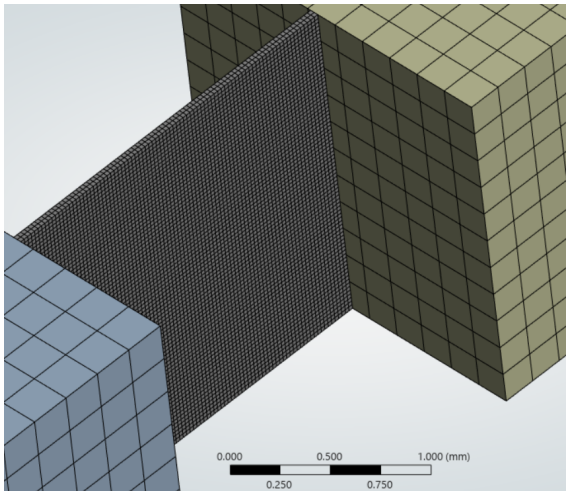
- The model is made up of 9 bodies. Five represent the epoxy printed parts, of which two have a fixed face. Epoxy resin is used as a material.
- The other four bodies represent the flexures. Structural steel is used as material, with an Young's modulus of 200 *GPa*.
- All elements are solid elements.
- The five rigid elements have program controlled mesh size.
- The four flexures were thought to require a smaller mesh size, half the width of the flexure itself. The flexure width is 0.05 mm, therefore the mesh of the flexures is sized at 0.025 mm in the flexures.
- The solver is set to include geometric non-linearities.
- The different bodies are connected through bonded connections without slip.



(a) Chain of flexures and rigid parts modelled in Ansys Mechanical.



(b) Variable mesh size used in the FEM model.



(c) Two elements span the tickness of the flexures.

Figure 3.8: Used FEM model to compare the physical prototype with an idealized result. Here, (a) shows the model geometry, (b) shows the global mesh, (c) shows the mesh of the flexure.

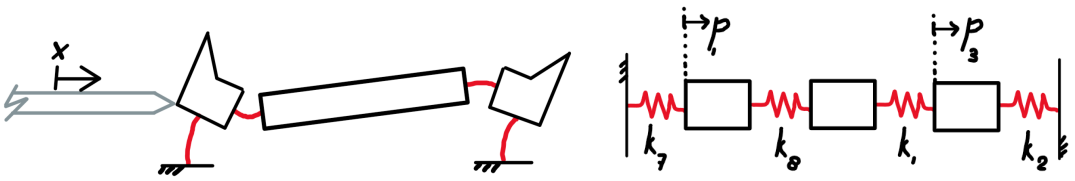
3.2.2. Measuring Stiffness Variations

The method at hand aimed to find how much stiffness change the glueing method of section 3.1.3 realized. Because the glueing method added to the flexural rigidity of the specific flexure, the stiffness estimation outlined in the previous section is not possible, as it relies on equal flexural rigidity for each flexure. Now, an analogous system is designed to estimate the stiffness of the flexures with higher flexural rigidity. The analogy is shown in figure 3.9. The loading of the compliant linkage chain was assumed to behave like four springs connected in series.

The calculated stiffness values of the Original configuration are now used to find the stiffness values of k_2 and k_3 in configuration Stiff V1 and Stiff V2. The other springs have the same stiffness values as calculated in the previous section. This yielded a stiffness expressions for the deflections at measurement point P_3, written in equation 3.22. This expression can be setup for each of the two linkages in the prototype. As k_{P_n} is the measurement of the physical system, and the flexures without stiffness changes were found in the Original configuration, the formula can be solved.

$$k_{P_3} = k_2 + \left(\frac{1}{k_1} + \frac{1}{k_7} + \frac{1}{k_8}\right)^{-1} \tag{3.21}$$

$$= k_2 + \frac{k_1 k_7 k_8}{k_1 k_7 + k_1 k_8 + k_7 k_8} \tag{3.22}$$



(a) Deflection of chain when measuring the wing sides.

(b) Simple mechanical approximation. P_1, P_3 are the measuring points. k_1, k_2, k_7 and k_8 are the flexures in the Wing 1 - Wing 4 system, shown in figure 1.4

Figure 3.9: Schematics used to simplify static deformation analysis in a physical measurement.

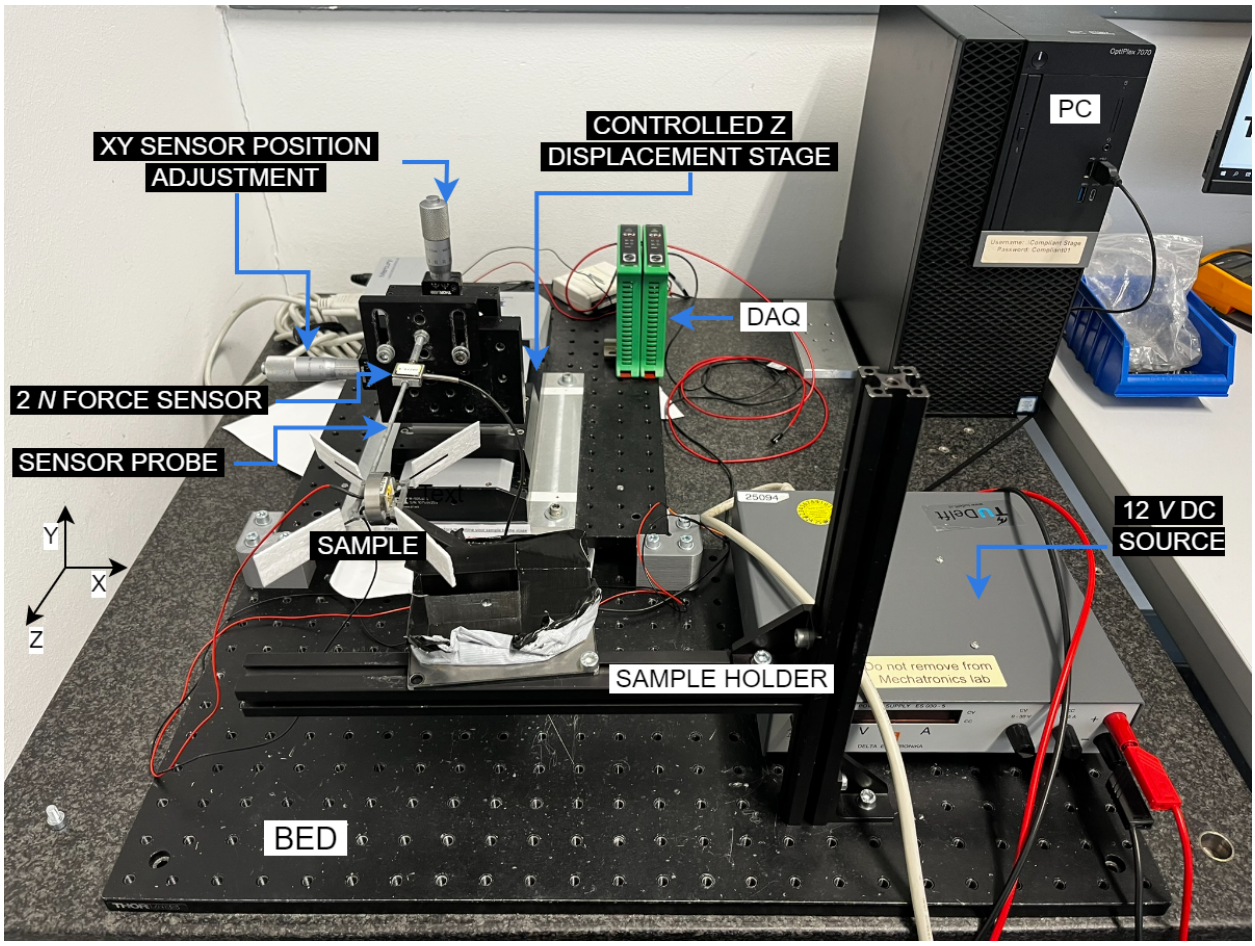


Figure 3.10: The setup used to measure force-displacement graphs. The prototype was rigidly connected to a bed using a sample holder. The controlled Z-displacement stage pushed a sensor probe attached to a 2 *N* force sensor into the prototype at specific locations in the linkages. Reaction forces were measured during the movement between the positions, to create a graph. XY force sensor positions were controlled using micrometer heads, aligning the sensor probe by eye. Force sensor data was processed using the data acquisition (DAQ) unit connected to a PC with LabView. The data processing and force sensor calibration were done by Lab Support Staff of Precision and Microsystems Engineering at TU Delft, as this measurements setup is a stand alone system used for characterization and research of compliant mechanism [53].

3.3. Measuring Dynamic Responses

To identify the response modifications of the system due to variations in stiffness, two distinct measurements, supported by a numerical modal analysis were performed. The first measurement aimed to find the sweeping amplitude response of all wings as a function of frequency, and compared the Original configuration to the Stiff V1 configuration. The second measurement was aimed to find the relative phase response between all wings, as a function of frequency. It compared the Stiff V1 configuration to the Stiff V2 configuration. It was not possible to measure all three configurations using both methods, as the author developed the phase response measurement setup after the stiffness configuration was changed from Original to Stiff V1. Trying to remove the material added to the flexure, as outlined in section 3.1.3, was prone to damaging the prototype. Restarting the manufacturing process was out of scope for this thesis, because of time constraints.

3.3.1. Modal Analysis

A supporting numerical modal analysis gave predictions on what eigenmodes could be present in the dynamics of the resonating mechanism. This model is a linear FEM analysis without damping. As this model was designed before the prototype was fully designed, the model was setup with a simplified geometry compared to the physical prototype. This was deemed satisfactory, as the mass and stiffness distribution was only required to be roughly the same, because the interest lied with finding the eigenmodes, not the response to excitations. The modal analysis extracts the eigenvalues and eigenvectors of the linear mass-

spring system of the model depicted in figure 3.11. In order to reduce computational time, the flexures were modelled as shell elements and the rigid bodies were modelled as solid elements. Contacts were modelled as bonded without slip. Element size is set to be program controlled.

In order to see the effects of rigidly connecting the actuator to ground on the eigenmodes present in the system, this model was duplicated to run the modal analysis twice. The two instances were analysed with different boundary conditions. In the first analysis, the whole drone is free-floating, having six rigid-body modes. This is equivalent to the real Atalanta flying in the air. The second instance has one of the central ring connector blocks rigidly connected to ground.

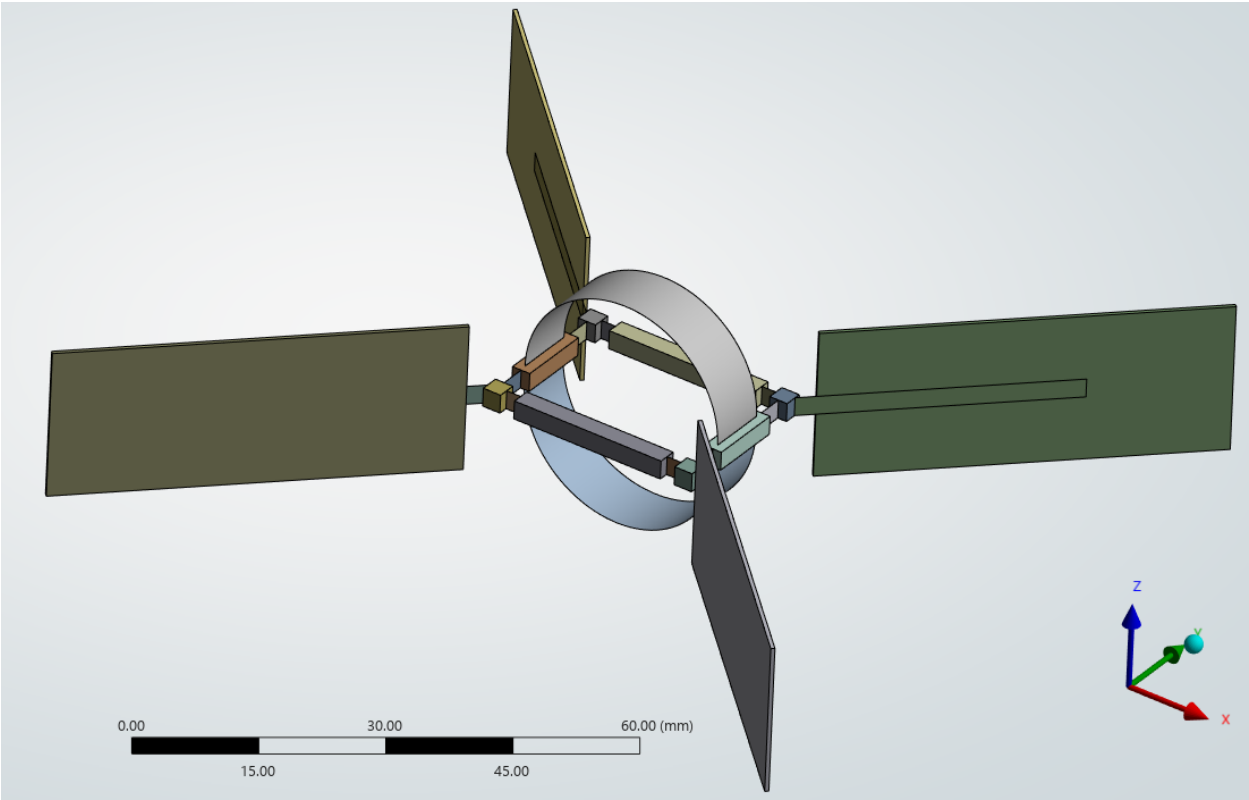


Figure 3.11: Full drone modelled in Ansys Mechanical. The flexures are modelled as shell elements with structural steel material. The wings are modelled as solid elements with EPS foam material. The wing ribs are modelled as shell elements with CFRP material. The rigid parts were modelled as solid elements with epoxy resin material.

3.3.2. Measuring Sweeping Amplitude

To investigate the dynamic behaviour of the prototype, the amplitude response measurement was setup to measure changes in wing sweeping angle under variations in actuator frequency and stiffness. The method consisted of three parts. The drone, with an oscillating linear actuator, driven by an external power source. The camera, taking top-view long exposure photographs of all wings at once. And the post processing logic, converting the images into frequency response functions.

The drone is placed in a black studio box, in order to have full control of the lighting using a stroboscopic pulsing lightsources. The prototype and the external equipment are shown in figure 3.12. The solenoid actuator is attached to an external power source via a transistor circuit. The transistor gate is controlled via an external signal generator using a pulse width modulated (PWM) square wave signal. The transistor circuit was borrowed from PME staff member Bradley But, who designed and soldered the circuit. Frequency modulation precision in the signal generator was limited to 0.1 Hz. Frequency of the actuator was assumed to coincide with the frequency of the signal generator. Frequency of the wings was measured to be the equal to that of the signal generator by using the stroboscope as a tachometer.

The settings and procedures for the amplitude response measurements are outlined below.

- The camera shutter speed was set to be one oscillation period or longer.
- The strobe lighting was set to 1 *kHz* frequency to mimic continuous lighting.

- A black box was built to use as a mini-studio with full darkness. A curtain was fabricated from a trash bag to manipulate the sample between measurements without having to disassemble the box.
- Photos and videos were shot with a Nikon D610 Digital Single-Lens Reflex (DSLR) Camera.
- Different software programs were used to externally control the camera and process raw image files, called DigiCamControl v2.1.7 and RawTherapee v5.12, respectively.
- Prototype actuator frequency was controlled using a Siglent SDG1032X signal generator connected to a Rigol DP2031 programmable DC power supply using a transistor circuit. The transistor fed $12\ V$ PWM square wave signals with a duty cycle of %50 to the actuator, at frequencies ranging between 10 and 80 Hz. The used square wave signal yielded maximum force during the pull stroke for continuous vibrations without overheating the solenoid actuator.
- The Original configuration was measured at the following frequencies in Hz: 10, 20, 30, 40, 50, 51, 52, 52.7, 53, 53.2, 53.7, 54, 54.2, 54.7, 55, 60.
- The Stiff V1 configuration was measured at the following frequencies in Hz: 10, 20, 30, 40, 47, 47.5, 48, 48.5, 49, 50, 51, 52, 53, 53.7, 54, 55, 60, 70, 80.
- The measurement point location, density and the total number of measurement points are not equal over the frequency range between the two configurations, because the resonant frequency of the two configurations differed. The resonant frequency was assumed to be the frequency with the highest amplitude, which was observed by eye when manually sweeping the frequency at the signal generator. It was hypothesized the most interesting dynamics would occur near the resonant frequency.

In order to process the images, a post processing methodology was developed, which is outlined below.

- The photos were processed using AutoCAD Fusion360 and MATLAB 2023b.
- Fusion 360 was used to measure wing deflection by tracing the outlines of the wings in a photograph in the sketch interface.
- It was found the wings deformed under the inertial and drag loading due to the vibrations. Therefore, three measurements were averaged per wing per photo in order to estimate the total amplitude. These three measurements are an indication of the deflection, and not a statistical sampling size. Taking the average assumes no wing deformation took place.
- Multiple photographs were accidentally undersampled by having a shutter speed shorter than the period of the wing oscillation waveform. This discrepancy is discussed in section 4.4.2, and is found to be of marginal influence when because the waveform can be reconstructed using the methods outlined therein.
- All 420 measurements were manually placed in a data frame which was converted into graphs using MATLAB.
- The processing logic plotted frequency response functions by drawing a cubic smoothing spline through the data points. The cubic smoothing spline is accessed though the `fit()` built-in MATLAB function with the `'smoothingspline'` option. [54]. Spline fitting parameters were controlled by the fitting function itself. The splines were used to provide a visual comparison between frequency response data and improve readability of the datasets compared to scatter plots of raw data. Calculations on amplitude modifications are based on the measured data.
- Parts of the processing logic were refined and debugged using an artificial intelligence (AI) in the form of a large language model (LLM) called ChatGPT by OpenAI.
- In order to find the resonant frequency of the whole system, the sweeping angles of the four wings were averaged, yielding a global average per frequency.

3.3.3. Measuring Phase

The phase response of the prototype to frequency and stiffness variations was measured using the same setup as the amplitude frequency response measurements. However, in this setup the camera took video images while a stroboscopic light source illuminated the prototype at a frequency 0.5 Hz above the driving frequency of the actuator. This created an artificial slow motion effect, without the need of high frames per second imaging systems. The observed frequency of the flapping motion in the video images is now 0.5 Hz

The used measurement parameters are outlined below.

- Camera was set to video mode, which used a rolling shutter. The video settings were set to 30 frames per second at 1920$\times$1080 pixels.
- The rolling shutter, together with the strobe light, created a rolling shutter effect. This effect caused parts of the frame to be obstructed by a black video anomaly, as shown in figure 4.19 in the results.
- To extract time domain information from the videos, MATLAB 2023b was used to create video tracking software.
- An LLM called ChatGPT by Open AI was used to choose appropriate video processing functions from the MATLAB 2023b image processing toolbox.
- The program tracks wing position by looping over all frames in a video file and track the brightest pixel within a search window. The search window was 20 by 20 pixels centered on the brightest pixel of the previous frame.
- The initial locations of the bright spots in the frame were found by manually clicking in the frame.
- The contrast between the bright spots on the wings and the surrounding wing material was increased by colouring the top edge of the wing with black ink marker. Also the floor and support structure were made black using back tape and paper.
- Due to the rolling shutter anomalies, in some frames no bright pixel was found in the search window. The program skipped such frames and the missing data point was filled using the MATLAB `fillmissing()` function with the Piecewise Cubic Hermite Interpolating Polynomial (PCHIP) spline option.
- The found dataset of all positions in time over the length of the video was used to fit a sine wave. For each wing a sine wave was fit. The phase delay between the fitted sine waves was measured to determine the phase behaviour between individual wings.
- Phase information between the wings was compared to the phase behaviour of the eigenmodes found in the numerical modal analysis.
- The measurements were performed on 40, 45, 50, 55 and 60 Hz, in both configurations.

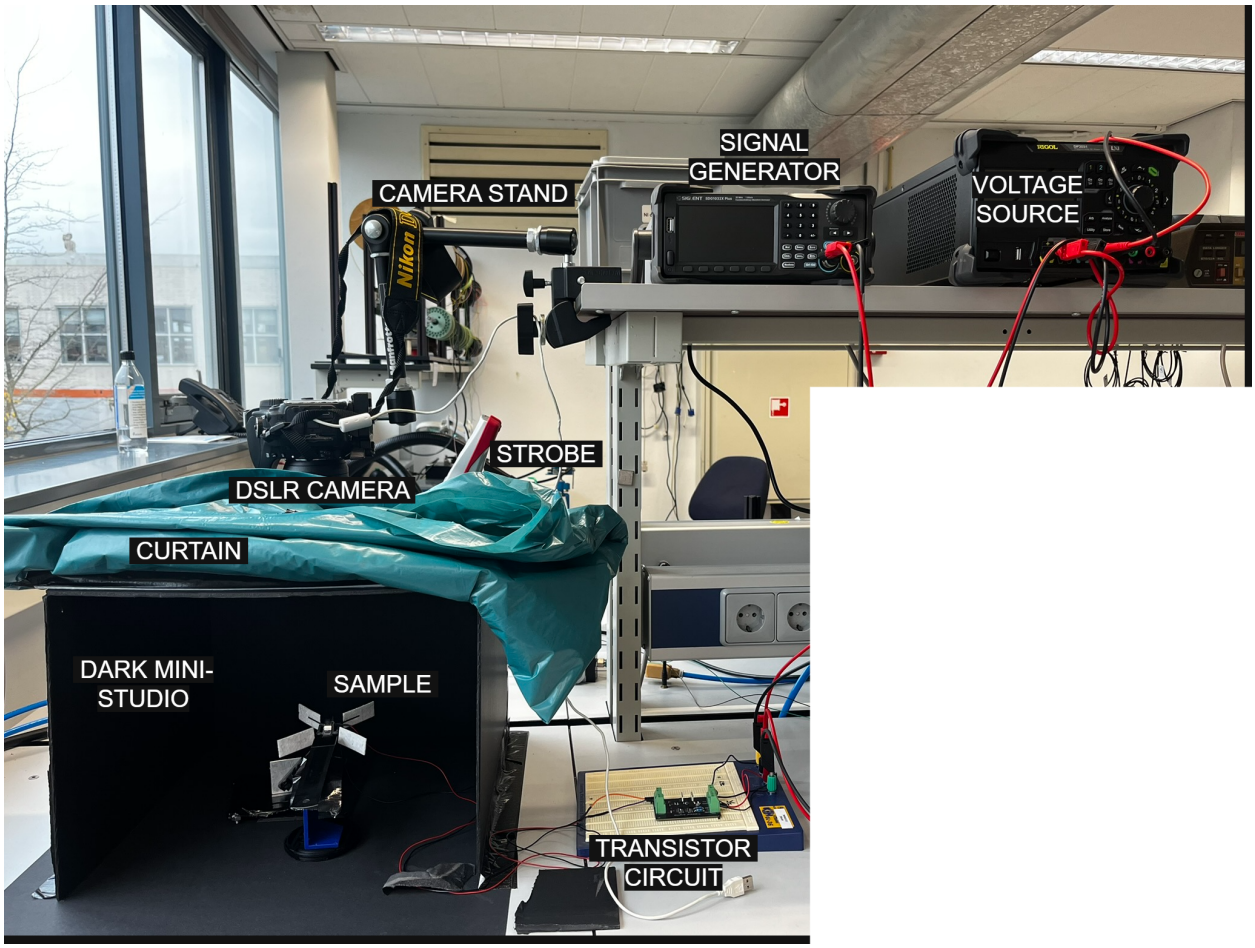


Figure 3.12: The setup used to measure sweeping angle amplitude frequency response and time domain frequency response. The actuator frequency of the prototype was controlled using a Siglent SDG1032X signal generator capable of opening and closing a transistor circuit with a 0-5 V PWM signal. The transistor shorted the circuit between the actuator and a Rigol DP2031 programmable DC power supply supplying 12 V. The actuator displaced the wings of the drone, which were measured by taking photos and videos using a Nikon D610 DSLR Camera. A RheinTacho RT STROBE pocketLED stroboscopic light source was used to control lighting and enable stroboscopic video measurements.

4
Results & Interpretations

This chapter presents and discusses the results from the experiments done on a four wing straight linkage Atalanta FWMAV prototype, under the influence of local stiffness modifications. The chapter contains three sections. The first section is on the manufactured prototype, its real world dimensions, and functioning. The second part is on numerical modal analysis, aimed at identifying the eigenmodes present in the system and the validity of the numerical model. The third section presents and discusses the results of measuring and extrapolating the stiffness values of each of the flexures in each of the configurations and the effects of the precision of indirect stiffness measurements. The fourth section presents the effect of the different stiffness configurations by analysing FRFs of the amplitude and phase of the individual wings.

4.1. Manufactured Prototype

A picture of the resulting manufactured prototype is shown in figure 4.1. The prototype functioned as expected. All wings were displaced by the central actuator, and the actuator was able to visibly displace the wings up to frequencies around $80\ Hz$. The actuator was able to run continuously without significant heating on a $12\ V$ source using a 50% duty cycle square wave. As the actuator is a pull-in solenoid, as described in section 3.1.1, the displacement of the actuator is limited by a maximum stroke. The maximum stroke of the manufactured prototype was found to be $2.08\ mm$. The prototype was found to remain functioning after approximately 57000 cycles.

$$n_{photo} = 35 \tag{4.1}$$
$$n_{video} = 22 \tag{4.2}$$
$$t_{measurement} = 20\ s \tag{4.3}$$
$$f_{avg} = 50\ Hz \tag{4.4}$$
$$n_{cycles} = (35 + 22) \cdot 20 \cdot 50 = 57000\ cycles \tag{4.5}$$

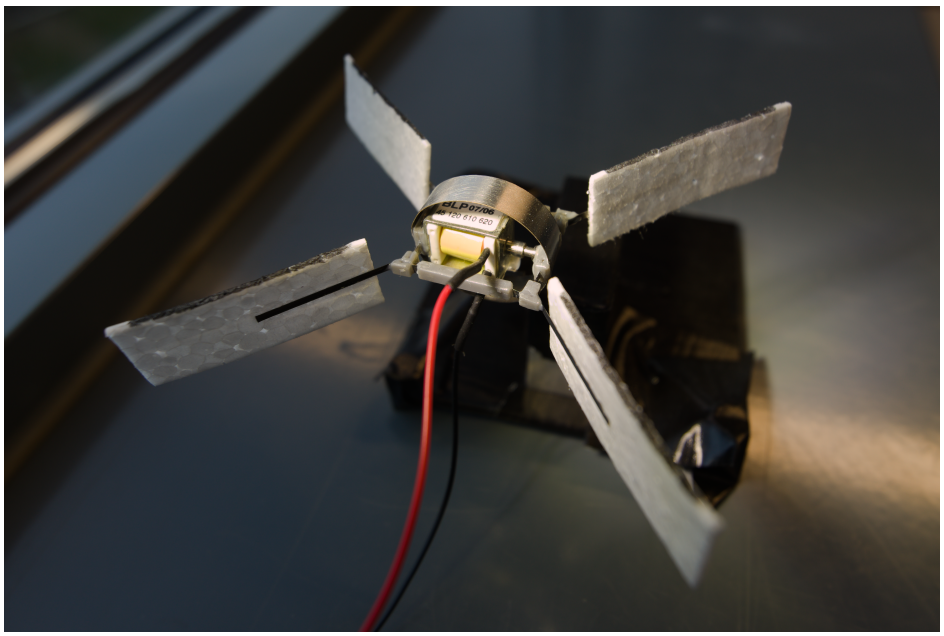


Figure 4.1: Picture of the resulting flapping-wing micro air vehicle prototype.

4.1.1. Dimensional Measurements

The acquired lengths are found in table 4.1. These results were used for the stiffness extrapolation and response analyses in the following sections. The found values were also used to calculate a theoretical transmission of the manufactured mechanism, as described by Bolsman, and derived further in section 2.1. This transmission ratio is not necessarily used for dynamic analysis, rather to compare any found sweeping angle values to expected values. For the calculation, an average of the long flexures and the short flexures are used. When using the model from figures 2.1 and 2.2, L_1 and L_2 will be the distance from the center of the long flexure to the bending plane of the short flexure lengths, and vice versa.

Now, $u = Stroke/2 = 1.04\ mm$, $L_1 = 4.35\ mm$ and $L_2 = 1.87\ mm$. The factor two is used on u, due to the displacement of the actuator appearing on both sides in the model. Plugging in the found values for u, L_1 and L_2, a theoretical angular displacement is found to be approximately $\phi = 13.2° = 0.23$ rad. Here, it is assumed the only displacement the central actuator can cause is in the pulling direction. Any displacements in the negative u direction (increasing the ring diameter) would be from inertial effects. At resonance, these inertial effects might push the wings and the actuator plunger further into the negative u direction, or they might pull the wings further than the plunger can pull them, increasing the total angular displacement. Therefore, the theoretical angular displacement is a static displacement estimate.

Reasons for the error between the nominal dimension and the measured lengths are listed below.

- Flexure slit length was longer than designed due to 3D printing accuracy.
- Flexure slit length tolerance was designed too big, causing the flexures to sink too deep into the slits.
- Flexures were not cut to the right length due to laser accuracy.

Table 4.1: Measured length of each flexure based on measured length of D_{ring} using $0.01\ mm$ accuracy micrometer screw gauge.

Flexure # (Nominal [mm])		Length [mm]
D_{ring}	(28.0)	29.54 ± 0.01
$Stroke\ (2u)$	(3.1)	2.08 ± 0.02
L_1	(2.0)	1.07 ± 0.04
L_2	(3.5)	2.36 ± 0.06
L_3	(3.5)	2.36 ± 0.12
L_4	(2.0)	2.04 ± 0.04
L_5	(2.0)	1.19 ± 0.07
L_6	(3.5)	1.96 ± 0.05
L_7	(3.5)	2.09 ± 0.10
L_8	(2.0)	1.47 ± 0.08

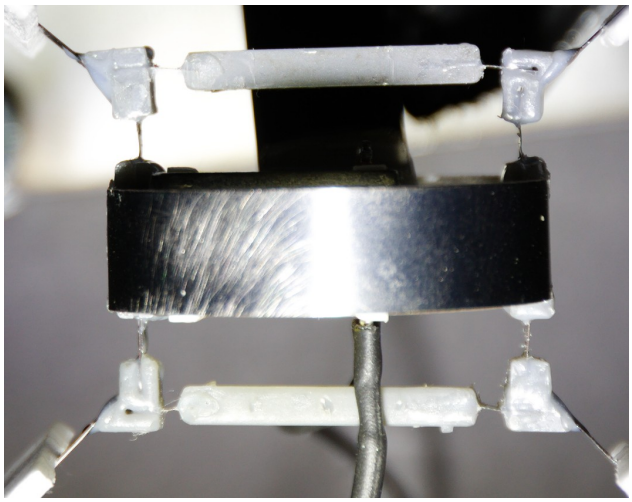


Figure 4.2: Image used for flexure length identification. L_1 is the short flexure in the bottom left corner, near Wing 1. All other flexures are numbered clockwise from L_1, see figure 1.4.

4.2. Modal Analysis

The results from the numerical modal analysis show the prominent eigenmodes present in the system. The free modal analysis shows the mode shapes and eigenfrequencies of a free floating model, with 6 rigid body modes and, therefore, no constraints on the orientation of any of its components. The fixed modal analysis shows the mode shapes and eigenfrequencies of a model fixed on one end of the central ring, while the other and can oscillate in direction of the actuator plunger.

The modal analysis shows two prominent eigenmodes that occur both in the fixed and in the free floating configuration. One eigenmode wherein the angular displacements of the wings in a single flexure linkage chain are in phase, called *Mode 1*. A second eigenmode where the angular displacements are out of phase, called *Mode 2*. Mode 2 is the eigenmode that corresponds with the kinematic motion described in section 2.1. In the free system, both central ring connectors can displace. In the fixed system, one central ring connector is fixed, similar to the physical system. Both configurations are described in 3.3.1. For the free

system Mode 1 and Mode 2 are shown in figure 4.3 at $51.946\ Hz$ and 4.4 at $69.646\ Hz$, respectively. For the fixed system, Mode 1 is split into Mode 1.1 and Mode 1.2 at a similar eigenvalue, shown in figure as 4.5 and 4.6. The corresponding eigenfrequencies are $38.617\ Hz$ and $38.878\ Hz$, respectively. Mode 2 is shown in figure 4.7 at $57.026\ Hz$.

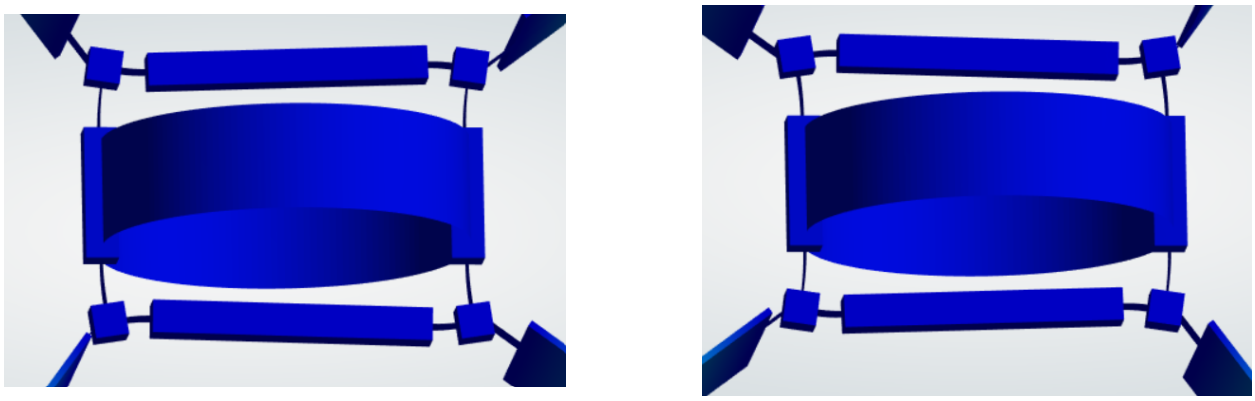


Figure 4.3: Free Mode 1: First structural eigenmode of the free system at eigenfrequency $\mathbf{51.946\ Hz}$. The angular displacement of the wings of a single linkage is in phase. The mode showed bending deformation in the long hinge flexures k_2, k_3, k_6 and k_7 (fig. 1.4). Also, the mode showed no deformation of the central ring flexure. In this eigenmode, the central ring connectors displace in phase with each other and in opposite phase to the wings, when observing the phase in a horizontal direction perpendicular to the central actuator.

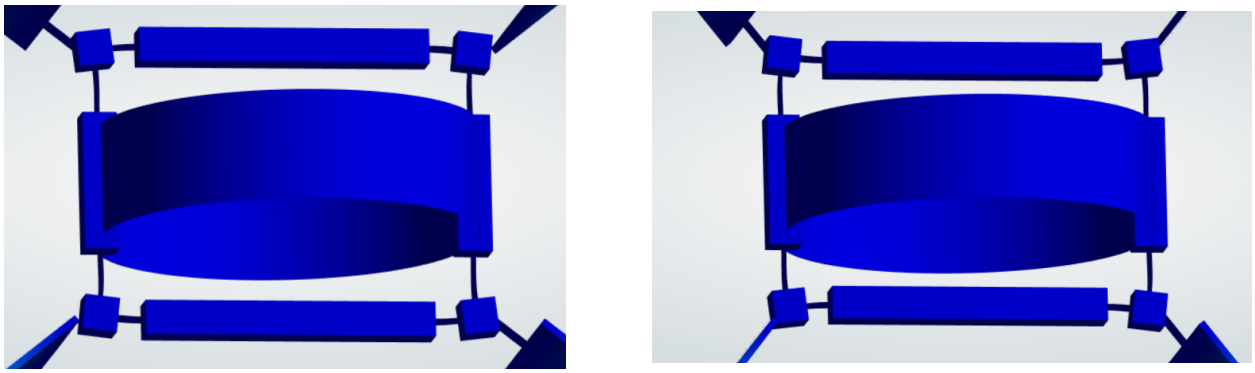


Figure 4.4: Free Mode 2: Second structural eigenmode of the free system at eigenfrequency $\mathbf{69.646\ Hz}$. The angular displacement of the wings of a single linkage is in opposite phase. This is the hovering mode. The mode showed bending deformation in the long hinge flexures k_2, k_3, k_6 and k_7 (fig. 1.4). The eigenmode showed deformation of the central ring flexure.

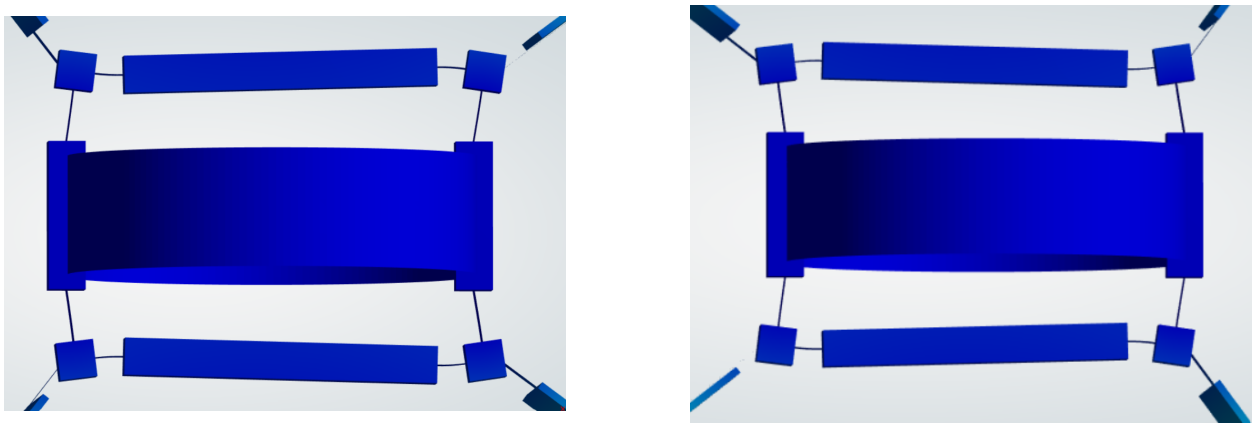


Figure 4.5: Fixed Mode 1.1: First structural eigenmode of the fixed system at eigenfrequency $\mathbf{38.617\ Hz}$. The angular displacement of the wings of a single linkage is in phase. The eigenmode showed no bending in the long hinge flexures k_2, k_3, k_6 and k_7 (fig. 1.4). Instead, the mode showed rotations about the bonded connections points of these flexures to the central ring connectors. The displacement of the central ring connectors was in phase with all of the wing displacements in the direction of actuator displacement. The eigenmode showed no deformation of the central ring flexure.

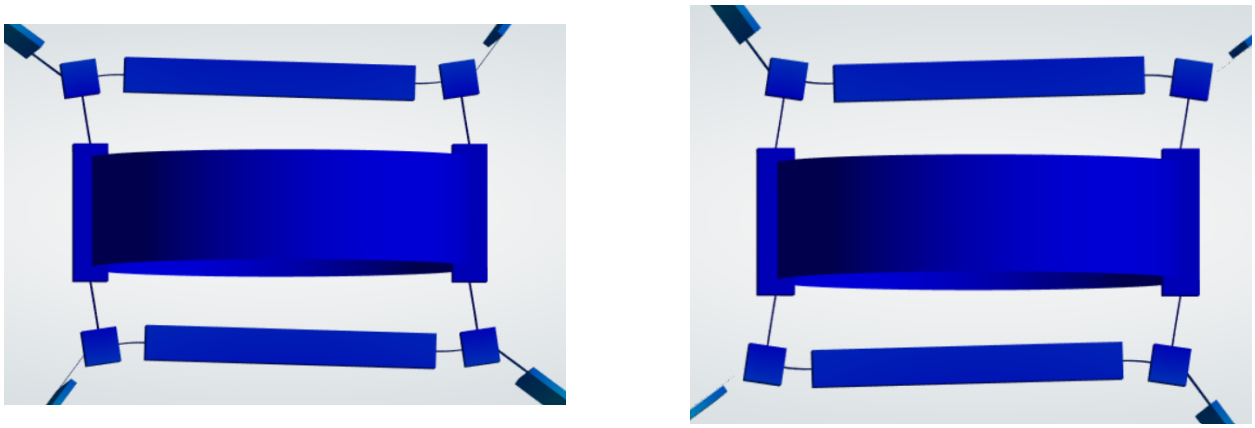


Figure 4.6: Fixed Mode 1.2: Second structural eigenmode of the fixed system at eigenfrequency $\mathbf{38.878\ Hz}$. The angular displacement of all wings is in phase. The eigenmode showed no bending in the long hinge flexures k_2, k_3, k_6 and k_7 (fig. 1.4). Instead, the mode showed rotations about the bonded connections points of these flexures to the central ring connectors. No deformation of the central ring, nor any displacement of the central ring connectors occurred.

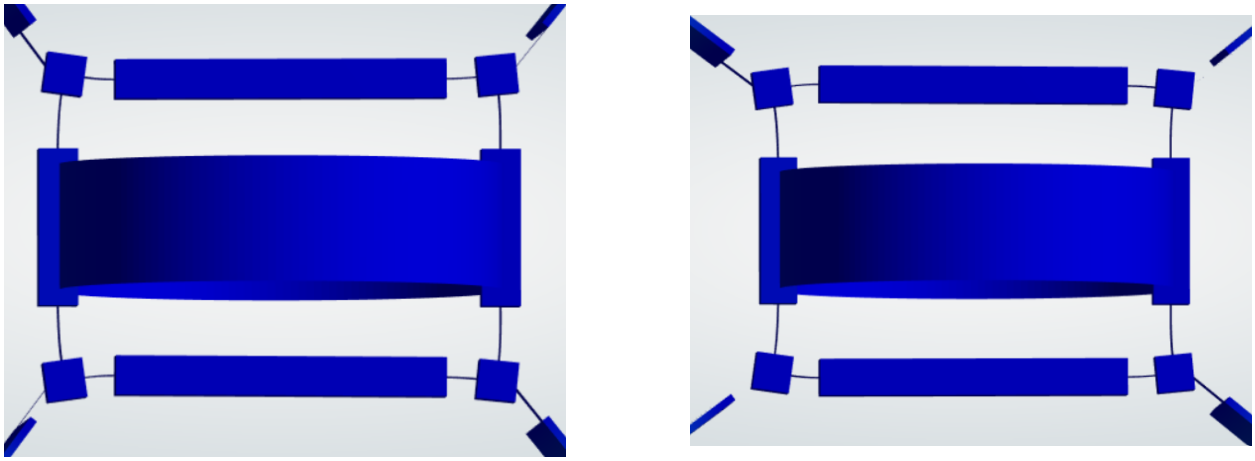


Figure 4.7: Fixed Mode 2: Third structural eigenmode of the fixed system at eigenfrequency $\mathbf{57.026\ Hz}$. The wings move out of phase. This is the hovering eigenmode. The eigenmode showed bending in the long hinge flexures k_2, k_3, k_6 and k_7. Also, the eigenmode showed central ring connector displacements opposite in phase and thus central ring deformations.

4.2.1. Interpretation and Validity of the Numerical Modal Analysis

The results from the modal analysis show eigenfrequencies in the same order of magnitude as those found in literature [29]. In Bolsman's research, a hovering mode eigenfrequency of $29\ Hz$ is found using modal FE analysis on the Straight Linkage Concept. The difference is a factor of approximately $2.4\times$ with the hovering eigenmode in the free system of this thesis, and $1.97\times$ for the hovering mode in the fixed system.

$$f_n = \frac{1}{2\pi}\sqrt{\frac{k_{eq}}{I_{eq}}} \tag{4.6}$$

When comparing the systems by using equation 4.6, the ratio of k_{eq}/I_{eq} is higher in the numerical model analysed in this thesis than the model analysed in Bolsman's research [29]. This implicates higher equivalent stiffness, lower equivalent mass or both, for the numerical system shown in section 3.3.1.

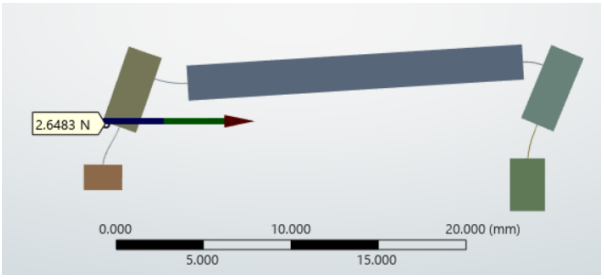
A caveat to this observation is the assumption that other aspects of the two modelling procedures, such as constraints, element type or material use, are the same. The in-phase mode shape, observed in both the free and the fixed system, are not described in literature on the Atalanta. This mode shape appears at lower frequencies than the hovering mode shape. As the wings are part of the displacement pattern in both the in-phase and the hovering mode, it is argued the difference in frequency is mainly caused by the absence of central ring deformations in the in-phase modes. This reduces equivalent stiffness and thus the eigenfrequency. This mode shape can still be present in real-world oscillations, as the in-phase rotation of the cross linkage system is independent from the position of the actuator. That is, if the actuator is in any

position, the in-phase mode can still occur, as no central ring deformation is part of this mode. This is due to the second degree of freedom of the Straight Linkage Concept.

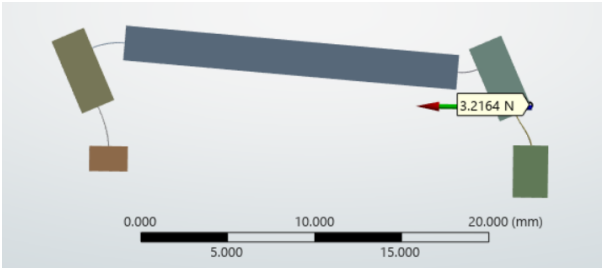
The modal analysis shows some discrepancies which could influence the resulting eigenmodes and eigenfrequencies. First and foremost, the rotating long flexures in the in-phase modes of the fixed system. This is likely caused by the *bonded* connection point being ”Program Controlled”. As all the connections, in both the fixed and the free system, were set up in the exact same way, the program must choose for the bonded connection to have a rotational degree of freedom in the fixed system. No proper solution has been found to alleviate this discrepancy in a moderate time frame. This is deemed reasonable as the thesis is focused on measuring physical results. The main focus of the modal analysis was to find which motion patterns occur in the physical experiments, not necessarily the actual eigenfrequencies.

4.3. Stiffness Measurements

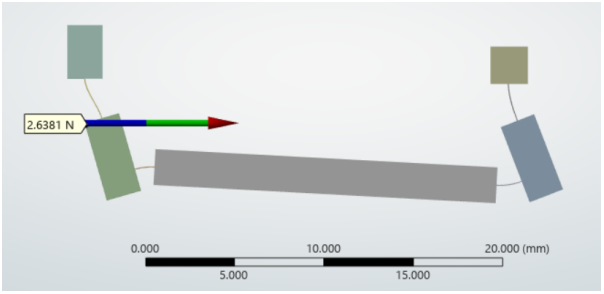
This experiment was designed to measure the stiffness of each flexure in the prototype. A comparison with a numerical model is made to define the found flexural rigidity of the flexures in the Original configuration. The stiffness modifications of V1 and V2 are extrapolated from physical measurements and the found flexural rigidity, as described in section 4.3.2. The full stiffness distribution of the prototype is shown in table 4.2. Here, the measured chain stiffness as well as the extrapolated individual stiffness of each of the flexures are tabulated. Each of the measurement values relates to the orientation of the force sensor compared to the linkage. For example, measurement w_1w_4 is oriented by placing the sensor at Wing 1, measuring the linkage of Wing 1 and Wing 4. The deformation pattern of the physical prototype can be found in figure 4.10. Figure 1.4 shows a schematic overview of the nomenclature. An example force-displacement graph is shown in figure 4.11b. All force-displacement graphs can be found in appendix A.



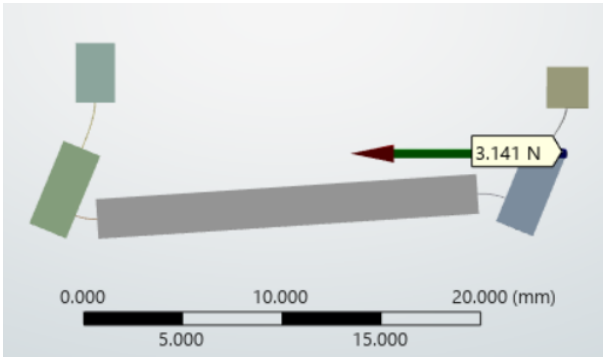
(a) Reaction force at displacement probe near k_3. $\mathbf{F_{w_2w_3} = 2.65\ N}$



(b) Reaction force at displacement probe near k_6. $\mathbf{F_{w_3w_2} = 3.22\ N}$



(c) Reaction force at displacement probe near k_2. $\mathbf{F_{w_1w_4} = 2.64\ N}$



(d) Reaction force at displacement probe near k_7. $\mathbf{F_{w_4w_1} = 3.14\ N}$

Figure 4.8: Static deformation results. The orientation of the linkages match the physical prototype, but rotated 180° compared to figure 1.4.

4.3.1. Evaluating Flexural Rigidity

Figure 4.8 shows the deformation in each of the four probe tip measurements in the numerical analysis. The results are listed together with the physical measurements in table 4.2. Figure 4.9 shows the total deformation of the different flexures under this load. The deformation of the physical prototype resulted in measured reaction forces at the force sensor tip, resulting in stiffness values. These stiffness values can be compared to the reaction forces found in the numerical model. The extrapolated stiffness values are shown in table 4.2.

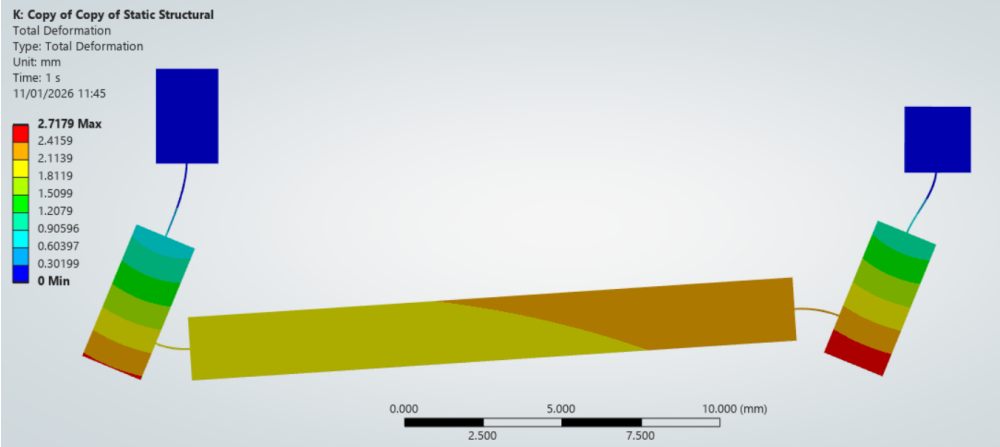


Figure 4.9: Total displacement of the numerical compliant linkage model, displacing the edge on the right near k_7 with 1 mm.

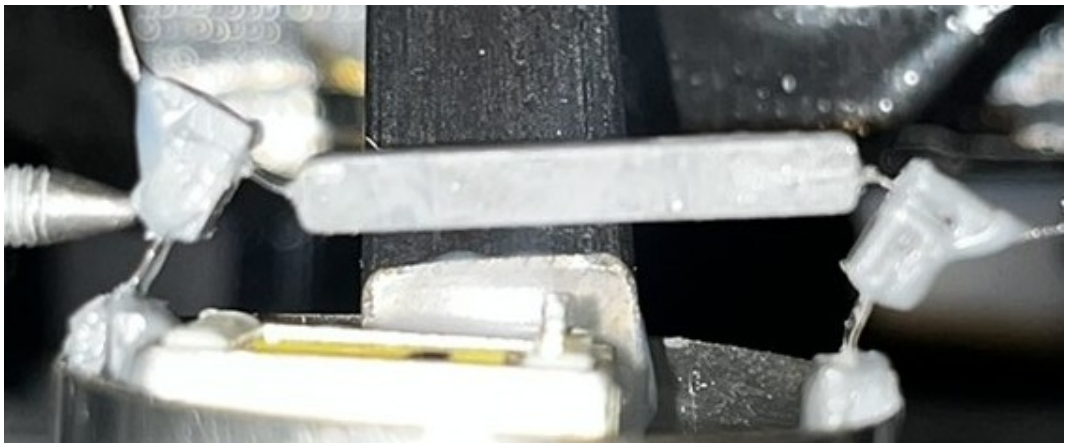


Figure 4.10: Total deformation of the compliant linkage model in the physical prototype, displacing the edge on the left near k_3 with 1 mm, or until the force sensor reaches is maximum load capacity of 2 N.

Table 4.2: Measured and extrapolated stiffness values of each compliant element in the prototype.

Measurement #		Measured Stiffness **Original** $[N/mm]$	**Stiff V1** $[N/mm]$	**Stiff V2** $[N/mm]$
$k_{act_{low}}$		1.06	1.11	-
$k_{act_{high}}$		3.28	2.91	-
$k_{w_1w_4}$		1.00	1.75	-
$k_{w_1w_4}$	FEM	2.64	-	-
$k_{w_4w_1}$		0.87	1.75	-
$k_{w_4w_1}$	FEM	3.14	-	-
$k_{w_2w_3}$		0.88	0.68	1.27
$k_{w_2w_3}$	FEM	2.65	-	-
$k_{w_3w_2}$		0.81	1.04	-
$k_{w_3w_2}$	FEM	3.22	-	-
Flexural Regidity	$[Nmm^2]$			
EI_{FEM}	4.17 (eq. 3.20)			
EI_{real} (n = 6)	1.26± 0.21			
Flexure (Nominal $[mm]$)	**Length** $[mm]$	Extrapolated stiffness **Original** $[Nmm/rad]$	**Stiff V1** $[Nmm/rad]$	**Stiff V2** $[Nmm/rad]$
k_1 (2.0)	1.07 ± 0.04	1.18		
k_2 (3.5)	2.36 ± 0.06	0.54	1.48	
k_3 (3.5)	2.36 ± 0.12	0.54		1.03
k_4 (2.0)	2.04 ± 0.04	0.62		
k_5 (2.0)	1.19 ± 0.07	1.06		
k_6 (3.5)	1.96 ± 0.05	0.64		
k_7 (3.5)	2.09 ± 0.10	0.60		
k_8 (2.0)	1.47 ± 0.08	0.86		

4.3.2. Interpretation and Validity of Stiffness Measurements

The listed stiffness values are of a lower order of magnitude than the values listed in the requirements 2.3. This lower stiffness aids by yielding higher sweeping amplitudes under the same force input. The physical system's flexural rigidity is found be lower than the flexural rigidity of the numerical system, because the connections in the prototype are not rigidly bonded. The physical measurements are influenced by the Young's modulus of the epoxy glue. The Young's-modulus of the epoxy glue is $1.718 \times 10^3\ N/mm^2$ [52]. Compared to $200 \times 10^3\ N/mm^2$ of structural steel, the glue will have a significant effect on stiffness. When dividing the found flexural rigidity with the theoretical area moment of inertia $I = \frac{1}{12}wt^3 = 2.08 \times 10^{-5}\ mm^4$ (eq. 3.20), a resulting average Young's modulus of $E_{real} = 60.7 \times 10^3\ N/mm^2$ is found.

Statistical Analysis

To check how the physical stiffness measurements correspond to the FEM measurements, a statistical analysis is outlined. This analysis gives an indication on the reliability of the physical measurements. The standard deviation of the physically measured stiffness of the linkage chains in the Original configuration, is $\sigma = 0.13\ N/mm$. For the numerical measurements, the standard deviation is $\sigma = 0.31\ N/mm$. Coefficients of variation can be calculated with $CV = \frac{\sigma}{\mu}$. Now, $CV_{real} = 0.15$ and $CV_{FEM} = 0.11$. This indicates the spread in the physical measurements is slightly higher than the spread in the numerical measurements, but of similar order of magnitude.

The coefficient of variation of the extrapolated flexural rigidity $CV_{EI_{real}} = 0.16$. Here, $CV_{EI_{real}}$ captures the spread in the ratio's k_{real}/k_{FEM}, for each measurement. The spread in the ratio itself is only slightly higher than the spread in the measurements. This indicates that the comparison between numerical and physical stiffness measurements can be used to estimate EI_{real}.

The method of extrapolating the stiffness modifications by assuming the system behaves as a chain of serial springs (fig. 3.9), resulted in an measured stiffness increase by a factor of approximately $2.7\times$ for k_2 and $1.9\times$ for k_3 (fig. 1.4). This yielded an absolute change of approximately $\Delta k_2 = 0.94\ Nmm/rad$ for affected flexure k_2 and $\Delta k_3 = 0.49\ Nmm/rad$ for k_3.

Expected Stiffness

More analyses can be done to compare the found stiffness variations with expected results. First of all, no geometric non-linearities are taken into account using this model. Due to rotations at the beam tip, a parallel force component along the length of the beam will be present. This component increases as a function of the deflection, while the component perpendicular to the beam decreases. The parallel component also applies an endpoint moment, as this force is offset by the distance between the loaded flexure and the probe tip. It also applies a tension force. As a beam loaded in tension is significantly stiffer, any force component parallel to the beam will cause much less deflection. In fact, when calculating the tensile stiffness using $k_{tensile} = \frac{AE_{real}}{L}$, it is found that, on average, the tensile stiffness is three orders of magnitude stiffer than the bending force. The compliance of the flexure is dominated by the endpoint moment and force. This should stiffen the system compared to the model used in section .

The stiffness increase is lower than expected, when using the gluing method defined in section 3.1.3. The stiffness of a flexure with a doubled thickness of $2 \cdot t_{original}$, is expected to be $8\times$ higher, due to the area moment of inertia scaling with t^3. The cross-section thickness has increased even more, as the modified flexure is now a composite sandwich structure with glue layers in between. However, the endpoint constraints of the added flexure are different then those of the original flexure glued into the slots of the rigid components. Estimations of the stiffness can be made by assuming the stiffened flexures behaved as sandwich structures. Measurements on the thickness of flexures k_2 and k_3 in the Stiff V2 configuration show thickness increases above a mere doubling. The flexures were measured using digital $0.01\ mm$ accuracy calipers, resulting in $t_{k_2} = 0.48\ mm$ and $t_{k_3} = 0.25\ mm$. It is observed than in the glueing process, a layer of epoxy residue accumulated on the outside of flexure k_2, but not on k_3. Therefore, it is assumed the sandwich structure of k_2 is build up as epoxy - steel - epoxy - steel - epoxy. And that of k_3 is steel - epoxy - steel. Using these measurements and knowing the steel flexures have a thickness of $0.05\ mm$, a epoxy layer thickness can be estimated.

$$\begin{aligned} t_{k_2} - 2t_{steel} &= 3t_{epoxy} \\ t_{epoxy_2} &= 0.127\ mm \\ \text{and } t_{k_3} - 2t_{steel} &= t_{epoxy} \\ t_{epoxy_3} &= 0.150\ mm \end{aligned}$$

When assuming the shear forces within the material cause no slipping between the layers of the sandwich structure, the flexural rigidity of the sandwich geometry can be estimated by taking the sum of the flexural rigidity of each layer, offset by the parallel axis theorem:

$$\sum_{i=1}^{n} E_i \cdot I_i = \sum_{i=1}^{n} E_i \cdot \left(\frac{wt_i^3}{12} + wt_i z_i^2 \right) \text{ with, } z \text{ the distance to the centroid} \tag{4.7}$$

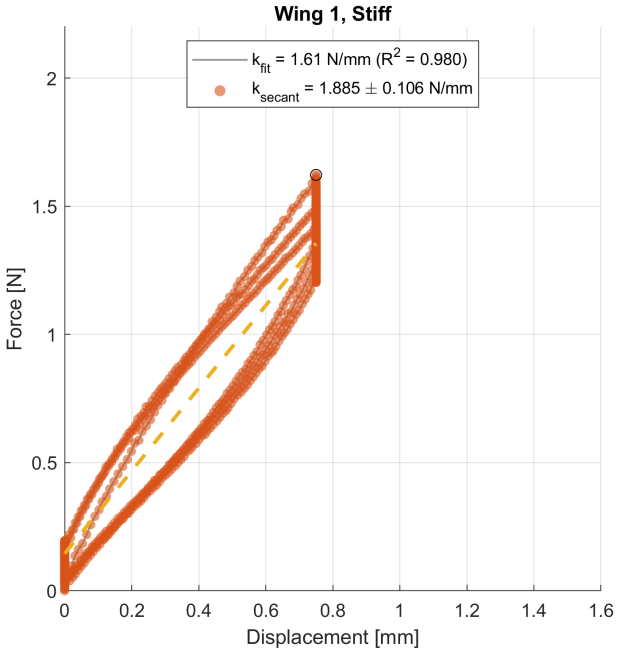
This yields a flexural rigidity of approximately $EI_{k_2} = 349.4\ Nmm^2$ and $EI_{k_3} = 409.3\ Nmm^2$, indicating the sandwich structure is not dominating the overall stiffness of flexures k_2 or k_3. Likely, the endpoint constraints have a much larger effect compliance.

It is recommended to carefully design the endpoint constraints when implementing smart materials into a future prototype. Many smart materials function on cross-section modulation. However, when this modulated cross-section cannot transfer its stiffness to the endpoints of the flexure, hardly any stiffness increase will be realized due to the smart material. When imagining a overhead crane is connected to the walls of a production hall using twigs, the recommendation at hand becomes more apparent.

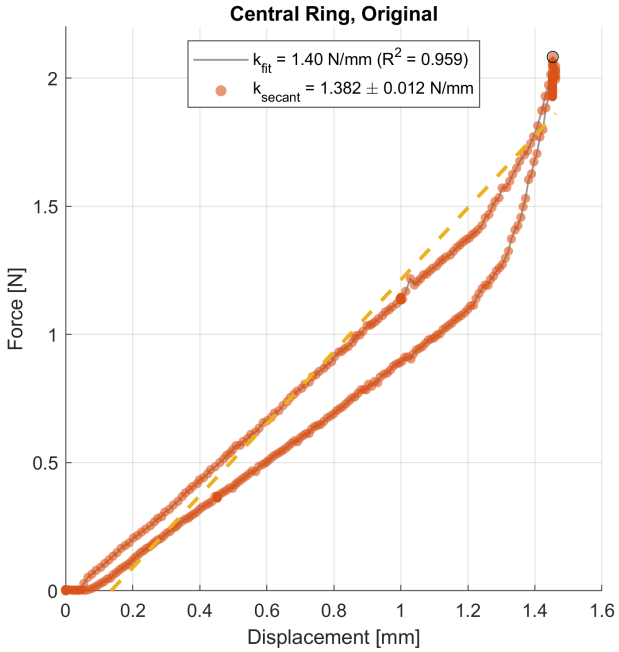
The stiffness of the flexures might be lower than expected due to creep. In figure 4.11a, the measurement data of $w_1 w_4$ in the wing 1 - wing 4 system in configuration Stiff V1 can be seen. During these measurements, the stiffness profile displayed hysteresis and creep, indicating a mechanical aspect of the system is

dissipating stiffness between loaded and unloaded conditions. This is common in thermosetting polymers, such as epoxy, showing viscoelastic behaviour. It can lower stiffness per loading-unloading cycle [33], [55]. Common tests showing the amount of creep are called *relaxation and creep tests*, aimed at showing how much stiffness loss a polymer experiences due to creep [55]. Unintentionally, the measurement of the Wing 1 - Wing 4 linkage in the stiff V2 configuration became a relaxation and creep test. What is interesting is the amount of creep seen in this test is much higher than the force measurements of flexures without stiffness modifications.

This indicates adding stiffness by gluing with epoxy can yield time dependant stiffness behaviour. At slow loading and unloading cycles, the stiffness is different than in fast loading and unloading cycles. Since the vibrations during the frequency response measurements are high, it is expected that the creep relaxation plays no significant role in the effective stiffness at resonance. However, since energy is dissipated during each cycle, it can have an effect on the damping. It is unknown how much effect this has on damping, nor if it is of any significance when comparing it to aerodynamic damping due to drag.



(a) Force-displacement graph of measurement $k_{w_1 w_2}$ in the Stiff V1 configuration. The graphs show substantial hysteresis and creep behaviour.



(b) Force-displacement graph of the central actuator measurement. The stiffness of the ring, combined with all the hinge flexures, was found to be non-linear, sloping upward after a displacement of approximately $1.25\ mm$. The non-linear part of the graph was only measured up to a force near $2\ N$, as this was the limit of the used force sensor. The values depicted in table 4.2 for $k_{act_{low}}$ and $k_{act_{high}}$ are the average slopes of the data, before and after the inflection point at $1.25\ mm$, respectively.

Figure 4.11: (a) Force–displacement graphs of the Wing 1 - Wing 4 linkage measured at Wing 1 in the Stiff V1 configuration. (b) Force-displacement graph of the central ring together with both linkages, in the Original configuration.

4.4. Photography Measurements

4.4.1. Sweeping Angle Frequency Response Functions

The frequency response functions (FRFs) of each wing and the total system, as a result of stiffness changes, are found in this section. The frequency response functions of the Original and Stiff V1 configurations were measured using the method described in section 3.3.2. The stiffness change of flexure k_2 was the only variable that induced changes in the frequency response plots. Figure 4.13e shows the average maximum sweeping angle of all wings. Here, the measurements show a resonance peak at 51 Hz in the Original system, and at 50 Hz in the Stiff V1 system. The stiffening near Wing 1 has lowered the resonant frequency of the full system by a factor of approximately 0.98$\times$, indicating no significant change. When observing the peaks of the individual wings per stiffness configuration, no clear single resonant frequency is seen. Each wing has a different frequency at which the amplitude is highest. Because it is easier to drive an actuator at a constant frequency than using an extra control system for frequency modulated control, it is assumed the results can be compared at the 51 Hz frequency.

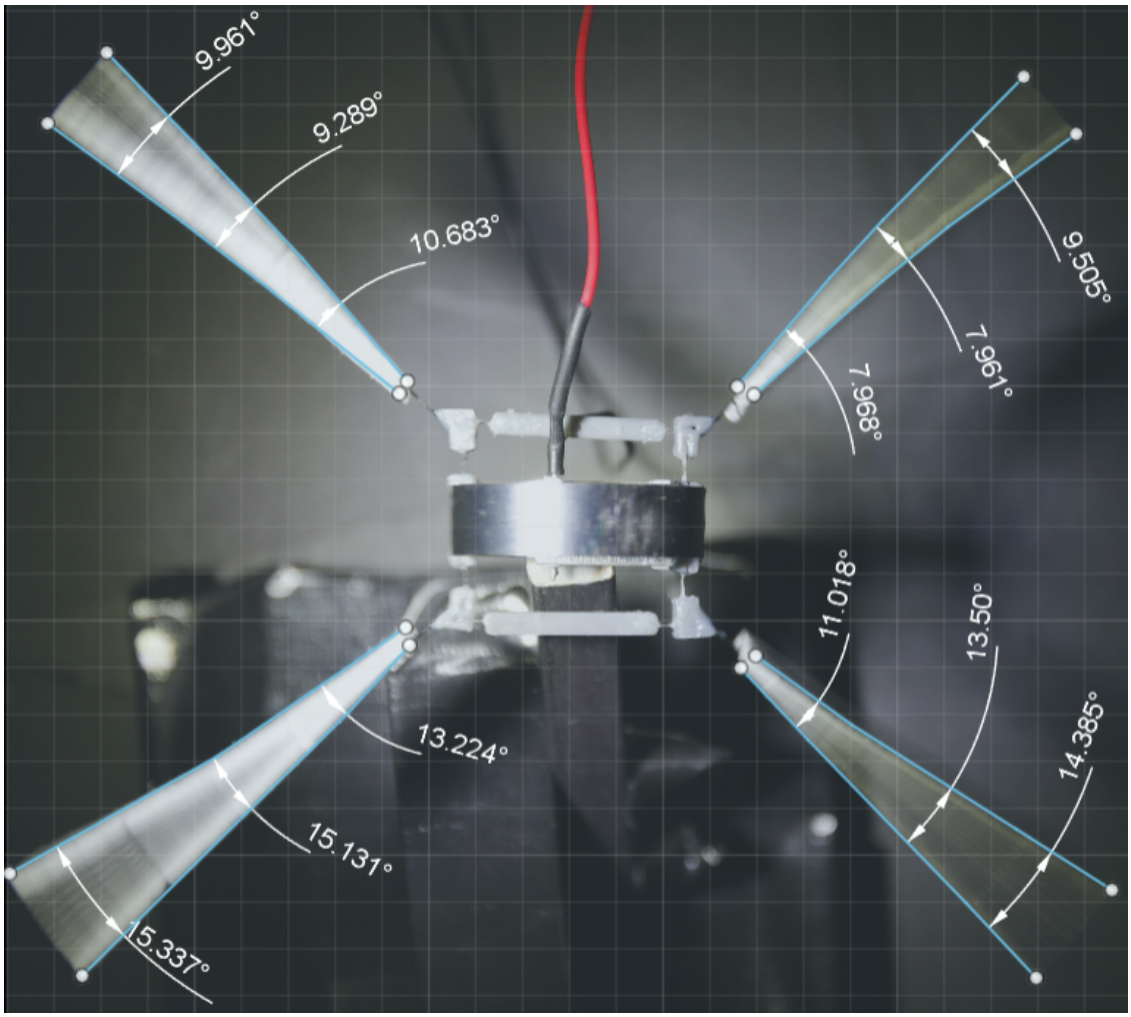
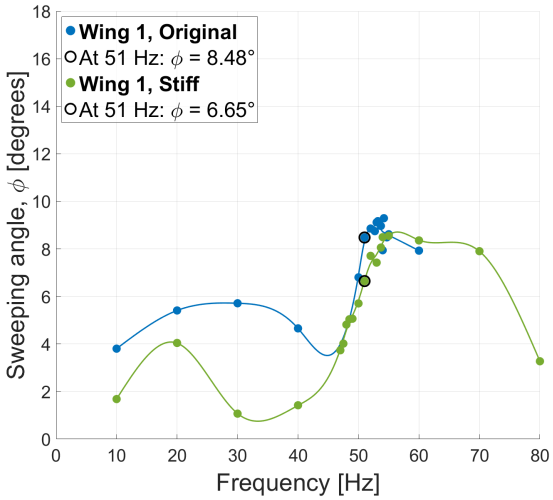
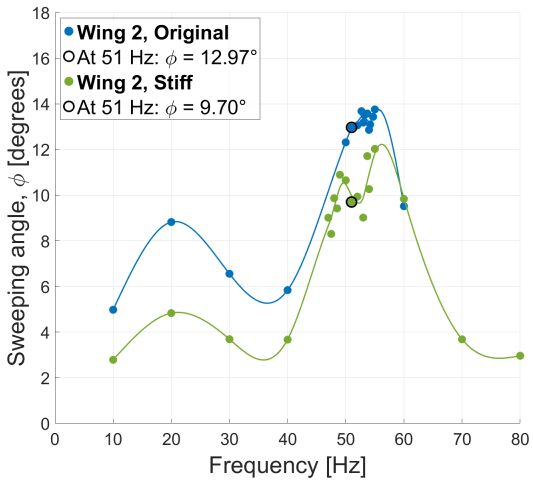


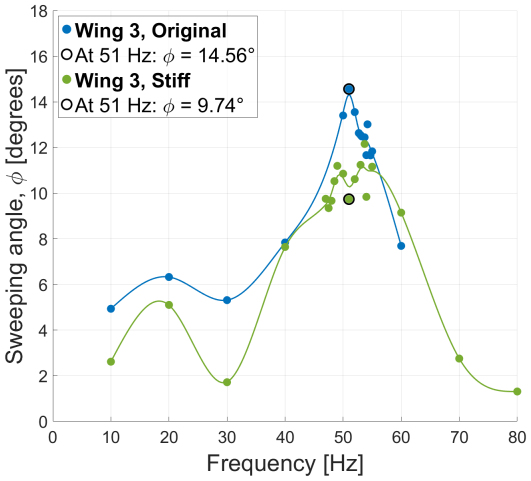
Figure 4.12: Example measurement at 51 Hz in the Original configuration. Each wing amplitude was measured at three instances along the length of the wing.



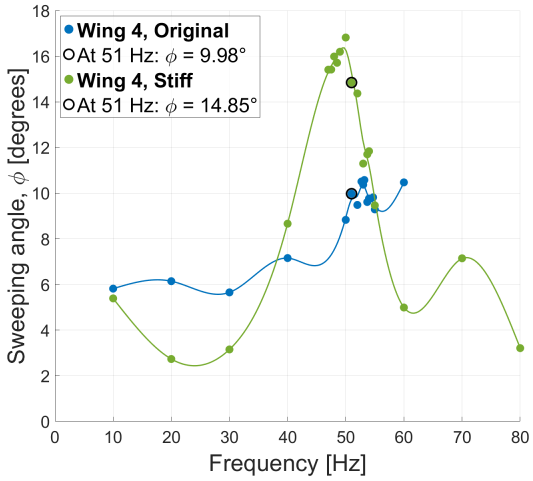
(a) FRF of wing 1. The sweeping amplitude of Wing 1 was lowered by a factor of 0.78$\times$ at 51 Hz



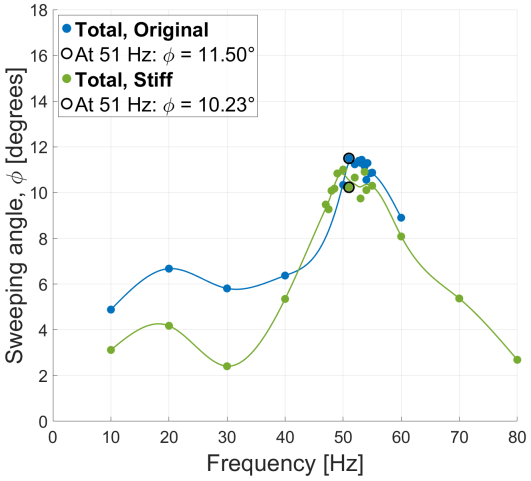
(b) FRF of wing 2. The sweeping amplitude of Wing 2 was lowered by a factor of 0.75$\times$ at 51 Hz



(c) FRF of wing 3. The sweeping amplitude of Wing 3 was lowered by a factor of 0.67$\times$ at 51 Hz

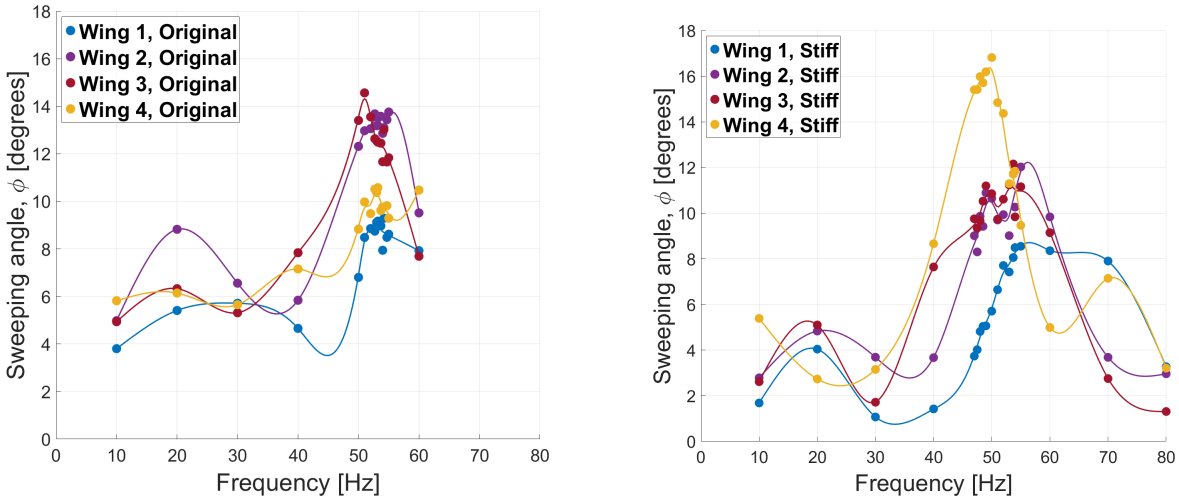


(d) FRF of wing 4. The sweeping amplitude of wing 4 was increased by a factor of 1.49 $\times$ at 51 Hz.



(e) FRF of the total displacement of each wing averaged.

Figure 4.13: Frequency response function of sweeping angle in degrees, before and after stiffness change at k_2. Observed changes of the sweeping amplitude at the resonant frequency of the Original configuration at 51 Hz, showed an increase of ϕ at Wing 4 and a decrease in all other wings. The splines in the figures are used for readability of the scatter data and are not a fit of a mechanical model.



(a) FRF of all wings, Original.

(b) FRF of all wings, Stiff V1.

Figure 4.14: Frequency response function of sweeping angle in degrees, before and after stiffness change at k_2. In the Original configuration the amplitudes of the Wing 1 - Wing 4 linkage system are lower than the amplitudes of the Wing 2 - Wing 3 linkage system. Here, due to manufacturing inaccuracies, the average stiffness of the Wing 1 - Wing 4 system is found to be $(k_1+k_2+k_7+k_8)/4$ =0.80 Nmm/rad. The average stiffness of the Wing 2 - Wing 3 system is $(k_3+k_4+k_5+k_6)/4$ =0.72 Nmm/rad. The splines in the figures are used for readability of the scatter data and are not a fit of a mechanical model.

4.4.2. Interpretation and Validity of Sweeping Angle FRF

The method of measuring the frequency response using photographs is deemed a reasonable approach since the measurements show a clear amplitude peak around $50\ Hz$ for all wings, in all configurations. This corresponds with the resonant frequency of the modal analysis, and is in the same order of magnitude as the resonant frequency found by Bolsman [29]. The results can be used to extrapolate steering capabilities when assuming lift generation is directly proportional to the sweeping amplitude, as outlined in chapter 5.

The measurements used in this chapter were prone to measurement errors due to camera and strobe settings. When reviewing the results, an undersampling discrepancy in the Stiff V1 data was found for frequencies lower than $50\ Hz$. In the Original data this discrepancy was found at measurements at $50,\ 51,\ 52,\ 53,\ 54$ and $55\ Hz$. As described in section 3.3.2, the shutter speed of the camera was set to the period of the oscillations of the actuator to have no aliasing. For example, when the drone operated at $55\ Hz$, the camera shutter speed was put at $1/55\ s$ or slower. However, for all the Stiff V1 measurement, photographs were taken using a shutter speed of $1/50\ s$. For the listed Original measurements, photographs were taken using a shutter speed of $1/60\ s$. As the data is undersampled, the plotted FRF's of figure 4.14 have increased uncertainty.

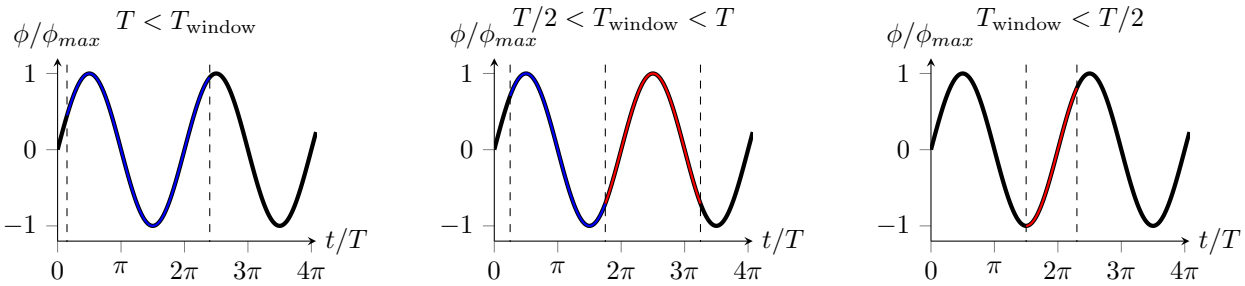
Signal Reconstruction

The signal reconstruction logic is outlined in three steps:

1. Estimate the maximum measurement error of the sweeping amplitude by assuming the center of the measurement window was located at a peak or trough in phase.
2. Calculate the probability of capturing the peak-to-peak amplitude in an undersampled measurement using the ratio between the oscillation period and the shutter speed of the camera. In case, by chance, both peaks were located inside the window, the measurement is not undersampled.
3. Indicate which measurements are most effected by the undersampling.

The amount of uncertainty can be calculated under the assumption that the wings oscillate in a sinusoidal pattern. This assumption is validated by the time domain observations of section 4.5. As there is no control between the phase of the prototype and the measurement instance, it is necessary to have a large enough window to capture the full two-peak amplitude. A measurement window equal or greater than the period of the oscillation will capture both peaks. In an undersampled measurement, the measured amplitude is dependant on the frequency at which the prototype is operating, the window length and the phase at which

the measurement is taken. When the window length is lower than the period, a worst case estimation can be calculated. When the window is wider than half the period, there is a finite probability the captured both peaks. When the window is narrower than half the period, both peaks cannot be captured, but a worst case estimation can still be calculated. In figure 4.15a to 4.15c, the three options are schematically depicted.



(a) Wave measurement window wider than the period, both amplitude peaks lie inside the window, no matter the phase of the window.

(b) Wave measurement windows narrower than the period, but wider than half the period. Blue window: both amplitude peaks lie within the window. Red window: only one amplitude peak lies within the window. The probability of the window capturing both peaks is dependant on the ratio between the window length and period.

(c) Wave measurement window narrower than half the period. The window can never capture both amplitude peaks.

Figure 4.15: Influence of window length on sampling both peaks of a sinewave with random measurement phase. Window length wider than the period (a), wider than half the period (b), or smaller than half the period (c).

For most measurement errors, the measuring window was bigger than half the period. Then, using equation 4.14, the actual sweeping amplitude $2\mathbf{A}$ can be calculated from the measured amplitude $\hat{\mathbf{A}}$. For any other window centering position the equation can be applied, but will yield a lower estimate on the actual amplitude $\mathbf{A}$. Therefore, it is the worst case scenario. A visualization of this process is shown in figure 4.16

From equation 4.14, it can be concluded that the measurement error is lower when T_w approaches $1/f_{act}$. For example, the $51\ Hz$ measurement in the Original configuration was taken with a $1/60\ s$ shutter speed. The measured amplitude for Wing 1 was $8.48°$. There is a chance that this measuring window captured both peaks, as the window spans $51/60 = 85\%$ of the oscillation. In the worst case, the measurement was taken exactly at a peak, and the actual amplitude would be $8.97°$. For the measurement at $55\ Hz$ the measured amplitude of Wing 1 was $8.62°$ with a worst case estimation of $8.77°$. For the measurement at $10\ Hz$ in the Stiff V1 configuration, the measured amplitude of Wing 1 was $5.39°$. Now, with the $1/50\ s$ shutter speed, the worst case estimation is $54.4°$.

$$T_{window} = T_w = \text{Shutter speed } [s]\ , \tag{4.8}$$

$$2\pi f_{act} = \omega_{act}\ [rad/s] \tag{4.9}$$

$$\text{for, } \frac{1}{f_{act}} > T_w > \frac{1}{2f_{act}}\ , \tag{4.10}$$

$$\theta = [\min(\text{window}), \max(\text{window})] = [t_{peak} - \frac{T_w}{2}, t_{peak} + \frac{T_w}{2}]\ , \tag{4.11}$$

$$\phi(t) = \mathbf{A}\sin(\omega_{act}t)\ . \tag{4.12}$$

$$\hat{\mathbf{A}} = \mathbf{A} + \mathbf{A}\left|\cos\left(\omega_{act}\cdot\frac{T_w}{2}\right)\right| \tag{4.13}$$

$$\mathbf{A} = \frac{\hat{\mathbf{A}}}{1+\left|\cos\left(\omega_{act}\frac{T_w}{2}\right)\right|} = \frac{\hat{\mathbf{A}}}{1+\left|\cos\left(2\pi f_{act}\frac{T_w}{2}\right)\right|} \tag{4.14}$$

$$\text{for, } T_w < \frac{1}{2f_{act}}\ , \tag{4.15}$$

$$\mathbf{A} = \frac{\hat{\mathbf{A}}}{1-\left|\cos\left(\omega_{act}\frac{T_w}{2}\right)\right|} \tag{4.16}$$

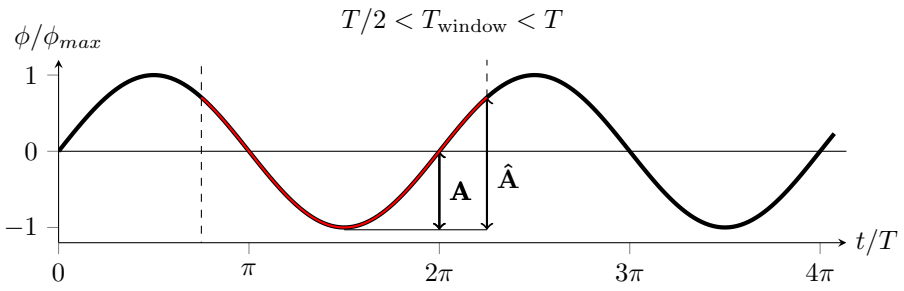


Figure 4.16: $\mathbf{A}$ in relation to $\hat{\mathbf{A}}$ when the window is centered on a peak or trough. This window location is used to estimate the maximum measurement error due to the under sampling.

Probobility

This logic was used to create new frequency response data, with upper bounds on the data points, as shown in figures 4.17 and 4.18. Because of the highly variable size of the bounds, the figures are shown as scatter plots using two distinct domains. The implications of the errors are best shown in the average amplitude of all wings, and the amplitude of Wing 4, because these results influence the interpretations of section 5. Overall, the errors are small and do not influence the qualitative patterns observed in the FRFs. This is due to the fact that the most affected frequencies are the least important to the observed patterns.

The probability that both peaks are captured in the undersampled measurements can be calculated. Since the actuator signal is decoupled from the manually operated camera trigger, it can be assumed the phase of the measurement is randomly distributed over the period of the oscillation. Therefore, the ratio between the window width and the oscillation period is directly related to the probability of the window capturing both peaks. This relationship is only valid for $T_w > T/2$, as smaller windows cannot physically capture both peaks. It can be seen that the undersampling error at $51\ Hz$ is highest, while the probability both peaks are measured is lowest at this frequency. Therefore, it is most probable the resonance frequency is at 51 Hz, with a probability of $P_{tot} = 0.81$. This is calculated by subtracting the probability where the 51 Hz measurement did capture both peaks times the probability the 52 Hz measurement did not capture both peaks from 1, as shown in equation 4.30.

$$t_{window} \sim U(0, T). \tag{4.17}$$

For $T > T_w > T/2$, (4.18)

and $T_w = T \cdot \dfrac{f_{act}}{1/(Shutter\ speed)}$. (4.19)

Then, $c \subseteq \left[t_{peak} - \left(\dfrac{T - T_w}{2} \right), t_{peak} + \left(\dfrac{T - T_w}{2} \right) \right]$. (4.20)

Now, $P_{(both\ peaks)} = 1 - \dfrac{2 \cdot |c|}{T}$ (4.21)

If, $f_{act} = 51\ Hz \ \ \wedge \ \ Shutter\ speed = 1/60$, (4.22)

$T_w = 0.85\ T$, (4.23)

$c \subseteq [t_{peak} - 0.075T, t_{peak} + 0.075T]$ (4.24)

Then $P_{51} = 1 - 0.3 = 0.70$ (4.25)

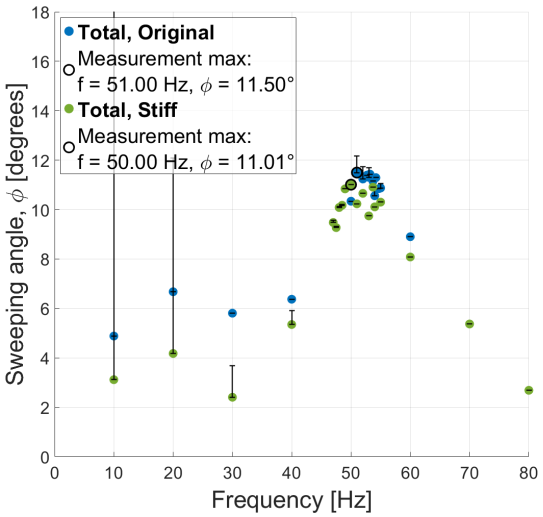
If $f_{act} = 52\ Hz \ \ \wedge \ \ Shutter\ speed = 1/60$, (4.26)

$P_{52} = 0.73$ (4.27)

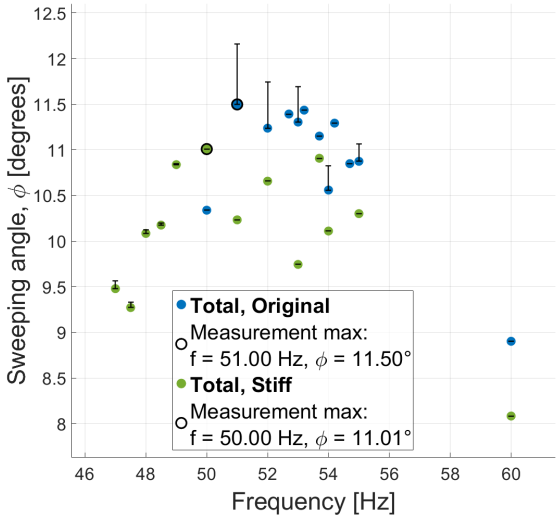
If $f_{act} = 53\ Hz \ \ \wedge \ \ Shutter\ speed = 1/60$, (4.28)

$P_{53} = 0.77$ (4.29)

$P_tot = 1 - (P_{51} \cdot (1 - P_{52})) = 1 - (0.7 \cdot (1 - 0.73) = 0.811$ (4.30)

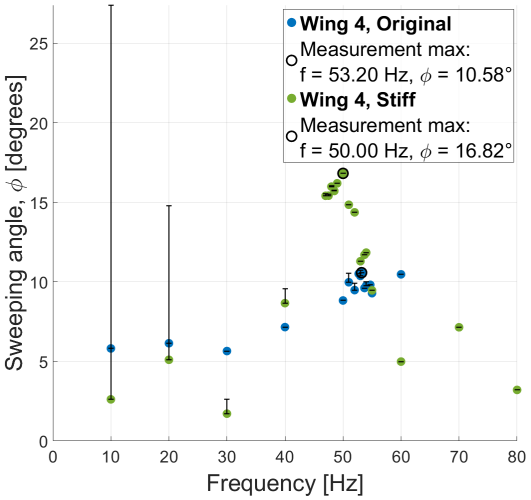


(a) Average sweeping amplitude of all four wings, including error bars. The error on the lowest frequencies are too large to be reasonably depicted alongside the other data points.

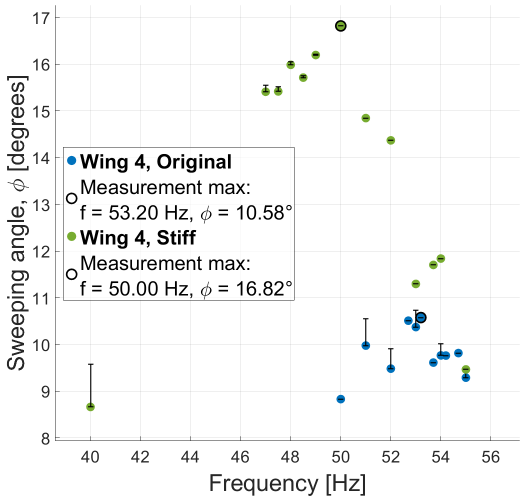


(b) Average wing angle of all four wings, zoomed in on amplitude peak around $51\ Hz$. Because of the induced error, it is not clear which frequency generates the highest amplitude response in the original system.

Figure 4.17: Frequency response scatter plots of average sweeping angle in degrees, before and after stiffness change at k_2. Measurement point error indicate maximum error calculated using equation 4.14 or equation 4.16, not probabilistic error.



(a) Measured sweeping amplitude of Wing 4.



(b) Sweeping amplitude of Wing 4, zoomed in on amplitude peak around $51\ Hz$. The measurement errors do not effect the observed amplitude increase, only the frequency at which the highest amplitude occurs in the original system, which is most probably 51 Hz.

Figure 4.18: Frequency response scatter plots of sweeping angle in degrees, before and after stiffness change at k_2. Measurement point error indicate maximum error calculated using equation 4.14 or equation 4.16, not probabilistic error.

4.5. Video Measurements

Using the stroboscopic video analysis described in section 3.3.3, phase information can be extracted. Configurations Stiff V1 and Stiff V2 were analysed using this method. In figure 4.20a to 4.20d an example of the found time domain data is shown. This data is used to extract phase behaviour of the wing oscillations. Figure 4.19 shows the trajectories of the wing tips when the wings move across the frames of the video. The displacement data was found as two signals, in both the X and Y direction of the frame. No consistent method was found to convert the found XY data to the angular displacement of the wings. Therefore, the phase is extracted from the data measured in the X direction.

A sine wave is fitted through the time domain data with high accuracy. The signals are approximated by a sine wave with at least R^2 =0.95. Some time domain data is distorted by jumps due to the rolling shutter anomalies seen in figure 4.19. The resulting time domain errors can be seen in the results of Wing 2 and Wing 3 in figure 4.20c. The phase information was combined for all wings by comparing the phase of Wing 1 to the phase of the other three wings. This resulted in a frequency response of the phase, affected by changes in stiffness, as shown in figure 4.21.

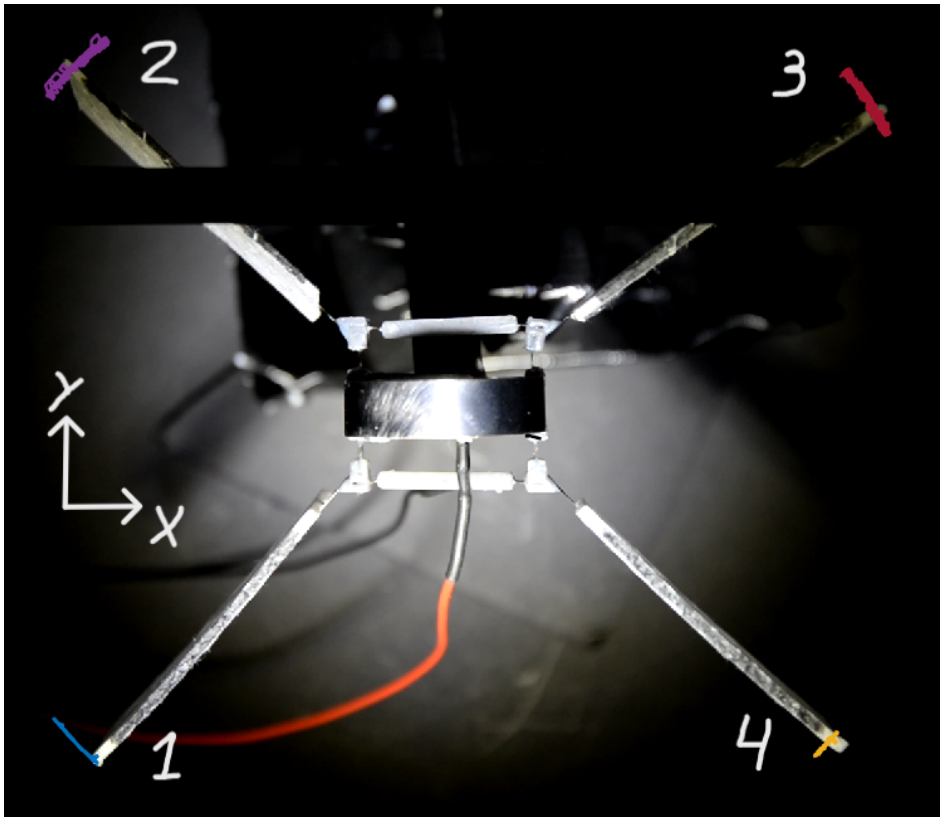
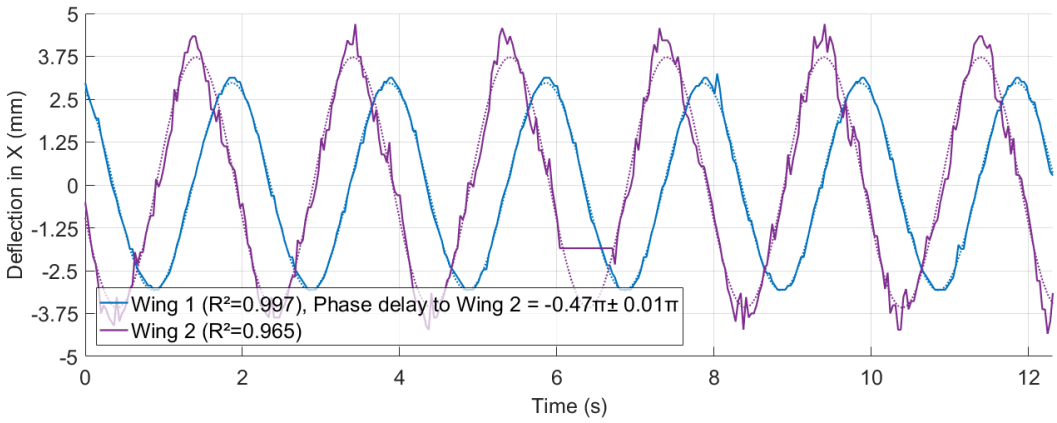
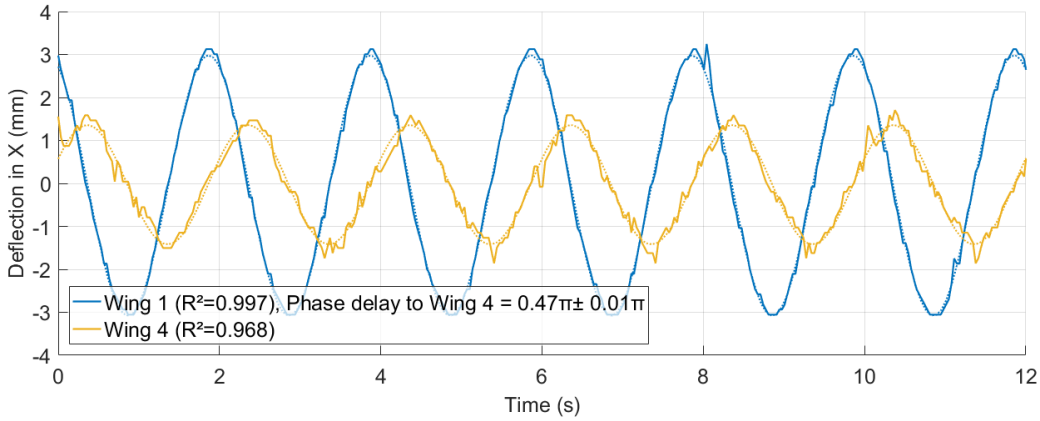


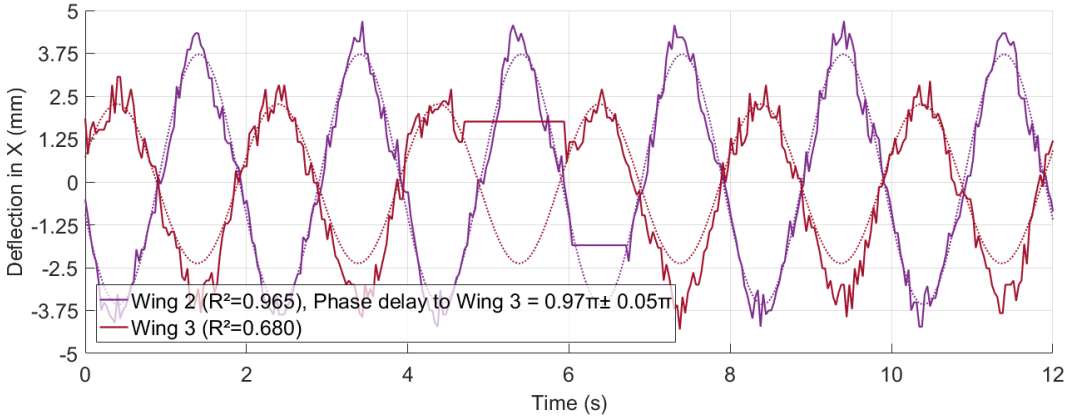
Figure 4.19: Tracked wing tip position traced over the first frame of a video of the Stiff V1 configuration at $55\ Hz$. The black bar at the top of the frame is a rolling shutter anomaly, discussed in section 3.3.2



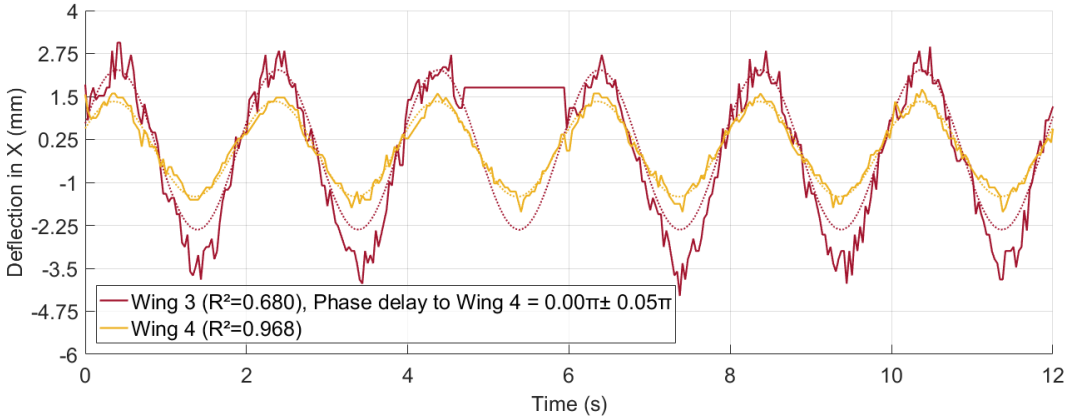
(a) Time domain oscillation of Wing 1 and Wing 2.



(b) Time domain oscillation of Wing 1 and Wing 4.



(c) Time domain oscillation of Wing 2 and Wing 3.



(d) Time domain oscillation of Wing 3 and Wing 4.

Figure 4.20: Time domain oscillations of all four wings in configuration Stiff V1 at $55Hz$

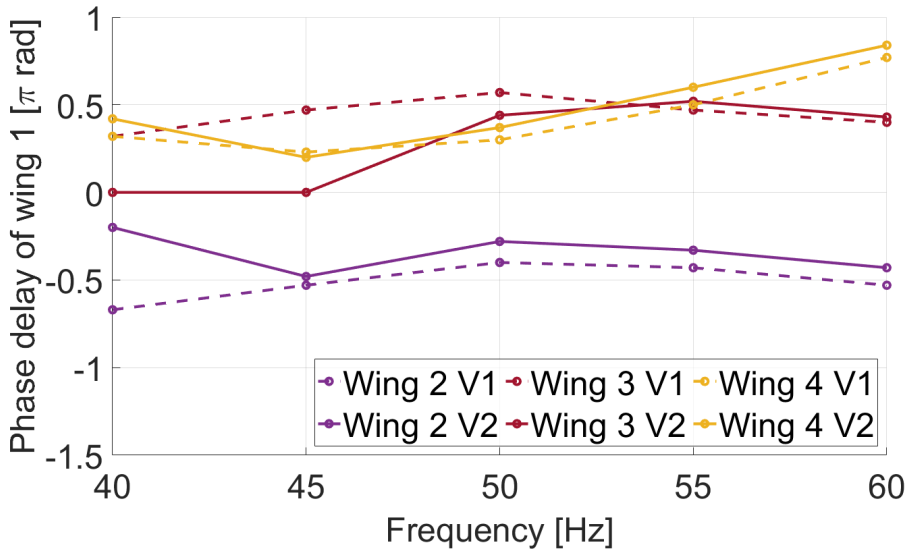


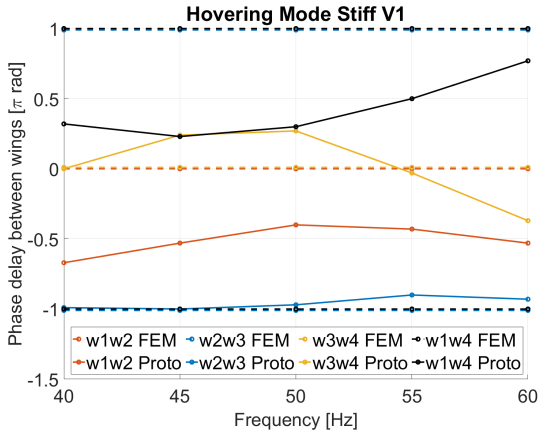
Figure 4.21: Frequency response of the phase delay of Wing 1 with respect to all other wings in factors of π radians. A positive phase delay indicates Wing 1 is behind the respective wing in phase. The phase delay between Wing 1 and Wing 4 was not altered by the stiffness increase. The phase delay between Wing 1 and wing 2 was slightly altered at 40 Hz. The phase delay between Wing 1 and wing 3 was altered below 50 Hz.

4.5.1. Interpretation and Validity Phase FRF

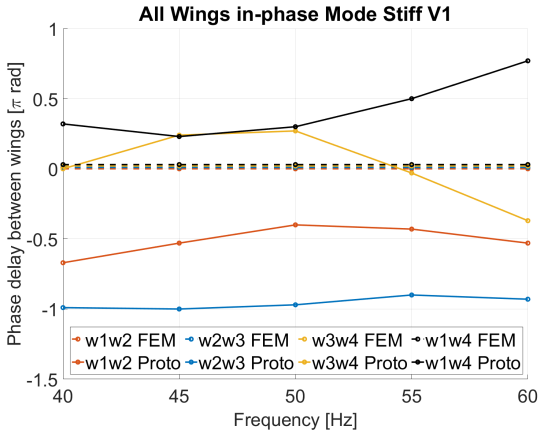
The phase delay observations can be used to measure the effect of the stiffness variations on the participation of the eigenmodes present in the oscillation. This is done by comparing the phase of the eigenmodes found in the modal numerical analysis to the observed phase of the wings in the prototype. When assuming the motion can be described as a superposition of the hovering mode and the in-phase mode, as shown in section 4.2, the observed phase delay can be related to the eigenmodes present. To aid in the comparison, four phase FRF diagrams are shown in figures 4.22 and 4.23.

The phase information between individual wings is calculated from the data in figure 4.21. The phase delay between two specific wings is the measured phase delay of one wing subtracted by the phase delay of the other wing. For example, at 55 Hz, the phase delay between Wing 3 and Wing 4, denoted as w_3w_4, is approximately 0 π rad in both stiffness configurations. At this frequency, the phase delay between Wing 2 and Wing 3, denoted as w_2w_3, is approximately -1 π rad. This is done for all wing combinations.

In the figures, it can be seen that in the Stiff V1 configuration, in the unmodified Wing 2 - Wing 3 linkage, the hovering mode dominates in the vibrations for all measured frequencies (fig. 4.22a). For the modified Wing 1 - Wing 4 linkage, in Stiff v1, the vibrations are in a superposition between the hovering and the in-phase mode. Both linkages show this behaviour in the Stiff V2 configuration. At lower frequencies, the in-phase mode dominates. At higher frequencies, the hovering mode dominates. However, at higher frequencies in the Stiff V2 configuration, the superimposed in-phase mode vibrations caused the hovering mode to have phase differences between the two linkages. That is, at 60 Hz in figure 4.23a, both linkages (w_1w4 & w_2w_3) appear to vibrate in the hovering mode, while a $\pi/2$ phase difference between the linkages remains.

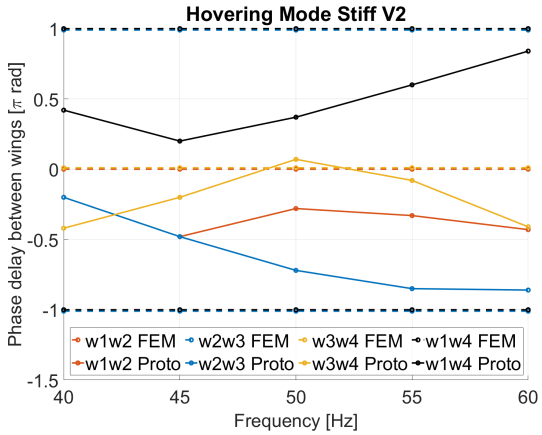


(a) Phase response of Stiff V1 compared to the Hovering Eigenmode. The dotted lines indicate what the phase of the system would be if it were in the hovering mode. For w_2w_3 and w_1w_4, the theoretical phase is shown at $1/-1$, since this is phase equivalent.

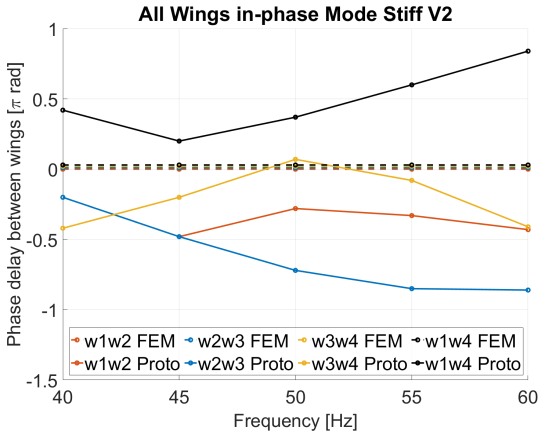


(b) Phase response of Stiff V1 compared to the In-Phase Eigenmode. The dotted lines indicate what the phase of the system would be if it were in the hovering mode.

Figure 4.22: Frequency response function of phase, before stiffness change at k_3 in w_2w_3. Note the used colours do not correspond with the phase delay values of figure 4.21. The Wing 2 - Wing 3 linkage system vibrated in the motion pattern of the hovering mode. The Wing 1 - Wing 4 Linkage system moved in a mode superposition, where the in-phase mode dominated at lower frequencies, and the hovering mode dominated at higher frequencies. The directly actuated wings (3 & 4), moved in and out of the hovering mode, dependant on frequency. The phase of Wing 1 and Wing 2 does not seem to be in either mode.



(a) Phase response of Stiff V2 compared to the Hovering Eigenmode. The dotted lines indicate what the phase of the system would be if it were in the hovering mode. For w_2w_3 and w_1w_4, the theoretical phase is shown at $1/-1$, since this is phase equivalent. At 40 an $45\ Hz$, the phase of w_1w_2 and w_2w_3 are equal, and the data overlaps.



(b) Phase response of Stiff V2 compared to the In-Phase Eigenmode. At 40 an $45\ Hz$, the phase of w_1w_2 and w_2w_3 are equal, and the data overlaps.

Figure 4.23: Frequency response function of phase, after stiffness change at k_3 in w_2w_3. Note the used colours do not correspond with the phase delay values of figure 4.21. In the Stiff V2 configuration, the Wing 2 - Wing 3 linkage system was following the mode superposition pattern of the Wing 1 - Wing 4 linkage system. At low frequencies, the in-phase mode dominated, while at higher frequencies the hovering mode dominated. The phase behaviour of the whole system was most akin to the hovering mode for frequencies above $55\ Hz$. However, the phase of systems w_1w_2 and w_3w_4 are not aligned. If this data is extrapolated to higher frequencies, it seems the two individual linkages vibrate in the hovering mode, but the linkages are out of phase by $\pi/2$. The phase behaviour of the whole system was most akin to the in-phase mode for frequencies below $45\ Hz$.

Validity

The accuracy of the time domain measurements is governed by the tracking of the wing tips and the subsequent sine wave fitting. Overall, no discrepancies have been found to indicate an unreliable interpretation of the results. Some observations influence total understanding of the measurements and system.

First of all, the used algorithm was not able to consistently produce sine wave fits over the entire length of the dataset for each videos. This required data clipping as shown in figures 4.24 and 4.25. In some measurements, the algorithm outlined in 3.3.2 was not able to measure a phase with reasonable accuracy. In this case, the phase delay was measured by observing the difference in time between two peaks. As the slow motion frequency is 0.5 Hz, the phase delay is the time delay times π.

Secondly, the used time domain dataset lacks the position of the actuator with respect to the wings. No method was found to reliably track the actuator position using the bright spot method of 3.3.2 for each dataset. An effort was made to track the position of the central actuator by tracking the bright plastic piece next to the read lead in figure 4.19.

Thirdly, the phase between the wings was found by fitting sine waves, while not all dataset seemed to produce pure sines. Figure 4.26 shows a waveform akin to a triangle wave. The phase information of the triangle waveform does not influence the assumption of sinusoidal signals, as both waveforms are symmetric over their period.

Finally, using the time domain information, a clear influence on the driving voltage can be observed. When the solenoid is driven over the $12\ V$ power limit, much larger amplitudes can be observed. Figure 4.27 shows this effect in the Stiff V2 configuration at $50\ Hz$. Here, it was possible to track the central actuator position, which is shown in figure 4.28. It shows an increase in the overall actuator deflection, indicating the measurements at $12\ V$ were not fully utilizing the designed actuator displacement.

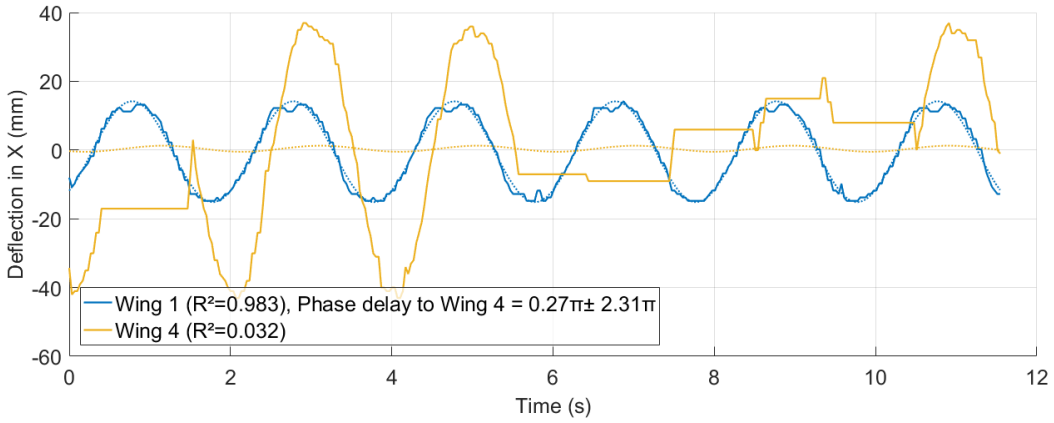


Figure 4.24: Time domain position data of wing 1 and wing 4 in the Stiff V1 configuration at $45\ Hz$. The data is highly corrupted for wing 4 due to the rolling shutter video anomalies.

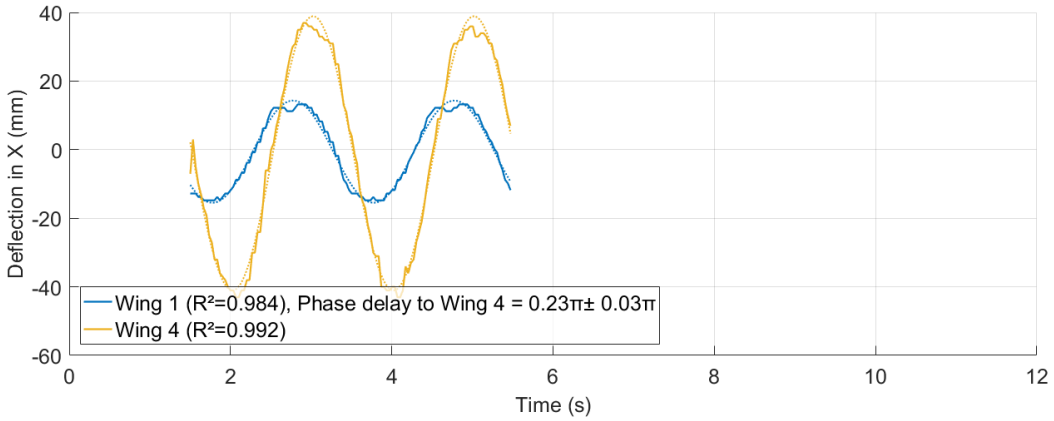


Figure 4.25: Time domain position data of Wing 1 and Wing 4 in the Stiff V1 configuration at $45\ Hz$. The data is windowed to produce a more accurate result.

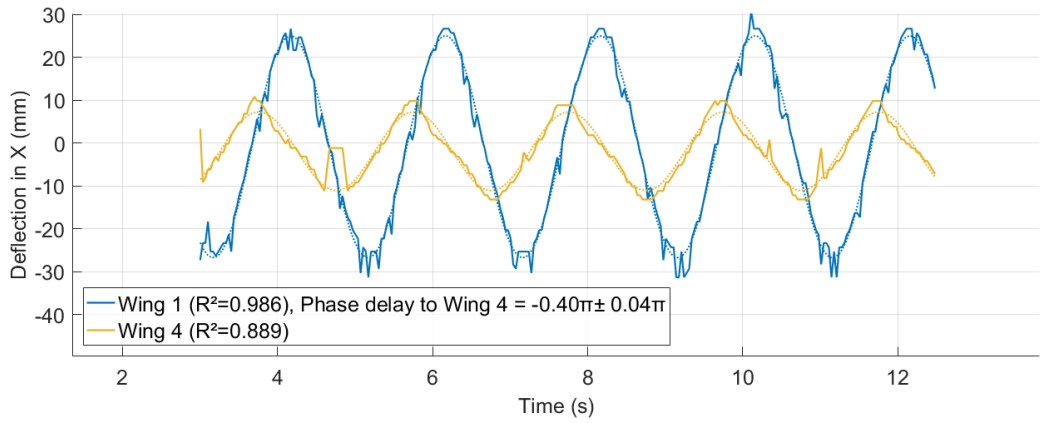


Figure 4.26: Time domain position data of Wing 1 and Wing 4 in the Stiff V2 configuration at $55\ Hz$. Wing 4 displays sawtooth like motion, instead of sinusoidal motion.

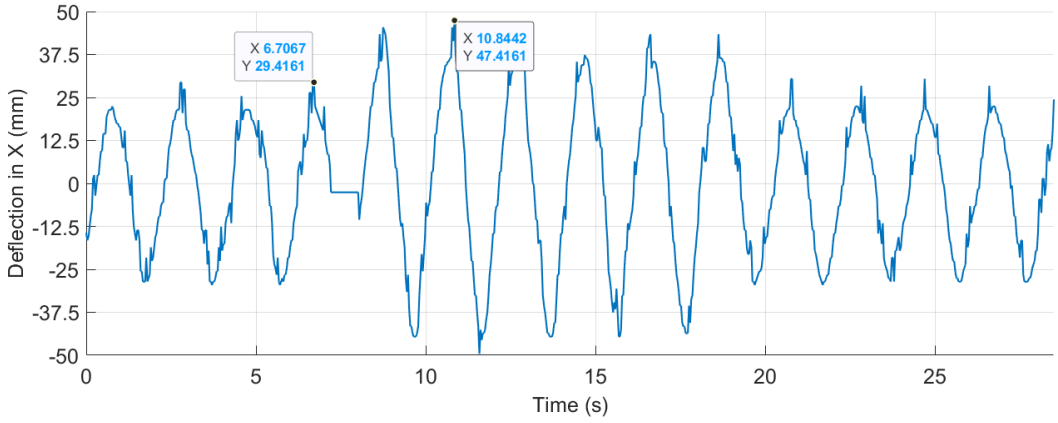


Figure 4.27: Effect of driving the actuator at 18V instead of 12V on the amplitude of Wing 1 in the Stiff V2 configuration at $50\ Hz$. The voltage is increased at approximately $t = 6\ s$ and turned back at $t = 20\ s$. The amplitude is increased by a factor of $1.6\times$.

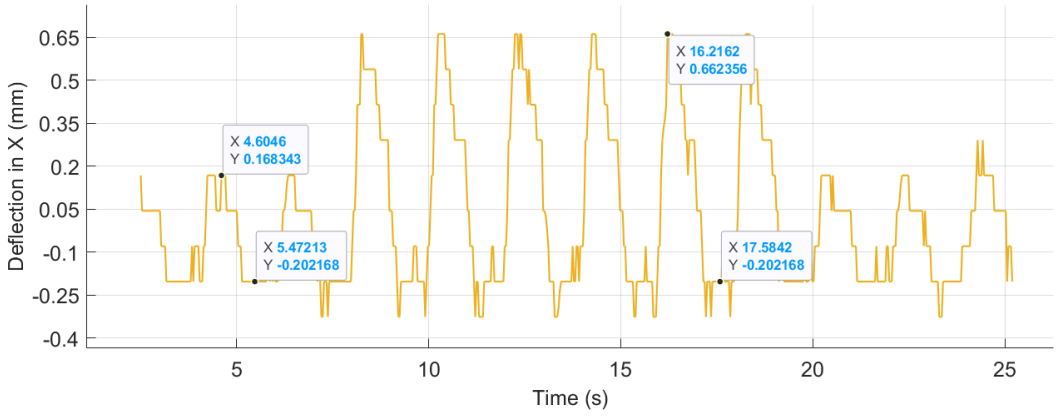


Figure 4.28: Effect of driving the actuator at 18V instead of 12V on the amplitude of the central actuator in the Stiff V2 configuration at $50\ Hz$. The displacement increased from approximately $0.37\ mm$ to $0.86\ mm$, or a factor of $2.3\times$.

5
Implications for the Atalanta FWMAV

This chapter combines the findings of chapter 4 to infer the functioning of the prototype. By looking at the average amplitude of all wings, the eigenfrequency of the whole system, without stiffness modifications, was measured at $51\ Hz$. The stiffness of specific flexures in the two compliant linkages in the prototype was increased from configuration Original to configurations Stiff V1 and Stiff V2. The stiffness was measured to increase by a factor of approximately $2.74\times$, from $0.54\ Nmm/rad$ to $1.48\ Nmm/rad$, using an indirect measurement method. When observing the amplitude response modifications for each wing at $51\ Hz$, an asymmetric amplitude pattern is observed. Wing 1, Wing 2 and Wing 3 have amplitude reductions of approximately $0.78\times$, $0.75\times$, $0.67\times$, respectively. The Wing 4 amplitude increased by approximately $1.49\times$.

The phase observations showed that the local stiffness increase changed the dominant eigenmode in the system. Two motion patterns were observed in the numerical model. One mode shape wherein the sweeping motion of the wings is in phase, and one wherein they are out of phase. Both these mode shapes were observed in physical measurements of the prototype. The stiffness distribution and the excitation frequency caused the dominant mode shape in the response to change. For example, the stiffening at k_3 between the Stiff V1 and the Stiff V2 configuration caused the Wing 2 - Wing 3 linkage system to oscillate in-phase at lower frequencies, and out of phase at higher frequencies. Before the stiffening, the system moved solely in the out of phase mode shape. Therefore, the stiffening changed the modal participation at the measured frequencies.

These findings can be combined to provide qualitative understanding on the steering capabilities of the Straight Linkage Concept, if it were integrated into a fully functioning Atalanta FWMAV. If the Atalanta were to adopt the Straight Linkage Concept, higher sweeping angles need to be achieved in order to acquire lift off. One of the biggest caveats for the extrapolation at hand are the unknown effects of stiffness increase and modal participation at these higher sweeping amplitudes. The currently found amplitudes are not high enough to generate sufficient lift. A fully functioning Atalanta requires peak-to-peak amplitudes of 75° or 120° to generate lift [29], [34]. As the damping in the Atalanta is mainly a result of drag, where $F_d \propto v^2$, and the stiffness of the compliant hinges are non-linear at large rotations, the whole system is non-linear. Therefore, directly extrapolating the found response modification to the higher amplitude regime is not possible. It is recommended further research focusses on what response modifications are obtained under the used stiffness alterations, while at moderately higher amplitudes (40° to 50°) and much higher amplitudes (90° to 100°). This will give an indication on the non-linearity of sweeping angle in relation to hinge stiffness.

5.1. Sensitivity Estimation

In order to analyse the sensitivity of the current system to steering control inputs, two assumptions have to be clarified. Firstly, the lift force is assumed to be directly proportional to the sweeping angle of each wing. In reality, the lift generated by a wing with passive pitching is sensitive to the combination of sweeping and pitching amplitude. Also the phase between these angles, the driving frequency and the equivalent inertia in the system are of influence. Secondly, the sweeping angle of the wings is assumed to be linearly dependent on the stiffness in the locally measured regime. This allows for a linear interpolation of the data, as shown in equation 5.2.

Under these assumptions, the amount of stiffness increase required to generate a sufficient control torque can be interpolated from the found data. From Peters, a lift change of 5% is found to be sufficient for control purposes of a two wing drone [31]. When using equation 5.2 and calculating a linear relation between amplitude and stiffness, the amount of stiffness required to steer the current prototype can be calculated to be $0.63\ Nmm/rad$. Therefore, stiffness is increased by a factor of $1.16\times$, from 0.54 to $0.63\ Nmm/rad$. This inference implies a high sensitivity of the system to structural property modifications.

In this analysis, two problems remain open. Firstly, the observed increase in sweeping angle at Wing 4 is accompanied by sweeping angle reductions at Wing 1, 2 and 3, which has two effects. One possible effect is that it will require less lift force modification to steer when lift is increased on one wing while it is decreased on the opposite wing. The local stiffness modification has a global result on all wings. The other effect is the overall lift force reduction needs to be compensated by the actuator in order to retain a certain elevation while steering, as total lift force is reduced.

The second problem arises when observing the spread in stiffness values due to manufacturing. The found values for the long flexures can be found in table 4.2. Here, in the Original system the calculated difference in stiffness between k_2 and k_6 is, for example, $0.10\ Nmm/rad$. This difference is larger than the interpolated stiffness increase for 5% lift changes, which comes before any measurement uncertainty of the calculated stiffness values. This stresses the necessity of stringent manufacturing tolerances and a more direct method of measuring stiffness. An observation of the sweeping amplitude profile in figure 4.14a of the Original configuration, shows manufacturing inequalities alone could yield a sweeping angle difference adequate for steering.

$$\phi = ak + b = \frac{\Delta\phi}{\Delta k}k\ + b \text{ with } [\phi] = {}^\circ, \text{ for } k \in [0.54, 1.48]\ Nmm/rad \tag{5.1}$$

$$\frac{\Delta\phi}{\Delta k} = a = \frac{14.86 - 9.97}{1.48 - 0.54} \approx 5.20\ {}^\circ/(Nmm/rad), \tag{5.2}$$

$$b = 9.97 - a \cdot 0.54 = 7.16^\circ \tag{5.3}$$

$$k_{required} = \frac{1.05\ \phi_{ori} - b}{a} = \frac{10.47 - 7.16}{5.20} \approx 0.63\ Nmm/rad\ . \tag{5.4}$$

This analysis provides an understanding into the sensitivity of the Straight Linkage Concept, but it is by no means an indication for future design choices. Further research should focus on measuring the effects of smaller stiffness modifications at higher sweeping amplitudes. A new measurement regime modifies the boundary conditions of the test setup closer to applications that are implementable in the Atalanta. The author suggests to first find a stable manufacturing method for an active structural component capable of approximately $1.5 - 2\times$ stiffness modifications over a continuous range. This component would pave the way for much more rigorous dynamic testing, since the analysis would not be limited to sequential passive stiffness configurations or comparing different prototypes.

5.2. Recommendations on Physical Modelling

The observed dynamics of the Straight Linkage Concept can be used to create a new dynamic model of the system. A starting point of the analysis is outlined, based on the observed dynamics. As stated, the stiffness modification at k_3 influenced the phase behaviour of the Wing 2 - Wing 3 system. Inferring what the dynamic behaviour of the system will be at larger sweeping amplitudes requires to test the assumption that the response will have the same modal behaviour at these higher amplitudes.

The observed dynamics display phase responses in modal superposition. A formulation of the sweeping phase response as a superposition of eigenmodes requires the forces in the system to be linear with respect to position, velocity and acceleration [18]. Theoretically, the system at hand is thought to be non-linearly damped through the drag force's dependence on v^2. When oscillating at resonance, a higher sweeping amplitude will result in more damping, which has to be compensated by the actuator.

However, the results can be interpreted as modal superposition because the observation in the modal analysis of section 4.2 align with the observed response in section 4.5.1. The modal analysis shows the in-phase mode occurs at a lower frequency. The same is shown in the prototype phase response (section 4.5.1). The in-phase mode shape is thought to require less energy than the out-of-phase mode shape, as it can occur without central ring deformation. The equivalent stiffness of this eigenmode is lower. This is thought to be the main reason as to why Wing 4 was able to increase amplitude under the stiffness increase.

From 1-DoF damped linear dynamics, one would expect an increase in stiffness to increase the resonant frequency, and therefore decrease the forced response amplitude of the system at resonance, under the same excitation force [17].

$$\phi(\omega) = \frac{F_{act}}{\sqrt{m^2\left(\frac{k}{m} - \omega^2\right)^2 + c^2\omega^2}} \tag{5.5}$$

$$\phi(\omega_r) = \frac{F_{act}}{c\omega_r} = \frac{F_{act}}{c}\sqrt{\frac{m}{k}} \tag{5.6}$$

This is not the case in the prototype system. From the observations of the time domain measurements, the system is thought to be similar to a damped 2-DoF two-mass-three-spring system. Such a system is generally described in physics textbooks on mechanics [18], [56], [57]. This system also has an in-phase and an out-of-phase eigenmode. However, a full description of the forced steady state response of the damped system is out of scope for this thesis. The dynamic system at hand is a suggestion on how a simplified linear model could be made, based on the found observations. A schematic of what the simplified model might look like is shown in figure 5.1. The dampers c_1 and c_4 are located at the masses, but there is no specific damping for relative mass displacements. The ring stiffness is located between the masses, to indicate its component in the out-of-phase eigenmode.

When making qualitative observations of this system, stiffening k_2 until it is essentially rigid will still allow compliance in the w_4 mass. This is thought to be the main reason of the observed shifts in amplitude. The stiffening caused the Wing 1 amplitude to be lowered, and the Wing 4 amplitude to increase. The actuator is still applying the same force, and the same amount of work per frequency. Therefore, it is hypothesized that in the stiffened linkage, at lower frequencies, there is not enough energy in the system to excite the out-of-phase mode, while at higher frequencies there is.

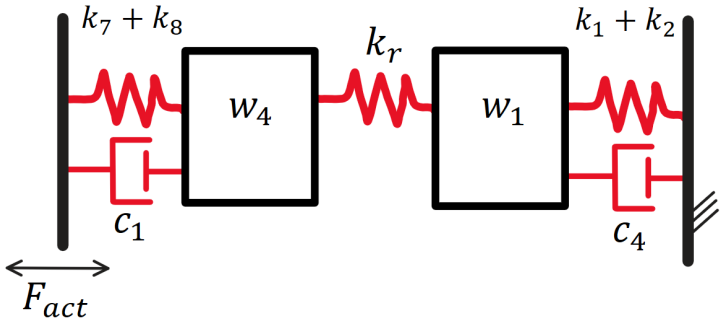


Figure 5.1: Idealized model of the linkage system. The central ring stiffness is placed between the two masses, to indicate the central ring has to be deformed to drive the out of phase mode. The model has two degrees of freedom, with imposed base oscillations.

The damped two-mass-three-spring dynamic system does not have a trivial dynamic expression for the amplitudes at resonance, such as the 1-DoF system of equation 5.6 has. Simplifying the system further, to two masses with one connecting spring, provides qualitative insight at lower abstraction. From theory on coupled oscillators, one would expect an anti-resonance to appear in Wing 4 [57]. This anti-resonance is a dynamic state in which the force of the actuator, acting on the first mass, does not displace this mass. The actuator force is directly opposed to the spring force caused by a displacement of the second mass in the compliant chain. The first mass is standing still, and no work is done by the force. Here, the phase of the actuator and the second mass are opposite.

For the two-mass-three-spring dynamic system of figure 5.1, the anti-resonance is expected to occur as well, together with two resonant peaks. The two eigenfrequencies are expected to occur at two distinct frequencies, corresponding to the in-phase, out-of-phase modes. In the single spring 2-DoF system, the in-phase mode is a rigid body mode, with eigenfrequency $0\ Hz$. The anti-resonant frequency for the two-mass-three-spring system is expected to lie at a higher frequency than the in-phase resonant frequency.

The FRF curves found in section 4.4 show drops in amplitude in all of the wings at intermediate frequencies (20 to $40\ Hz$). It is not known whether this is a response to the anti-resonance dynamics, or the first eigenfrequency being around 10 to $20\ Hz$. Also, the amount of measurement samples is low in the low frequency regime, limiting understanding of the dynamics at low frequencies. In fact, the present drops are more pronounced in the two wings away from the actuator (Wing 1 and Wing 2), which indicate different dynamics are present. Modelling the system as a two-mass-three-spring system is still thought to be an interesting starting point for further dynamic modelling in the Atalanta project.

The main element of the physical prototype that is not described using the linear dynamics are the non-linear damping and geometric non-linearity in the stiffness. This is thought to be an open research topic in the dynamics of this particular system. Especially the extrapolation of the current results to higher sweeping angle dynamics is not possible without this non-linear description.

Furthermore, the used 2-DoF models do not accurately describe the actuator dynamics. In reality the force of the actuator is applied to a third mass, which is connected to the ring and the two linkage mechanisms. There must be a coupling present between the two linkage systems, which is observed to be of influence on the resonant dynamics. The coupling exists, as the Wing 2 - Wing 3 linkage dynamics are influenced by the local stiffness change in the Wing 1 - Wing 4 system (figure 4.14). On top of that, passive pitching in the wings was not included in the physical prototype of this research, but is thought to be required for generating sufficient lift. This adds a degree of freedom to the dynamic system, which further elaborates a physical description of the full Atalanta.

5.3. Recommendations on Measuring the Dynamics of the Atalanta

To summarize, the following recommendations are proposed coming from the found results and inferences:

- A similar methodology can be performed on both the straight and the cross linkage system. The Straight Linkage Concept would have sweeping hinge stiffness modifications and Cross Linkage Concept would have the same passive pitching hinge stiffness modifications. This would generate a direct comparison between the amount of stiffness change and the generated lift modifications.
- Building on the previous point, it is recommended that the prototype performance is not based on angle measurements, but on direct force or torque measurements. This omits the need of precise descriptions of the amount of lift the passive pitching wings generate as a result of the measured wing angles. As the Straight and the Cross Linkage Concept require different angle dynamics to generate steering (Sweeping vs Pitching angle modulation), no comparison between the concepts can be made based on angle measurements without complete aerodynamic descriptions.
- Manufacturing methods need to be improved further in order to make comparisons between prototypes and to properly understand stiffness changes. As the variance of measured stiffness is governed by the variance of length and flexural rigidity combined, researching a robust manufacturing is highly recommended. A proposed solution lies with cutting out stacked sheets [49].
- Passive stiffness modifications need to be replaced with active stiffness modifications capable of continuous instead of discrete alteration. Stiffness modifications by a factor of approximately $1.5 - 2\times$ are deemed generally sufficient. This requires research on manufacturing and implementing active structural components in the FWMAV scale. A known relation between stiffness and voltage is easier to use in experiments then indirectly measuring the stiffness.
- The prototype shows potential and can be made to have larger sweeping angles using smaller hinges. Measuring the dynamics at sweeping angles of moderately higher (40° to 50°) and much higher amplitudes (90° to 100°) allows to describe the non-linear relation between the local stiffening and sweeping angle responses.
- In order to fully understand the resonant dynamics of the mechanism it is necessary to robustly measure the phase of the actuator with respect to the wings. Currently the amount amount of displacement in the actuator is too small compared to the wing displacements, under the noise of the rolling shutter video anomalies. Either by using a high speed camera without anomalies, visually amplifying the actuator displacement in the frame through a linkage, or a second measuring device such as a laser displacement sensor coupled in phase to the camera.
- It is recommended that future research on the resonant dynamics does not rely fully on the method of fixing one side of the actuator, creating an asymmetric displacement. Instead, it is recommended to combine direct torque measurements with measurements wherein the Atalanta is suspended in the air. Also using a symmetric actuator that can pull on both sides with a stationary main body. This allows for a symmetric displacement on both sides, which is hypothesized to generate different dynamics.
- Building on the previous point, the suspended or free-flying Atalanta is also hypothesized to be subject to inertial disturbances due to the in-phase mode. This effect is an open area of research and could limit the applicability of the Straight Linkage Concept.

6 Conclusions

This research explored the use of local stiffness modifications as a control input for the steering of a resonating flapping-wing micro air vehicle (FWMAV) called Atalanta. Specifically, the effect of sweeping hinge stiffness changes on the resonant dynamics of a flapping mechanism was analysed. The mechanism in question was a two degree of freedom, compliant mechanism referred to as the *Straight Linkage Concept*. The mechanism was designed to transfer linear displacements of a central actuator into rotational wing sweeping displacements of four wings. The research aimed to answer whether this Straight Linkage Concept is a viable contender for the actuation and control mechanism of the Atalanta, opposed to the currently used *Cross Linkage Concept*. Both mechanisms are described in section 1.2.2.

By combining a numerical finite element model with the manufacturing and testing of a physical prototype, it was found that locally increasing the sweeping hinge stiffness affected the resonant dynamics of the four wing drone as a whole. By driving the drone at resonance, more wing motion was observed for a given actuator input. The local stiffness increase changed the dynamic response of the sweeping amplitude of individual wings, by modifying their amplitude and phase at resonance. The observed response modifications indicated it is possible to practically realize an asymmetric lift distribution over the four wings using a single stiffness increase, allowing for efficient steering.

6.1. The Behaviour of the Straight Linkage Concept

The research directions of this thesis were guided by the research question:

> *What is the effect of using the Straight Linkage Concept on the steering and control capabilities of the Atalanta, when using structural property modifications as a control input?*

It was found that locally changing the sweeping hinge stiffness affected the resonant dynamics of the four wing drone as a whole, as well as the response of individual wings. In fact, the frequency response functions in section 4.4 indicated that the applied stiffness modification increased the amplitude of one wing, while it decreased the amplitude of the other wings. The dynamic response of amplitude and phase were modified, indicating an asymmetric lift distribution can be realized over the four wings, which is necessary for steering.

While earlier research showed the design of the straight linkage mechanism has closely spaced eigenvalues, indicating a high sensitivity to structural property modifications, it was never attempted to measure the effects of local stiffness modifications in a physical four wing prototype. This research showed how these properties influence the response of the system.

Beforehand, it was hypothesized that a locally higher stiffness in one of the sweeping hinge flexures would effectively limit the movement of the wings connected to this stiffened flexure. In this case, Wing 1 and Wing 4. The response of Wing 1 did lower when observing the stiffened system at the resonant frequency. However, the sweeping angle response was increased in the wing compliantly connected to Wing 1 through the linkage, being Wing 4. This indicates the energy put into the resonating system by the central actuator is transferred away from the stiffened joint, instead of limiting the total displacement.

Measuring the behaviour of the physical prototype under different frequencies and stiffness distributions found the stiffening changed the dominant mode shape in the response. Two prominent eigenmodes were found using a numerical model, which were both observed in the dynamics of the physical prototype. Under symmetric stiffness conditions, an out-of-phase mode shape was observed, wherein the two wings in the Straight Linkage Concept move in opposite directions. The stiffness increase caused the response to include an in-phase mode shape, wherein the two wings move in equal directions. The in-phase mode shape is thought to have less equivalent stiffness, which allows for increased flapping amplitudes in a stiffer configuration. This answers the research question. The capability of the Straight Linkage Concept to shift the modal participation from one mode to the other mode is thought to allow for more elaborate and highly sensitive dynamic response modifications under a local stiffness increase, allowing for high controllability.

The exploration and understanding of the main research question was guided by several sub-questions.

1 *How sensitive are the resonant dynamics of the Straight Linkage Concept to local structural property modifications?*

It was found that the method of gluing extra flexure material to increase stiffness changed the response amplitude of the wings. The response modifications clearly show a sensitivity to the stiffness increase. Through interpolation, a stiffness increase by a factor of $1.16\times$ was found to be able to create an adequate steering torque, were the used in a lift capable prototype. The sensitivity of the Straight Linkage Concept was found to be high enough for implementation in the Atalanta.

Analytically, a 5% lift force modifications have been found to be adequate for roll control of a two wing drone [31]. From the interpolation, it was found that the sensitivity of the mechanism is too high for the accuracy of the used manufacturing method. Measured difference in flexure lengths of $0.3\ mm$ were can change the sweeping angle of this system by more than 5%. This answers the sub-question. The sensitivity of the mechanism at the observed sweeping angles is too high to be practically implemented, when using a manufacturing method based on gluing by hand.

2 *How does the extra degree of freedom of the Straight Linkage Concept affect the dynamics and resonance behaviour of the system?*

It was found the resonance behaviour of the Straight Linkage Concept can be described using the superposition of two vibrational modes. An in-phase mode and an out-of-phase mode. Both of these modes have been predicted using modal analysis in FEM and have been observed using stroboscopic video analysis. From the findings, it is inferred that the extra degree of freedom caused the sharp increase in sweeping amplitude for Wing 4 with respect to Wing 1. If, for example, a stiffness modification fully restricted the rotation of the wing connector at Wing 1, then the other wing in the compliant linkage would still be able to move.

Furthermore, it was found that the phase of the different wings shifted due to changes in stiffness at frequencies below the found resonant frequency. If the lift and control capabilities of the Atalanta are only dependent on cycle averaged lift force modifications, then changes in phase between wings may not be important, as all wings will produce lift, regardless of respective phase. This is only possible if the requirements for controller bandwidth can be slower than the flapping frequency, so that any uncontrolled phase behaviour cancels out during flight manoeuvres. Though, the effect of individual wing phase and total lift production are still to be researched for the Atalanta. Especially when the drone is free floating, the in-phase mode of the linkages could generate unwanted dynamics. A problematic phase behaviour might occur when both linkages and all four wings move in the same direction and inertial effects start to create unwanted vibration the central drone body.

The sub-question is answered by stating that the extra degree of freedom causes the dynamics to be akin to a linear two-mass-three-spring model, in the sense that the dynamics shift between an in-phase and out-of-phase mode. However, due to the geometric and aerodynamic non-linearities in stiffness and drag respectively, the extra degree of freedom causes more intricate dynamics than this model.

3 *In what way does the Straight Linkage Concept differ in steering capabilities compared to the Cross Linkage Concept?*

The comparison between the straight linkage and the Cross Linkage Concept is rooted in the degrees of freedom of the mechanism and the possible locations for local stiffness alterations. No clear indication of different performance has been found through this research, as the methods were solely applied to the Straight Linkage Concept.

However, the observed dynamic behaviour of the prototype indicated that the Straight Linkage Concept has adequate sensitivity to local stiffness modifications in the measured sweeping amplitude regime. The concept is hypothesised to have positive effects on controllability due to its extra degree of freedom, which allows for more elaborate response modifications compared to the Cross Linkage Concept. As the Cross Linkage Concept relies solely on pitching amplitude modulation due to hinge stiffness modifications, and the Straight Linkage Concept can incorporate this too, it is assumed the Straight Linkage Concept is more capable of efficient control.

However, the full non-linear dynamics of the Straight Linkage Concept have not been described analytically or numerically, and it is unknown whether this is possible with reasonable accuracy across flight envelopes. In this sense, the single degree of freedom behaviour of the Cross Linkage Concept would be favourable when a description of the non-linear dynamics of the Atalanta is deemed to be required in future research or prototype design.

The answer to the final sub-question is that the choice between the Straight or the Cross Linkage Concept for control of the Atalanta will have to be based on the possibility of describing the non-linear resonant response. If the description is possible for the Straight Linkage Concept, it is deemed favourable because of the predictive attributes of such a model on the manufacturing and requirements of prototypes. However, if this prediction is not possible, the Straight Linkage Concept provides a much wider array in resonant response modifications. Subsequent prototype iterations could benefits of this. In terms of optimality, finding a locally optimal configuration capable of flight, while relying on manufacturing and testing different prototypes, seems to be more likely if the design space is wider and more combinations of stiffness alterations can be tested.

6.2. Final thoughts on Controlling the Atalanta FWMAV

Controlling the Atalanta by altering the wing flapping dynamics at resonance through local structural modifications is, in the least, not trivial. The experimental focus of this research clearly demonstrated behaviour that was not seen before in the Atalanta project. However, in a paradoxical reasoning, this thesis showed experimental research requires much more control over the variables that are not being studied than the variables that are. In the Atalanta project, a balance has to be found where, on the one hand, experiments should say something about the full four wing system with proper actuators, lift generation, resonance and control. While on the other hand, new sub-components need to be tested individually, because their performance cannot be measured without limiting the scope and understanding the boundary conditions.

Further experimental research, especially on mechanics and control, requires more knowledge on the boundary conditions. Comparing the functioning of the Straight Linkage with the Cross Linkage Concept will require tight control over the manufacturing error and aerodynamic behaviour between the two concepts. In this case, it is deemed unnecessary to fully understand the functioning of the wings or the used materials. If the focus is on picking the best linkage, future research should find a stable manufacturing technique for the mechanism and the wings that allows for a proper comparison.

To the author it seems that most pieces of the control puzzle have been found, but have not been put together due to limits in manufacturing of wings and compliant mechanisms. A final recommendation on the future of the Atalanta is to focus on these elements. However, in the personal experience of the author, these elements might be regarded of less importance to research than testing novel ideas. They are not. Without full control of the variables that are not under study, it is impossible to integrate the amazing findings of at least 26 MSc theses and three (almost four) PhD dissertations.

Bibliography

[1] Falcker Innovations B.V. “Falcker.” (2024), [Online]. Available: https://falcker.com.

[2] Chengdu JOUAV Automation Tech Co.,Ltd. “Agriculture drones | farming drones for crop monitoring - jouav.” (2025), [Online]. Available: https://www.jouav.com/blog/agriculture-drone.html.

[3] Skymagic Live. PTE. Ltd. “Skymagic drone shows.” (2025), [Online]. Available: https://skymagic.show.

[4] Teledyne FLIR LLC. “Flir black hornet 4 prs uav nano drone.” (2025), [Online]. Available: https://www.flir.eu/products/black-hornet-4/?vertical=uas%5C&segment=uis.

[5] Avy B.V. “Applications emergency response.” (2024), [Online]. Available: https://avy.eu/applications-emergency-response.

[6] Zipline International Inc. “Healthcare | zipline drone delivery & logistics.” (2025), [Online]. Available: https://www.flyzipline.com/solutions/healthcare.

[7] K. Telli, O. Kraa, Y. Himeur, S. Atalla, and W. Mansoor, “A comprehensive review of recent research trends on unmanned aerial vehicles (uavs),” *Systems*, vol. 11, p. 48, 2023. DOI: 10.3390/systems11080400.

[8] M. Hassanalian and A. Abdelkefi, “Classifications, applications, and design challenges of drones: A review,” *Progress in Aerospace Sciences*, vol. 91, p. 33, 2017. DOI: 10.1016/j.paerosci.2017.04.003.

[9] M. Perçin, “Aerodynamic mechanisms of flapping flight,” Ph.D. dissertation, Delft University of Technology, 2015.

[10] D. J. Willis, J. Peraire, and K. S. Breuer, “A computational investigation of bio-inspired formation flight and ground effect,” in *25th AIAA Applied Aerodynamics Conference*, Jun 2007. DOI: 10.2514/6.2007-4182.

[11] Hansjörg Wyss Institute for Biologically Inspired Engineering at Harvard University. “Robobees: Autonomous flying microrobots.” (2025), [Online]. Available: https://wyss.harvard.edu/technology/robobees-autonomous-flying-microrobots/.

[12] Micro Air Vehicle Laboratory at Delft University of Technology. “Delfly.” (2025), [Online]. Available: https://www.delfly.nl/.

[13] Soft and Micro Robotics Laboratory at Massachusets Institute of Technology. “Arial robot powered by soft actuators.” (2025), [Online]. Available: https://smrl.mit.edu/research/aerial-robot-powered-by-soft-actuators/.

[14] S. Singh, M. Zuber, M. N. Hamidon, N. Mazlan, A. A. Basri, and K. A. Ahmad, “Classification of actuation mechanism designs with structural block diagrams for flapping-wing drones: A comprehensive review,” *Progress In Aerospace Sciences*, vol. 132 (100833), p. 59, Jun 2022. DOI: 10.1016/j.paerosci.2022.100833.

[15] P. Liu, S. P. Sane, J.-M. Mongeau, J. Zhao, and B. e. a. Cheng, “Flies land upside down on a ceiling using rapid visually mediated rotational maneuvers,” *Science Advances*, vol. 5, p. 10, 2019. DOI: 10.1126/sciadv.aax1877.

[16] C. P. Ellington, “The novel aerodynamics of insect flight: Applications to micro air vehicles,” *The Journal of Experimental Biology*, vol. 202 (23), pp. 3439, 3448, Dec 1999. DOI: 10.1242/jeb.202.23.3439.

[17] P. A. Tipler and G. Mosca, *Physics for Scientists and Engineers, with Modern Physics*, 6th ed. New York: W. H. Freeman and Company, 2008.

[18] M. Géradin and D. Rixen, *Mechanical Vibrations : Theory and Application to Structural Dynamics*, 3rd ed. Newark: John Wiley & Sons, Incorporated, 2015.

[19] X. Xiong, X. Zou, Z. Wang, K. Wang, Z. Li, and W. Yang, “Using electrostatic spring softening effect to enhance sensitivity of mems resonant accelerometers,” *IEEE Sensors Journal*, vol. 21 (5), pp. 5819–5827, Mar 2021. DOI: 10.1109/jsen.2020.3037700.

[20] W. Zhao, R. C. Zheng, X. R. Yin, X. L. Zhao, and K. Nakano, “An electromagnetic energy harvester of large-scale bistable motion by application of stochastic resonance,” *Journal of Vibration and Acoustics-Transactions of the Asme*, vol. 144 (001007), p. 16, Feb 2022. DOI: 10.1115/1.4051265.

[21] E. L. Pradeesh, S. Udhayakumar, M. G. Vasundhara, and G. K. Kalavathi, “A review on piezoelectric energy harvesting,” *Microsystem Technologies*, vol. 28 (8), pp. 1797–1830, Aug 2022. DOI: 10.1007/s00542-022-05334-4.

[22] L. Li, C. Liu, Y. F. Hong, H. C. Wu, X. Y. Tian, and W. M. Zhang, “Design and sensitivity analysis of a micro-resonant accelerometer with adjustable stiffness,” *IEEE Sensors Journal*, vol. 24(5), pp. 5904–5914, Mar 2024. DOI: 10.1109/Jsen.2024.3349540.

[23] M. Ghanbari, G. Rezazadeh, and V. Moloudpour-Tolkani, “A wide-bandwidth mems energy harvester based on a novel voltage-sliding stiffness tunability,” *Applied Mathematical Modelling*, vol. 125, pp. 16–34, Aug 2024. DOI: 10.1016/j.apm.2023.08.034.

[24] J. W. S. Pringle, *Insect Flight*. Oxford University Press, 1976.

[25] A. Pons and T. Beatus, “Distinct forms of resonant optimality within insect indirect flight motors,” *J. R. Soc. Interface*, vol. 19, 2022. DOI: 10.1098/rsif.2022.0080.

[26] S. O. Andersen and T. Weis-Fogh, *Resilin. A Rubberlike Protein in Arthropod Cuticle* (Advances in Insect Physiology), J. W. L. Beament, J. E. Treherne, and V. B. Wigglesworth, Eds. Academic Press, 1964, vol. 2, p. 65. DOI: 10.1016/S0065-2806(08)60071-5.

[27] J. M. Melis, I. Siwanowicz, and M. H. Dickinson, “Machine learning reveals the control mechanics of an insect wing hinge,” *Nature*, vol. 628, pp. 795–803, Apr 2023. DOI: 10.1038/s41586-024-07293-4.

[28] A. Pons, “The self-oscillation paradox in the flight motor of drosophila melanogaster,” *J. R. Soc. Interface*, vol. 20, p. 14, 2023. DOI: 10.1098/rsif.2023.0421.

[29] C. T. Bolsman, “Flapping wing actuation using resonant compliant mechanisms,” Ph.D. dissertation, Delft University of Technology, Oct 2010.

[30] J. F. L. Goosen, H. J. Peters, Q. Wang, P. Tiso, and F. van Keulen, “Resonance based flapping wing micro air vehicle,” in *International Micro Air Vehicle Conference and Flight Competition (IMAV2013)*, ENAC, Sep 2013, pp. 281–288.

[31] H. J. Peters, “A controllability approach for resonant compliant mechanisms,” Ph.D. dissertation, Delft University of Technology, Mar 2016.

[32] N. T. Jafferis, M. A. Graule, and R. J. Wood, “Non-linear resonance modeling and system design improvements for underactuated flapping-wing vehicles,” in *IEEE international conference on robotics and automation*, IEEE, May 2016, pp. 3234–3241. DOI: 10.1109/ICRA.2016.7487493.

[33] M. Ashbey, H. Shercliff, and D. Cebon, *Materials: Engineering, Science, Processing and Design*, 4th ed. Oxford, UK: Elsevier Ltd., 2019.

[34] Q. Wang, “Modeling, design and optimization of flapping wings for efficient hovering flighth,” Ph.D. dissertation, Delft University of Technology, Jun 2017. DOI: 10.4233/uuid:e6fc3865-531f-4ea9-aeff-e2ef923ae36f.

[35] C. T. Bolsman, B. P. Pålsson, J. F. L. Goosen, R. H. Munnig Schmidt, and F. van Keulen, “The use of resonant structures for miniaturizing fmavs,” in *Proceedings of the 3rd US-European Competition and Workshop on Micro Air Vehicle Systems (MAV07) & European Micro Air Vehicle Conference and Flight Competition (EMAV2007)*, 2007, pp. 1–12.

[36] L. Wang and Z. Zhong, “Dynamics of the dragonfly wings raised by blood circulation,” *Acta Mechanica*, vol. 225, no. 4-5, pp. 1471–1485, Apr 2014. DOI: 10.1007/s00707-013-1037-5.

[37] C. Majidi and R. J. Wood, “Tunable elastic stiffness with microconfined magnetorheological domains at low magnetic field,” *Applied Physics Letters*, vol. 97, Sep 2010. DOI: 10.1063/1.3503969.

[38] I. A. Kuder, A. F. Arrieta, W. E. Raither, and P. Ermanni, “Variable stiffness material and structural concepts for morphing applications,” *Progress in Aerospace Sciences*, vol. 63, pp. 33–55, Nov 2013. DOI: 10.1016/j.paerosci.2013.07.001.

[39] S. Becker, T. Ranzani, R. S., and R. J. Wood, “Pop-up tissue retraction mechanism for endoscopic surgery,” in *IEEE/RSJ International Conference on Intelligent Robots and Systems*, IEEE, Sep 2017, pp. 920–927. DOI: 10.1109/IROS.2017.8202255.

[40] A. S. Chen, H. Zhu, Y. Li, L. Hu, and S. Bergbreiter, “A paper-based electrostatic zipper actuator for printable robots,” in *International Conference on Robotics and Automation (ICRA)*, IEEE, May 2014, pp. 5038–5043. DOI: 10.1109/ICRA.2014.6907597.

[41] K. Al-Souqi, K. Kadri, and S. Emam, “A review on vibration control using piezoelectric shunt circuits,” *Applied Sciences*, vol. 15, no. 11-6035, p. 30, 2025. DOI: 10.3390/app15116035.

[42] A. S. Roulaux, “Attitude control mechanisms of flapping-wing air vehicles,” MSc thesis, Delft University of Technology, May 2021.

[43] J. B. Kottiswaran, “Observations of the quasi-steady aerodynamic model of the atalanta,” MSc thesis, Delft University of Technology, Jul 2023.

[44] E. B. Magrab, *Vibrations of Elastic Systems* (Solid Mechanics and Its Applications), 2nd ed. Cham, Switzerland: Springer Nature Switzerland AG, 2024.

[45] F. S. Tse, I. E. Morse, and R. T. Hinkle, *Mechanical vibrations : theory and applications* (Allyn and Bacon series in mechanical engineering and applied mechanics), 2d. Boston: Allyn and Bacon, 1978.

[46] R. Haberman, *Mathematical models: mechanical vibrations, population dynamics, and traffic flow : an introduction to applied mathematics* (Classics in applied mathematics; 21). Philadelphia: Society for Industrial and Applied Mathematics, 1977.

[47] T. Moens, “Design and testing of a controllable hinge for a flapping-wing micro air vehicle,” MSc thesis, Delft University of Technology, Apr 2023.

[48] R. Diekerhof, “Resonating structures with flapping wings: Numerical modelling and validation,” MSc thesis, Delft University of Technology, Jun 2016.

[49] F. R. Serrano, E. Steinhardt, and R. J. Wood, “Considerations for the design and rapid manufacturing of pop-up mems devices,” *Advanced Materials Technologies*, vol. 9, Apr 2024. DOI: 10.1002/admt.202301940.

[50] L. L. Howell, S. P. Magleby, and B. M. Olsen, *Handbook of Compliant Mechanisms*, First. West Sussex: John Wiley & Sons, Ltd, 2013.

[51] W. C. Young and R. G. Budynas, *Roark’s Formulas for Stress and Strain*, 7th ed. New York, US: McGraw-Hill Companies, Inc, 2002.

[52] Henkel Adhesive Technologies Vietnam Co., Ltd.y. “LOCTITE® EA 9466.” (2025), [Online]. Available: https://www.henkel-adhesives.com/vn/en/product/structural-adhesives/loctite_ea_94661.html.

[53] Delft University of Technology. “Precision and Microsystems Engineering (PME) - About PME - Facilities.” (2025), [Online]. Available: https://www.tudelft.nl/me/over/afdelingen/precision-and-microsystems-engineering-pme/about-pme/facilities.

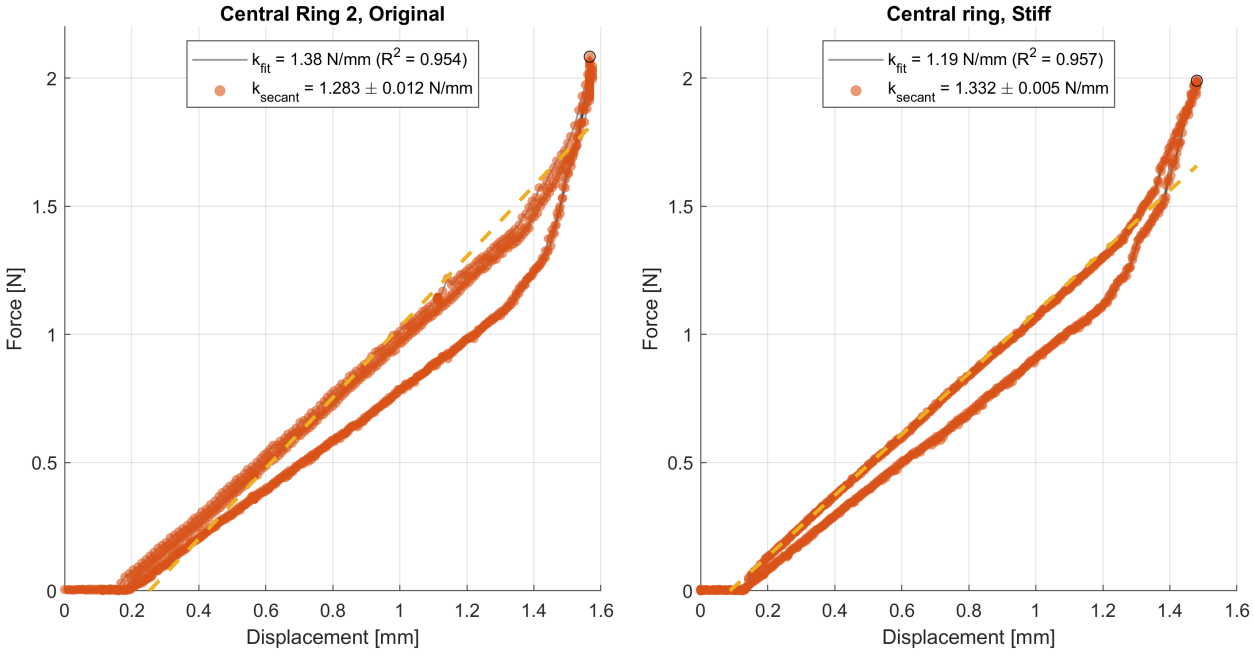
[54] The MathWorks, Inc., *Smoothing Splines — MATLAB & Simulink Documentation*, https://nl.mathworks.com/help/curvefit/smoothing-splines.html, Accessed: 2026-02-25, 2026.

[55] H. F. Brinson and L. C. Brinson, *Polymer Engineering Science and Viscoelasticity: An Introduction*, Second. New York: Springer, 2015. DOI: 10.1007/978-1-4899-7485-3.

[56] D. W. Childs and L. S. Andrés. “Dynamics and vibrations lecture notes (MEEN 363(501)) particle kinetics 2, lecture 14 to 18.” (2009), [Online]. Available: https://rotorlab.tamu.edu/Dynamics_and_Vibrations/Lectures%20(pdf)%20and%20homework/Particle%20Kinetics%202/L14-18.pdf.

[57] R. M. Schmidt, G. Schitter, and J. van Eijk, *The Design of High Performance Mechatronics*, 3rd ed. Amsterdam: IOS Press, 2011.

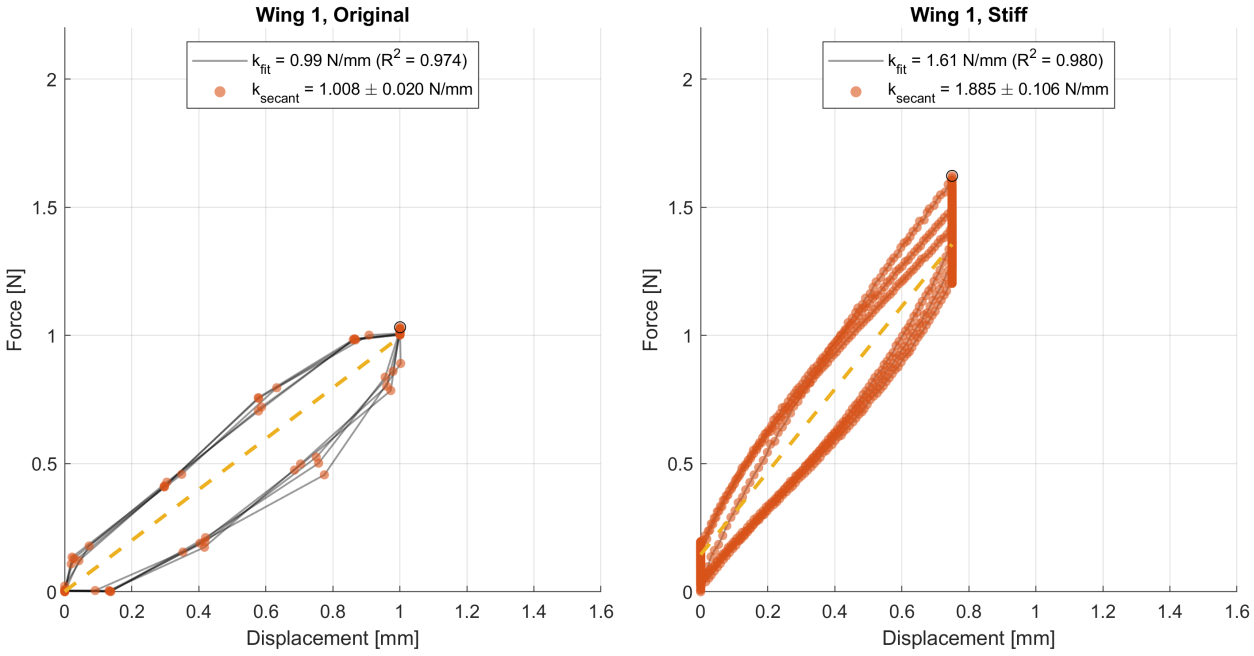
A Stiffness Measurements



(a) Central ring Original.

(b) Central ring Stiff V1.

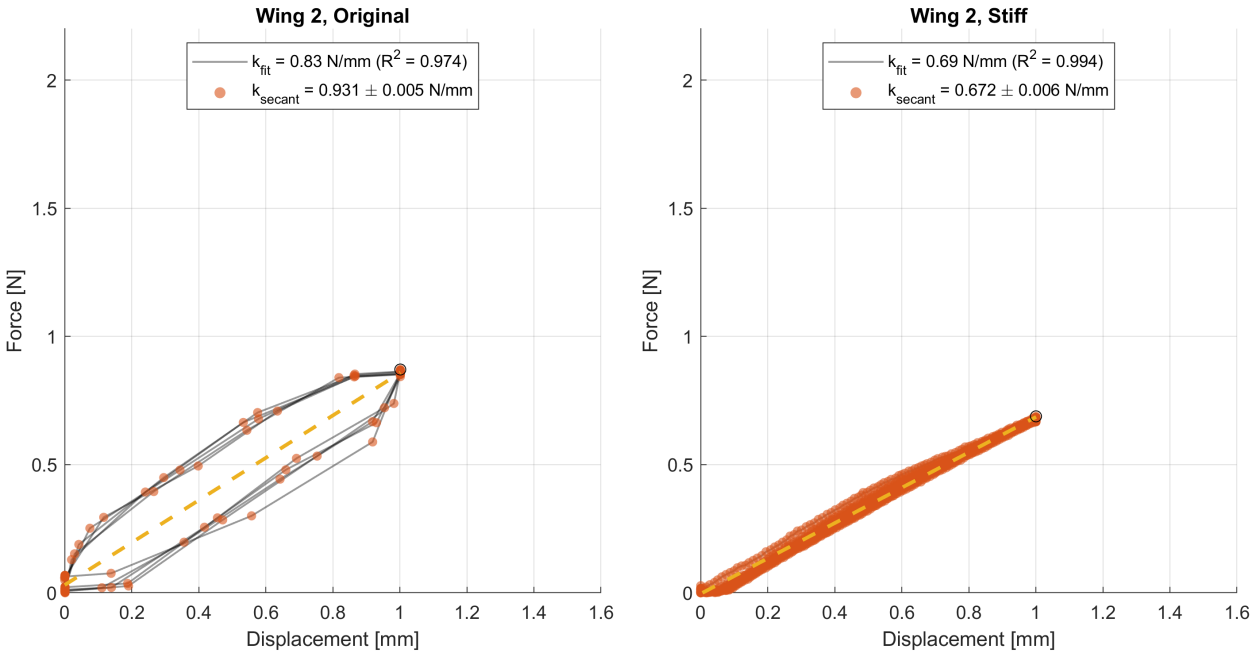
Figure A.1: Force-Displacement data for the central actuator in (a) the Original configuration, and (b) the Stiff V1 configuration.



(a) $w_1 w_4$ Original.

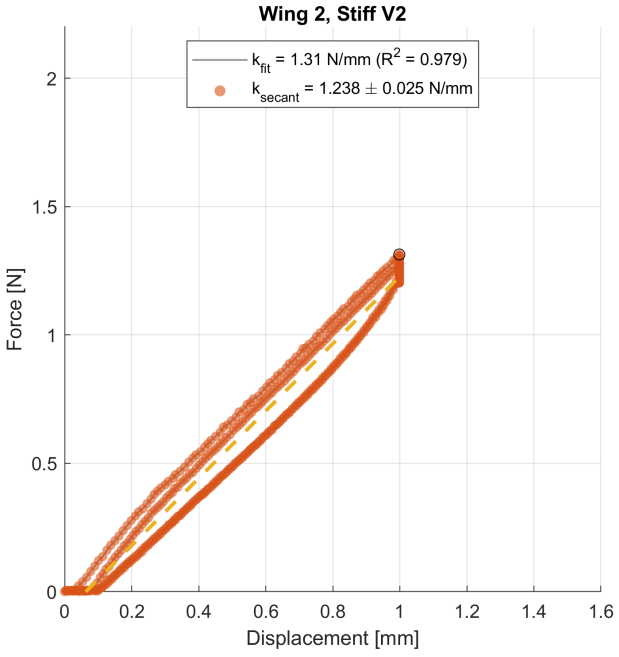
(b) $w_1 w_4$ Stiff V1.

Figure A.2: Force-Displacement data for the $w_1 w_4$ measurement in (a) the Original configuration, and (b) the Stiff V1 configuration.



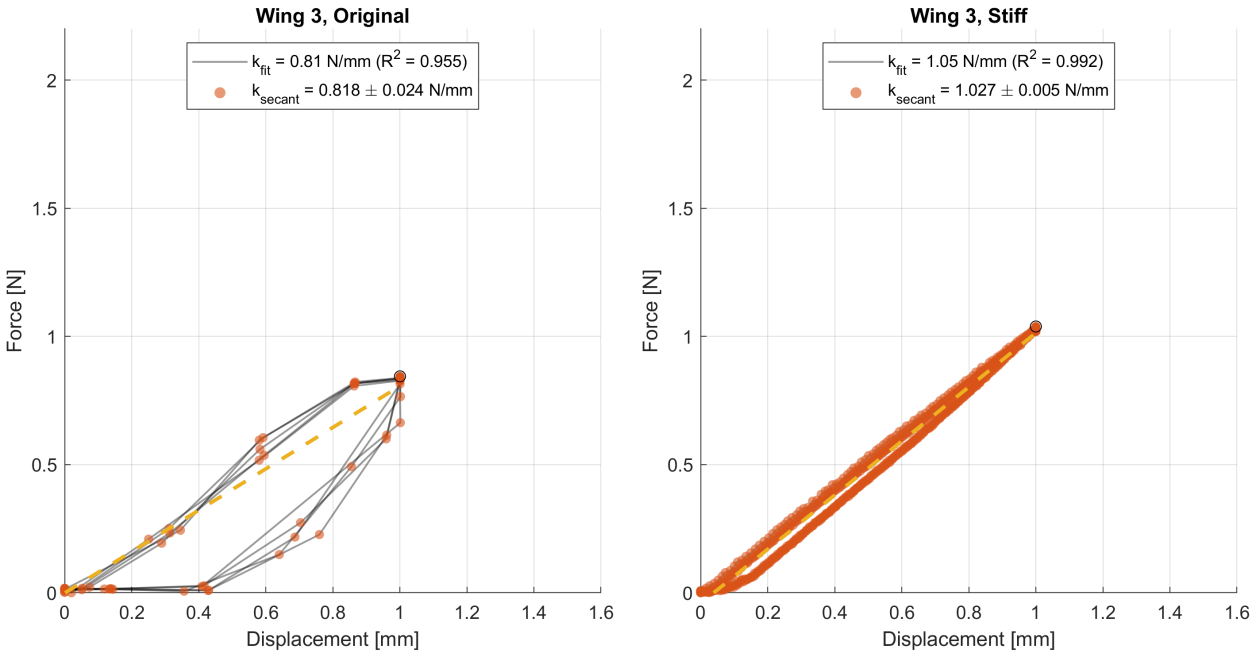
(a) w_2w_3 Original. **(b)** w_2w_3 Stiff V1.

Figure A.3: Force-Displacement data for the w_2w_3 measurement in (a) the Original configuration, and (b) the Stiff V1 configuration.



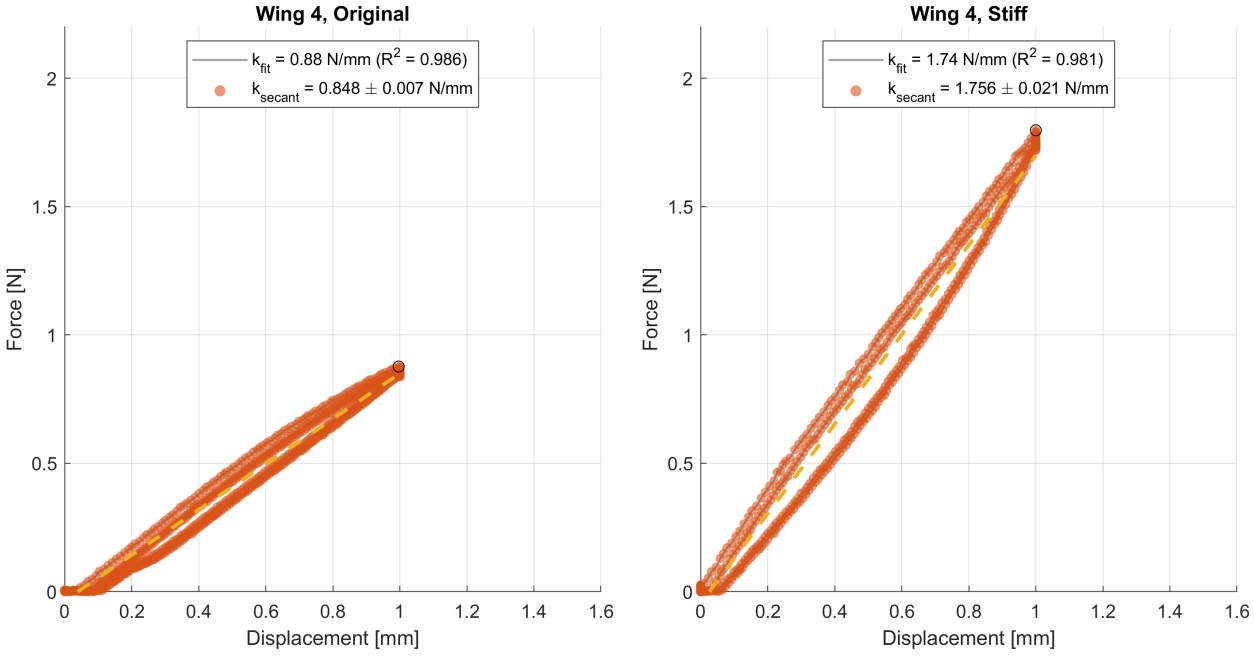
(a) w_2w_3 Stiff V2

Figure A.4: Force-Displacement data for the w_2w_3 measurement in (a) the Stiff V2 configuration.



(a) w_3w_2 Original **(b)** w_3w_2 Stiff V1

Figure A.5: Force-Displacement data for the w_3w_2 measurement in (a) the Original configuration, and (b) the Stiff V1 configuration.



(a) w_4w_1 Original **(b)** w_4w_1 Stiff V1

Figure A.6: Force-Displacement data for the w_4w_1 measurement in (a) the Original configuration, and (b) the Stiff V1 configuration.